



# Discrete Element Simulations and Experiments: Toward Applications for Cohesive Powders

Olukayode Isaiah Imole

**DISCRETE ELEMENT SIMULATIONS AND  
EXPERIMENTS:  
TOWARD APPLICATIONS FOR COHESIVE  
POWDERS**

Cover image

Superposition of the experimental samples used in this research

Cocoa powder (brown) and Limestone powder (white).

With special thanks to Nicola Saponieri and Vanessa Magnanimo

**DISCRETE ELEMENT SIMULATIONS AND  
EXPERIMENTS:  
TOWARD APPLICATIONS FOR COHESIVE  
POWDERS**

PROEFSCHRIFT

ter verkrijging van  
de graad van doctor aan de Universiteit Twente,  
op gezag van de rector magnificus,  
prof.dr. H. Brinksma,  
volgens besluit van het College voor Promoties  
in het openbaar te verdedigen  
op vrijdag 14 maart 2014 om 14.45 uur

door

Olukayode Isaiah IMOLE  
geboren op 22 november 1982  
te Lagos, Nigeria

Dit proefschrift is goedgekeurd door de promotoren :

Prof. dr. rer.-nat. S. Luding

dr. V. Magnanimo

*Samenstelling promotiecommissie :*

Rector Magnificus

Prof. dr. rer.-nat. S. Luding

Dr. V. Magnanimo

Prof.dr.-ing. A. Kwade

Prof.dr.ir. R. Akkerman

Prof. dr. J. Ooi

Dr. M. Ramaioli

Dr. ir. N. P. Kruyt

voorzitter

Universiteit Twente, promotor

Universiteit Twente, ass.-promotor

Technische Universität Braunschweig, Duitsland

Universiteit Twente

University of Edinburgh, Verenigd Koninkrijk

EPFL / Nestle Research Center, Lausanne, Zwitserland

Universiteit Twente



This research has been supported by the European Union Marie Curie Initial Training Network PARDEM FP7 (ITN-238577), see <http://www.pardem.eu/> for more information.

Keywords: granular materials, anisotropy, discrete element method, experiments, cohesive powders

Published by Gildeprint Drukkerijen, Enschede, The Netherlands

ISBN: 978-90-3653-633-2

Copyright © 2014 by Olukayode Isaiah Imole

All rights reserved. No part of the material protected by this copyright notice may be reproduced or utilized in any form or by any means, electronic or mechanical, including photocopying, recording or by any information storage and retrieval system, without written permission of the author.

*to my father and the memory of my loving mother*



# Summary

## **DISCRETE ELEMENT SIMULATIONS AND EXPERIMENTS: TOWARD APPLICATIONS FOR COHESIVE POWDERS**

by O. I. Imole

Granular materials are omnipresent in nature and widely used in various industries ranging from food and pharmaceutical to agriculture and mining – among others. It has been estimated that about 10% of the world’s energy consumption is used in the processing, storage and transport of granular materials. Owing to complexities like dilatancy, shear band formation and anisotropy, their behavior is far from completely understood. To gain an understanding of the deformation behavior, various laboratory element tests can be performed. Element tests are (ideally homogeneous) macroscopic tests in which the experimentalist can control the stress and/or strain path. One element test that can be performed is the uniaxial compression test. While such macroscopic experiments are pivotal to the development of constitutive relations for flow and rheology, they provide little information on the microscopic origin of the bulk flow behavior of these complex packings. In this thesis, we couple experiments and particle simulations to bridge this gap and link the microscopic properties to the macroscopic response for frictionless, frictional and cohesive granular packings, with the final goal of industrial application. The procedure of studying frictionless, frictional and cohesive granular assemblies independent of each other allows to isolate the main features related to each effect and provides a gateway into the use of discrete element methods to model and predict more complex industrial applications.

For frictionless packings, we find that different deformation paths, namely isotropic/uniaxial over-compression or pure shear, slightly increase or reduce the jamming volume fraction below which the packing loses mechanical stability. This observation suggests a necessary generalization of the concept of the jamming volume fraction from a single value to a “wide range” of values as a consequence of the modifications induced in the microstructure, i.e. fabric, of the granular material in the deformation history. With this understanding, a constitutive model is calibrated using isotropic and deviatoric modes. We then predict both the



stress and fabric evolution in the uniaxial mode.

By focusing on frictional assemblies, we find that uniaxial deformation activates microscopic phenomena not only in the active Cartesian directions, but also at intermediate orientations, with the tilt angle being dependent on friction, and different for stress and fabric. While a rank-2 tensor (representing a second order harmonic approximation) is sufficient to describe the evolution of the normal force directions, a sixth order harmonic approximation is necessary to describe the probability distributions of contacts, tangential forces and the mobilized friction.

As a further step, cohesion is introduced. From multi-stress level uniaxial experiments, by comparing two experimental setups and different cohesive materials, we report that while stress relaxation occurs at constant volume, the relative relaxation intensity decreases with increasing stress level. For longer relaxation, effects of previously experienced relaxation becomes visible at higher stress levels. A simple microscopic model is proposed to describe stress relaxation in cohesive powders, which accounts for the extremely slow force change via a response timescale and a dimensionless relaxation parameter.

In the final part of the thesis, we compare results from experiments and discrete element simulations of a cohesive powder in a simplified canister geometry to reproduce dosing (or dispensing) of powders by a turning coil in industrial applications. Since information is not easily accessible from physical tests, by scaling up the experimental particle size and calibrating material parameters like cohesive strength and interparticle friction, we obtain quantitative agreement between the mass per dose in simulations and experiments for different dosage times. The number of doses, for a given total filling mass is inversely proportional to dosage time and coil rotation speed, as expected, but increases with increasing number of coils. Using homogenization tools, we obtain the exact local velocity and density fields in our device.

# Samenvatting

## **Discrete Element Simulaties en Experimenten: Naar toepassingen op cohesieve poeders**

door O. I. Imole

Granulaire materialen zijn wijdverbreid in de natuur en worden verwerkt in een reeks van industrieën, variërend van de voedsel- en farmaceutische tot de agriculturele en mijnbouw-industrie. Er wordt geschat dat ongeveer 10% van het wereldwijde energieverbruik besteed wordt aan het verwerken, opslaan en transporteren van granulaire materie. Door complicaties zoals dilatatie, spanningslocalisatie en anisotropie, is het gedrag van dit soort materialen echter nog verre van begrepen. Om een beter begrip te krijgen van het gedrag onder deformaties kunnen verschillende elementaire laboratoriumtesten worden uitgevoerd. Elementaire testen zijn (idealiter homogene) macroscopische testen waarin de onderzoeker het rek- en/of spanningstraject van het materiaal onder controle heeft. Alhoewel deze macroscopische testen centraal staan in de ontwikkeling van constitutieve relaties, leveren ze maar weinig inzicht in de microscopische processen die aan de basis liggen van het macroscopisch stromingsgedrag van deze complexe materialen. In dit proefschrift worden experimenten en deeltjessimulaties gebruikt om een brug te slaan tussen de microscopische eigenschappen en het macroscopische gedrag voor wrijvingsloze, wrijvingsvolle en cohesieve granulaire materialen, met industriële toepassing als uiteindelijk doel. Het individueel bestuderen van deze drie verschillende soorten granulaire materialen stelt ons in staat de belangrijkste gevolgen van elk effect te bepalen, en daarmee een route te vinden naar de toepassing van Discrete Element Methods (DEM) in het modeleren en voorspellen van complexe industriële toepassingen.

Voor wrijvingsloze granulaire materialen vinden we dat verschillende deformatiegeschiedenissen, namelijk isotrope/uniaxiale compressie of een pure afschuiving, tot een kleine verandering leiden van de blokkeringsvolumefractie waaronder het granulaire materiaal zijn stabiliteit verliest. Deze observatie suggereert de noodzaak van een veralgemenisering van het begrip blokkeringsvolumefractie, van een eenduidige waarde naar een interval van waardes

als gevolg van veranderingen in de microstructuur die zijn opgewekt door de vervormingsgeschiedenis van het granulaire materiaal. Deze kennis is geïmplementeerd in een constitutief model, dat gekalibreerd is tegen isotrope en deviatorische vervormingen. Met dit model zijn vervolgens de ontwikkelingen van de spanning en de microstructuur onder een uniaxiale vervorming voorspeld.

Bij de bestudering van granulaire materialen met interne frictie hebben we gevonden dat uniaxiale vervorming niet alleen leidt tot microscopische effecten langs de actieve Cartesische richtingen, maar ook langs andere richtingen, waarbij de richtingshoek afhangt van de wrijving en verschilt tussen de spanning en de microstructurele vervorming. Terwijl een tweede-orde tensor volstaat voor de beschrijving van de ontwikkeling van de richtingen van de normaalkrachten, blijkt een zesde-orde harmonische benadering nodig te zijn voor de beschrijvingen van de waarschijnlijkheidsverdelingen van contacten, de tangentiële krachten en de gemobiliseerd wrijving.

In een vervolgstap is cohesie geïntroduceerd. Op grond van meerdere uniaxiale experimenten rapporteren we, door het vergelijken van twee experimentele methods en verschillende cohesieve materialen, dat terwijl spanningsrelaxatie optreedt bij constante volumetrische belasting, de mate van relatieve relaxatie afneemt bij toenemende spanning. Voor langere relaxaties wordt de invloed van eerder ondergane relaxaties zichtbaar onder later ingestelde hogere spanningen. We stellen een eenvoudig microscopisch model voor dat de spanningsrelaxatie in cohesieve poeders beschrijft, en daarbij verklaringen biedt voor de extreem langsame krachtsveranderingen en de tijdschaal van de relaxatie, alsmede voor een dimensieloze relaxatieparameter.

In het laatste deel van dit proefschrift vergelijken we experimenten en DEM simulaties van cohesieve poeders in een vereenvoudigde trommelgeometrie voor de dosering (en afgifte) van poeders in industriële toepassingen. Omdat het experimentele proces niet makkelijk direct bestudeerd kan worden, hebben we de experimentele deeltjesgrootte en de belangrijkste deeltjeseigenschappen, zoals de cohesie en de wrijving tussen deeltjes, opgeschaald. Hiermee hebben we een kwantitatieve overeenkomst gevonden tussen de massa per dosering in de simulaties en experimenten, bij verschillende doseringstijden. Het aantal doseringen vertoont een omgekeerde evenredigheid met de rotatie tijd en -snelheid van de doseringsspoel, maar neemt toe met de lengte van de spoel. Door gebruik te maken van homogeniseringsinstrumenten verkrijgen we de lokale snelheids- en dichtheidsvelden in het doseringsmechanisme.

# Acknowledgements

I am grateful to the Almighty God for the grace and strength he has given me to get to this point in my studies. Indeed, the past three and half years in the Multi Scale Mechanics group, University of Twente has been a learning period for me. Right from the time I came for the interview, till this present time, I have enjoyed tremendous support, help and guidance from colleagues, family and friends. At this point, I would like to express my heartfelt thanks to everyone who helped in one way or the other during the course of completing this thesis.

I would like to thank my supervisor Prof. Stefan Luding for accepting me into his group. Being under your tutelage for these years has given me the opportunity to learn, work on various problems and travel to interesting places. The discussions, comments, advice and iterations on our papers have taught me a lot about scientific writing. You have made me and my family feel at home in The Netherlands and I am very grateful for this. I will also not forget your wife, Gerlinde – who never ceases to ask about our welfare. Thank you very much. I thank my co-advisor, Vanessa Magnanimo, your day-to-day advice, supervision and coaching has been really invaluable. I cannot thank you enough for your insights and suggestions in the completion of this work. You taught me how to interpret scientific data, present ideas in a clear manner and keep a broad view. Thanks a lot.

To Dr. Marco Ramaioli and Dr. Edgar Chavez, I appreciate you for welcoming me into the Nestle, Switzerland family during my secondments. Edgar, thanks for always making sure I had all I need for my experiments, for the discussions and for the assistance and support you showed during my visits. Marco, you have made me a better researcher and taught me the essentials of working within and outside the academic world. I appreciate your feedback, supervision, corrections, openness and demand for the best. I profited a lot from your insights and ingenuity and I will never forget all you taught me. To the PARDEM consortium – professors, advisors, colleagues and industrial partners – I say thank you for the time we shared together during the training in several countries. A special thanks to Maria Paulick, Prof. Arno Kwade, Dr. Harald Zetzener and Dr. Martin Morgeneyer for hosting me during my short secondments to the Technische Universität, Braunschweig.

To the MercuryDPM development team, Anthony, Thomas and Dinant, I say thanks for the time you spent to get the canister set-up working. To my former and present colleagues in MSM – Abhi, Kuni, Martin, Fatih, Nico, Sudheshna, Vitaliy, Wouter den Breeijen (for the extra disk space), Wouter den Otter, Kazem – thank you all for the part you played in the success of my thesis. To my office mates, Mateusz and Nishant, I say thanks for the time we shared together travelling, discussing and collaborating in and outside research. A special thanks to Sylvia – the mother of the MSM group. Thanks for the care and support you showed to me. To my friends in Enschede and beyond – Tjay, Sam Odu, Bolaji Adesokan and family, Austin Ezejiofor and family, Adura Sopeju, Femi Odegbile, Sole Tunde, Eytayo Oluwadare Akin Omoteji – thank you all. To my church friends and their family – Ballard, Terence, Olumide, thanks for your prayers.

Finally, I'd like to thank my family. To my siblings, Dare, Kemi and Special, this achievement would not have been possible without you. I say a special thanks to my Dad for the sacrifice to make me what I am today. My nephews, nieces, cousins, uncles, aunts and in-laws, thank you all. Most importantly, I appreciate the sacrifice and support of my lovely wife, Moyo and son Daniel. Moyo, thank you for your prayers, encouragement, listening and understanding throughout the course of this work. I couldn't have asked for a better partner. To Dan, thanks for repeatedly stomping on my laptop, pulling the plug and making a mess. You're the best!

To everyone who contributed to my life, whose name I unfortunately forgot to include above, you mean no less to me. I appreciate you all.

Olukayode Imole  
Enschede, March 2014

# Contents

<b>Summary</b>	<b>v</b>
<b>Samenvatting</b>	<b>vii</b>
<b>Acknowledgements</b>	<b>ix</b>
<b>1 Introduction</b>	<b>1</b>
1.1 Background: Granular materials . . . . .	1
1.2 Philosophy . . . . .	3
1.3 The Discrete Element Method . . . . .	8
<b>2 Isotropic and shear deformation of frictionless granular assemblies</b>	<b>11</b>
2.1 Introduction . . . . .	12
2.2 Simulation method . . . . .	14
2.3 Preparation and test procedure . . . . .	16
2.4 Averaged quantities . . . . .	20
2.5 Evolution of micro-quantities . . . . .	26
2.6 Evolution of macro-quantities . . . . .	32
2.7 Theory: Macroscopic evolution equations . . . . .	39
2.8 Conclusions and Outlook . . . . .	44
<b>3 Effect of particle friction under uniaxial loading and unloading</b>	<b>49</b>
3.1 Introduction and Background . . . . .	50
3.2 Simulation details . . . . .	52
3.3 Definitions of Averaged Quantities . . . . .	57
3.4 Results and Observations . . . . .	62
3.5 Polar Representation . . . . .	79
3.6 Summary and Outlook . . . . .	84
<b>4 Slow relaxation behaviour of cohesive powders</b>	<b>91</b>
4.1 Introduction and Background . . . . .	92

---

4.2	Sample Description and Material Characterization . . . . .	93
4.3	Experimental Set-up . . . . .	95
4.4	Stress Relaxation Theory . . . . .	99
4.5	Results and Discussion . . . . .	100
4.6	Conclusion and Outlook . . . . .	106
<b>5</b>	<b>Dosing of cohesive powders in a simplified canister geometry</b>	<b>109</b>
5.1	Introduction and Background . . . . .	110
5.2	Dosage Experiments . . . . .	111
5.3	Numerical Simulation . . . . .	114
5.4	Experiments . . . . .	119
5.5	Numerical Results . . . . .	122
5.6	Conclusion . . . . .	130
<b>6</b>	<b>Conclusions and Recommendations</b>	<b>133</b>
	<b>References</b>	<b>139</b>
	<b>Curriculum vitae</b>	<b>149</b>

# Chapter 1

## Introduction

### 1.1 Background: Granular materials

From sandcastles to large rocks, from cereals to food powder, table salt to wheat grains, coffee beans to baking flour, granular materials, next to water and air, are indispensable to our existence on earth. Even in space exploration, the importance of granular materials to the success of space mission has been reported.

The storage, handling, processing and packaging of granular materials also cuts across different industrial sectors. In the chemical, biotechnological, pharmaceutical, textile, environmental protection, food industries, operations such as mixing, segregation, precipitation, crystallization, fluidization, agglomeration, are common and often involves the processing of granular materials. In highly developed economies, number of particulate raw or finished products can amount to millions and is permanently increasing day by day because of diversified requirements of various clients and consumers in the global market. In fact, it has been estimated that about 10% of the world's energy consumption is used in the processing, storage and transport of granular materials. Despite its importance, a question that arises is why the behavior of granular materials is far from being completely understood.

To answer this question, one would need to draw an analogy between granular materials and water. It is known that largest portion of the earth's surface is covered by water in form of oceans, seas and lakes. Depending on the prevailing temperature and pressure, water may take on different forms of matter. For example, at room temperature and pressure, water is liquid. However, when the room temperature is increased, it changes state and water vapor





Figure 1.1: Granular materials can take on the different states of matter in a sand hour glass [1].

(or gas) emerges. Additionally, when water is frozen, it becomes (solid) ice with different properties than when it is in the liquid or solid state at different temperature. Due to this multi-variate nature, it is impossible to fully classify water as a perfect solid, liquid or gas.

Granular materials can also easily pass through the three phases of matter in a single geometry. For example, in the flowing sand hour glass illustrated in Fig. 1.1, the top section consists of grains completely static, fixed in position as one would expect in a solid. Closer to the channel at the bottom of the top section, one observes that the grains are flowing as one would expect in a liquid. In the bottom compartment, as the flowing grains settle, they form a heap at the center of the glass indicating that they can support their own weight, which a normal liquid cannot do. Looking closely at the top of the heap, one observes collisions of grains with the heap along with random motion of grains, similar to what one would see in a gas.

Yet, one observes that in contrast to what is seen in gases, the collisions between the grains in the sand hour glass are dissipative in nature. This means that the collisions are inelastic leading to energy loss due to friction between the grains. Hence granular materials are seen as an assembly of particles or grains that are not in thermal equilibrium and the classical laws governing the flow of fluids and gases do not hold. All these make the study of granular materials an enigma – a challenging and interesting multi-disciplinary endeavor for scientists, physicists, engineers, mathematicians and theoreticians.

## 1.2 Philosophy

Many industrial particle systems display unpredictable behaviour and thus are difficult to handle. This gives rise to considerable challenges for fundamental understanding and the design and operation of unit-processes and plants. In an industrial survey, Ennis et al. [39] reported that 40% of the capacity of industrial plants is wasted because of granular solid problems. Merrow [109] also reported that the main factor causing long start-up delays in chemical plants is solids processing, especially the lack of reliable predictive models and simulations. This displays the urgent industrial need for a computational technique based on a physical understanding of particle systems that can adequately model the mechanical response of granular materials in order to be able to devise new technologies, to improve existing designs and to optimize operating conditions.

In order to understand the behavior of granular materials, element tests can be performed. Element tests are ideally homogeneous laboratory experiments that allow the user to control the stress/strain path. Such macroscopic experiments are useful in developing and calibrating constitutive relations, but provide little information on the microscopic origin of the bulk flow behavior. An alternative approach is to perform discrete element simulations (DEM) [11, 34, 89, 92, 151].

Despite the huge popularity of the discrete element method and the increased number of publications over the past few years, one main there is still a lot of skepticism in the industry about the power of this method in predicting industrial problems. One main obstacle for the general acceptance of DEM in industry is the lack of verification and validation methodologies and accepted model calibration methods within the framework illustrated in Fig. 1.2 – especially when cohesive fine powders of non-spherical shape are involved.<sup>1</sup>

Verification in this sense refers to methods aimed at determining that the DEM model implementation accurately reproduces the underlying conceptual model and its solutions [118]. In verification, the discrete element code and calculation algorithms are checked against highly accurate analytical or numerical benchmark solutions. In this sense, verification is about the mathematics and the programming and not about the physics and mechanics involved. Potential sources of numerical errors in a typical DEM computation include inappropriate particle scale representation, insufficiently small computational time steps and computing round-off and programming errors.

The verification process is followed by an altogether much more challenging task of validation which assesses the degree to which the computational model accurately represents the physics being modelled. Validation of DEM simulation thus requires a comparison between

---

<sup>1</sup>The verification and validation framework presented in this section is largely based on J. Y. Ooi. Establishing predictive capabilities of DEM - Verification and validation for complex granular processes. *AIP Conf. Proc.*, 1542:20–24, 2013

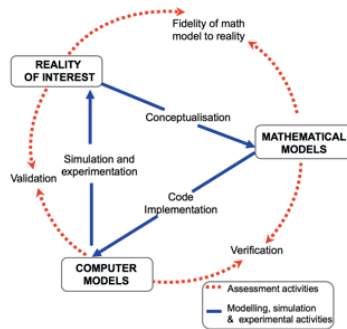


Figure 1.2: Verification and validation framework according to Ooi [118].

the simulation and the validation experiment, where the predictive capability is evaluated against the physical reality whilst addressing the uncertainties arising from both experiments and computations [118].

As many granular processes are inherently very complex, it is necessary to approach the problem in a hierarchical fashion by first identifying and validating against simpler “components” of the system before the complete process with the full-fledged complexities is tackled. Validation experiments require a rigorous characterization of the test material, test conditions and uncertainties in the experimental measurements. Exemplary verification tests that can be performed include the elastic normal impact of two identical spheres, elastic normal impact of a sphere with a rigid plane and the oblique impact of a sphere with a rigid plane at constant resultant velocity and varying incident angles [118].

Additionally, a micromechanical description, which takes into account the discrete nature of granular systems, is necessary and must be linked to the continuum description, which involves the formulation of constitutive relations for macroscopic fields [48, 49, 72, 79, 107, 152]. The parameters of these constitutive models have to be identified from experimental or numerical calibration tests [41] while the predictive quality must then be tested against an independent test.

In the following, we will address some interesting properties of granular materials and how these influence their behavior under different conditions.

### 1.2.1 Particle Size and Shape

Granular materials come in different shapes and sizes and have different morphological properties. A few examples of industrial materials are shown in Fig. 1.3 all having different properties – from long (tremolite), round porous (grain oil char), spherical (coal fly

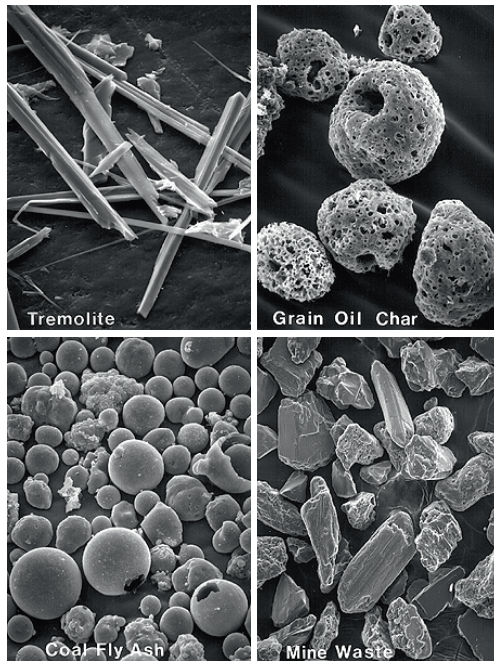


Figure 1.3: Granular materials can have different shapes from tremolite (elongated), grain oil char (round and porous), coal fly ash (spherical) to mine waste (angular) according to Ref. [2]

ash) and angular (mine waste). The particle shape and size distribution, amongst other parameters determine mechanical material properties such as friction, or compressive strength [121, 144, 182] of granular materials. The description of shape can take place by words or pictures (qualitative), by numbers (quantitative) or, to compare results from different analysis procedures, by shape factors. The British norm (BS 2955) proposes some adjectives to describe particle shapes. In a rougher form, elongation tells how close the particle shape is to a sphere, but gives no information about the roughness of the surface. Circularity is defined as the ratio of circuit of sphere with an area equal to particle to particle circuit. It is related to the overall particle shape and its roughness. Convexity informs just about the roughness of the surface with no other information [3].

For the description of a particle, geometrical length scales, the statistical length, as well as physical equivalent diameters and also the specific surface are used. For example, commonly used as geometrical length scale is the diameter or length of a cylindrical granular or an almost spherical particle. Also the volume  $V$  of a particle and the surface  $S$  are often used as direct size measurement. For a non spherical particle those properties can be transferred via the equivalent diameter. The most important geometrical equivalent diameters are [3]:

1.  $d_V$ : diameter of a sphere with an equal volume,
2.  $d_S$ : diameter of a sphere with an equal surface,
3.  $d_P$ : diameter of a circle with the same projected surface and
4.  $d_{lc}$ : light scattering diameter.

## 1.2.2 Friction

Friction is the force preventing the relative motion of solid surfaces, fluid layers or material elements sliding against each other. The classical laws of solid friction was first written by Amontons in 1699 and further developed by Coulomb in 1785 [13] and describes the minimum lateral/tangential  $F_f$  force required to put two bodies in motion. The tangential force is defined as:

$$F_f = \mu N, \tag{1.1}$$

where the dimensionless scaler  $\mu$  is the static friction coefficient and  $N$  is the normal force pressing the two bodies together. The Amontons-Coulomb friction law are widely used in several applications; for example in silo design where friction at the silo walls provides a vertical load carrying capacity, thereby, reducing the horizontal stress at the bottom of the silo [8]. Static and dynamic as well as sliding and rolling friction can be distinguished [3].

Static frictional forces from the interlocking of the irregularities of two surfaces will increase to prevent any relative motion up until some limit where motion occurs. Dynamic friction occurs when two objects are moving relative to each other and is usually lower than the coefficient of static friction for the same material [108]. Dynamic friction is almost constant over a wide range of low speeds.

Rolling friction is the torque that resists the rolling of a circular object along a surface. The rolling friction can arise from several sources at the contact between two particles or between a particle and surface. These may include micro-slip and friction on the contact surface, plastic deformation around the contact, viscous hysteresis, surface adhesion and shape effects [9, 67].

When both materials are hard, a combination of static/dynamic friction (caused by irregularities of both surfaces) and molecular friction (caused by the molecular attraction or adhesion of the materials) slow down the rolling. When the particle is soft, its deformation slows down the motion. When the other surface is soft, the plowing effect is a major force in slowing the

motion. Sliding resistance is the force that resists motion of a body over a surface with no rolling.

The microscopic origin of friction is non-trivial. The first microscopic interpretation of friction, taking into account the asperities/roughness between surfaces in contact was proposed by Bowden and Tabor [13, 27]. The theory assumes that the contact area between bodies in contact are much smaller than the apparent contact area such that only the highest asperities sustain the normal stress. Furthermore, the highest asperities deform plastically due to the large contact stress, thus making the normal stress at contact a constant. Bowden and Tabor further assume that the asperities in contact ‘weld’ together to form a ‘solid’ joint which must be broken by a critical shear stress for sliding to occur.

Limitations of the Amontons–Coulomb laws occurs for high normal loads or very soft materials where the surface roughness is flattened leading to a saturation of the frictional force with normal force. A second limitation is the assumption of constant friction coefficients – which is not valid for phenomena such as ageing (increasing  $\mu$  with time) and velocity weakening (decreasing dynamic friction with time) [13].

### 1.2.3 Cohesion

The cohesion,  $c$ , is the resistance of a physical body, subjected to its separation into parts. The cohesion of particulate solids can be classified in two very broad types: wet and dry cohesion. In wet (moisture-induced) cohesion capillary forces dominate particles interactions. In dry cohesion, for solids of less than 10  $\mu\text{m}$ , van der Waals forces and electrostatic forces are also significant [3].

Cohesive powders have the ability to gain strength when stored at rest under compressive stress for a long period of time. Wahl et al. [165] reported that moisture, temperature, pressure, particle size and storage time have a major effect on the particles during storage hence research on the study of caking must be based on the application of real storage conditions. Schulze [138] suggests that cohesion can be due to deformation and increase of the particle contact area leading to higher adhesive forces, interlocking by particle shape effects (overlap due to surface asperities and hook-like bonds). Another reason can be bridge formation due to solid crystallization during drying or due to the dissolution of some materials from moisture absorption [3].

## 1.3 The Discrete Element Method

The Discrete Element Method (DEM) [11, 34, 89, 92, 151] helps to better understand and model the deformation behaviour of particle systems. Since the elementary units of granular materials are mesoscopic grains which deform under stress and the realistic modelling of the particles is much complicated, the DEM relates the interaction force to the overlap of two particles. If all forces  $\mathbf{f}_i$  acting on the particle  $i$  either from other particles, from boundaries or from external forces, are known, the problem is reduced to the integration of Newton's equations of motion for the translational and rotational degrees of freedom:

$$\frac{d}{dt}(m_i \dot{\mathbf{r}}_i) = \mathbf{f}_i + m_i \mathbf{g} \quad (1.2)$$

with the mass  $m_i$  of particle  $i$ , its position  $\mathbf{r}_i$ , the velocity  $\dot{\mathbf{r}}_i$  of the center of mass, the resultant force  $\mathbf{f}_i = \sum_c \mathbf{f}_i^c$  acting on it due to contacts with other particles or with the walls, the acceleration due to volume forces like gravity  $\mathbf{g}$ .

Two spherical particles  $i$  and  $j$ , with radii  $a_i$  and  $a_j$ , respectively, interact only if they are in contact so that their overlap  $\delta = (a_i + a_j) - (\mathbf{r}_i - \mathbf{r}_j) \cdot \mathbf{n}$  is positive, i.e.  $\delta > 0$ , with the unit normal vector  $\mathbf{n} = \mathbf{n}_{ij} = (\mathbf{r}_i - \mathbf{r}_j) / |\mathbf{r}_i - \mathbf{r}_j|$  pointing from  $j$  to  $i$ . The force on particle  $i$ , from particle  $j$ , at contact  $c$ , has normal and tangential components. The normal force is complemented by a tangential force law [92], such that the total force at contact  $c$  is:  $\mathbf{f}_c = f_n \hat{\mathbf{n}} + f_t \hat{\mathbf{t}}$ , where  $\hat{\mathbf{n}} \cdot \hat{\mathbf{t}} = 0$ , with tangential force unit vector  $\hat{\mathbf{t}}$ . For more details on the contact force laws, see chapter 5.

### 1.3.1 Thesis Outline

This thesis focuses on the deformation behavior of granular materials under different strain, stress and dynamic conditions. As a tool, laboratory experiments and discrete element simulations are used to understand the microscopic and macroscopic response of these granular assemblies which have been idealized as packings of polydisperse spherical disks. In general, the philosophy of this thesis is split into three distinct, however interrelated parts namely:

1. The effects of the deformation paths on the microscopic and macroscopic response of *frictionless* and *frictional* granular assemblies as presented in chapters 2 and 3, respectively. This is accomplished *purely* using *quasi-static* DEM simulation of element tests in a triaxial box geometry under *high confining stress* conditions.

2. An *experimental* study of the time-dependent behavior of cohesive granular materials under oedometric (uniaxial) compression is presented in chapter 4 showing where the contact models used in the simulation have to be improved.
3. A *combination* of experiments and discrete element simulations in the investigation of an *application*, namely the dosing of cohesive powders in a simplified canister geometry, as presented in chapter 5. This study is conducted under low consolidation stress and both static and dynamic conditions alternating.

In chapter 2, we investigate the response of granular assemblies to isotropic, uniaxial and shear deformation. On the microscopic side we report on the response of the coordination number and fraction of rattlers and their dependence on their respective jamming volume fractions. On the macroscopic scale, we report on the evolution isotropic pressure and isotropic fabric along with the deviatoric stress and fabric with volume fraction. In the final part of the chapter, we test the predictive power of a simple anisotropy model – calibrated with the deviatoric shear simulation – on the uniaxial mode.

In chapter 3, the effect of friction on packings of polydisperse granular assemblies subjected to uniaxial loading and unloading is studied. We use the magnitude and orientation of contacts to understand the dependence of the deviatoric stress ratio and deviatoric fabric on friction. Microscopic observations on the number of sliding/sticking contacts and the directional probability distribution of normal forces are also studied. Finally, evolution of the normal force directions, contact probability distributions, tangential force and mobilized friction are approximated using harmonic functions.

Chapter 4 focuses on experiments on the time-dependent relaxation behavior of two cohesive powders under uniaxial deformation as compared between two testers. We show that strain rate, relaxation time, and a step-wise loading and relaxation cycle all influence the creep-like behavior. The parameters of a simple microscopic model that captures the creep behavior is also presented. We highlight where the contact models used in discrete element simulations need to be improved.

Finally in 5, we present experimental and numerical findings on the dosing of cohesive powders in a simplified canister geometry. We show that our discrete element simulations are capable of quantitatively reproducing observations from experiments in terms of the dosed mass throughput, the number of coils and the initial mass in the canister. Finally, using homogenization (coarse-graining) tools, we extract other macroscopic fields and show further insights on the dosing action.





## Chapter 2

# Isotropic and shear deformation of frictionless granular assemblies\*

### Abstract

*Stress- and structure-anisotropy (bulk) responses to various deformation modes are studied for dense packings of linearly elastic, frictionless, polydisperse spheres in the (periodic) tri-axial box element test configuration. The major goal is to formulate a guideline for the procedure of how to calibrate a theoretical model with discrete particle simulations of selected element tests and then to predict another element test with this calibrated model (parameters).*

*Only the simplest possible particulate model-material is chosen as the basic reference example for all future studies that aim at the quantitative modeling of more realistic frictional, cohesive powders. Seemingly unrealistic materials are used to exclude effects that are due to contact non-linearity, friction, and/or non-sphericity. This allows to unravel the peculiar interplay of micro-structural organization, i.e. fabric, with stress and strain.*

*Different elementary modes of deformation are isotropic, deviatoric (volume-conserving), and their superposition, e.g., a uni-axial compression test. (Other ring-shear or*

---

\*Based on O. I. Imole, N. Kumar, V. Magnanimo, and S. Luding. Hydrostatic and Shear Behavior of Frictionless Granular Assemblies Under Different Deformation Conditions. *KONA Powder and Particle Journal*, 30:84–108, 2013

*stress-controlled (e.g. isobaric) element tests are referred to, but not studied here.) The deformation modes used in this study are especially suited for the bi- and tri-axial box element test set-up and provide the foundations for powder flow in many other experimental devices. The qualitative phenomenology presented here is expected to be valid, even more clear and magnified, in the presence of non-linear contacts, friction, non-spherical particles and, possibly, even for strong attractive/adhesive forces.*

*The scalar (volumetric, isotropic) bulk properties, like the coordination number and the hydrostatic pressure, scale qualitatively differently with isotropic strain, but behave in a very similar fashion irrespective of the deformation path applied. The deviatoric stress response, i.e., stress-anisotropy, besides its proportionality to deviatoric strain, is cross-coupled to the isotropic mode of deformation via the structural anisotropy; likewise, the evolution of pressure is coupled via the structural anisotropy to the deviatoric strain. Note that isotropic/uniaxial over-compression or pure shear slightly increase or reduce the jamming volume fraction, respectively. This observation allows to generalize the concept of “the” jamming volume fraction, below which the packing loses mechanical stability, from a single value to a “wide range”, as a consequence of the deformation-history of the granular material that is “stored/memorized” in the structural anisotropy.*

*The constitutive model with incremental evolution equations for stress and structural anisotropy takes this into account. Its material parameters are extracted from discrete element method (DEM) simulations of isotropic and deviatoric (pure shear) modes as volume fraction dependent parameters. Based on this calibration, the theory is able to predict qualitatively (and to some extent also quantitatively) both the stress and fabric evolution in the uniaxial, mixed mode during compression.*

## 2.1 Introduction

Dense granular materials are generally complex systems which show unique mechanical properties different from classical fluids or solids. Interesting phenomena like dilatancy, shear-band formation, history-dependence, jamming and yield stress - among others - have attracted significant scientific interest over the past decade. The bulk behavior of these materials depends on the behavior of their constituents (particles) interacting through contact forces. To get an understanding of the deformation behavior of these materials, various laboratory element tests can be performed [111, 133, 140]. Element tests are (ideally homogeneous) macroscopic tests in which the experimentalist can control the stress and/or strain path. Different element test experiments on packings of bulk solids have been realized in the bi-axial box (see [113] and references therein) while other deformations modes, namely uniaxial and volume conserving shear have been reported in [122, 131]. While such macro-

scopic experiments are important ingredients in developing constitutive relations, they provide little information on the microscopic origin of the bulk flow behavior of these complex packings.

The complexity of the packings becomes evident when they are compressed isotropically. In this case, the only macroscopic control parameters are volume fraction and pressure [51, 98]. At the microscopic level for isotropic samples, the micro-structure (contact network) is classified by the coordination number (i.e. the average number of contacts per particle) and the fraction of rattlers (i.e. fraction of particles that do not contribute to the mechanical stability of the packing) [51]. However, when the same material sample is subjected to shear deformation, not only does shear stress build up, but also the anisotropy of the contact network develops, as it relates to the creation and destruction of contacts and force chains [11, 124, 166]. In this sense, anisotropy represents a history-parameter for the granular assembly. For anisotropic samples, scalar quantities are not sufficient to fully represent the internal contact structure, but an extra tensorial quantity has to be introduced, namely the fabric tensor [47]. To gain more insight into the micro-structure of granular materials, numerical studies and simulations on various deformation experiments can be performed, see Refs. [157, 159, 160] and references therein.

In an attempt to classify different deformation modes, Luding et al. [98] listed four different deformation modes: (0) isotropic (direction-independent), (1) uniaxial, (2) deviatoric (volume conserving) and (3) bi-/tri-axial deformations. The former are purely strain-controlled, while the latter (3) is mixed strain-and-stress-controlled either with constant side stress [98] or constant pressure [101]. The isotropic and deviatoric modes 0 and 2 are pure modes, which both take especially simple forms. The uniaxial deformation test derives from the superposition of an isotropic and a deviatoric test, and represents the simplest element test experiment (oedometer, uniaxial test or lambda-meter) that activates both isotropic and shear deformation. The bi-axial tests are more complex to realize and involve mixed stress-and-strain-control instead of completely prescribed strains as often applied in experiments [113, 178], since they are assumed to better represent deformation under realistic boundary conditions – namely the material can expand and form shear bands.

In this study, various deformation paths for assemblies of polydisperse packings of linearly elastic, non-frictional cohesionless particles are modeled using the DEM simulation approach. One goal is to study the evolution of pressure (isotropic stress) and deviatoric stress as functions of isotropic and deviatoric strain. Microscopic quantities like the coordination number, the fraction of rattlers, and the fabric tensor are reported for improved microscopic understanding. Furthermore, the extensive set of DEM simulations is used to calibrate the anisotropic constitutive model, as proposed in Refs. [98, 101]. After calibration through isotropic [51] and volume conserving pure shear simulations, the derived relations between the parameters and volume fraction are used to predict uniaxial deformations. Another goal is to improve the understanding of the macroscopic behavior of bulk particle systems and to

guide further developments of new theoretical models that describe it.

The focus on the seemingly unrealistic materials allows to exclude effects that are due to friction, other contact non-linearities and/or non-sphericity, with the goal to unravel the interplay of micro-structural organization, fabric, stress and strain. This is the basis for the present research – beyond the scope of this paper – that aims at the quantitative modeling of these phenomena and effects for realistic frictional, cohesive powders. The deformation modes used in this study are especially suited for the bi-axial box experimental element test set-up and provide the fundamental basis for the prediction of many other experimental devices. The qualitative phenomenology presented here is expected to be valid, even more clear and magnified, in the presence of friction and non-spherical particles, and possibly even for strong attractive forces.

This chapter is organized as follows: The simulation method and parameters used are presented in section 2.2, while the preparation and test procedures are introduced in section 2.3. Generalized averaging definitions for scalar and tensorial quantities are given in section 2.4 and the evolution of microscopic quantities is discussed in section 2.5. In section 2.6, the macroscopic quantities (isotropic and deviatoric) and their evolution are studied as functions of volume fraction and deviatoric (shear) strain for the different deformation modes. These results are used to obtain/calibrate the macroscopic model parameters. Section 2.7 is devoted to theory, where we relate the evolution of the micro-structural anisotropy to that of stress and strain, as proposed in Refs. [98, 101], to display the predictive quality of the calibrated model.

## **2.2 Simulation method**

The Discrete Element Method (DEM) [34], was used to perform simulations in bi- and tri-axial geometries [38, 75, 89, 151], involving advanced contact models for fine powders [92], or general deformation modes, see Refs. [11, 157, 160] and references therein.

However, since we restrict ourselves to the simplest deformation modes and the simplest contact model, and since DEM is otherwise a standard method, only the contact model parameters and a few relevant time-scales are briefly discussed – as well as the basic system parameters.

### **2.2.1 Force model**

For the sake of simplicity, the linear visco-elastic contact model for the normal component of force has been used in this work and friction is set to zero (and hence neither tangential

forces nor rotations are present). The simplest normal contact force model, which takes into account excluded volume and dissipation, involves a linear repulsive and a linear dissipative force, given as

$$\mathbf{f}^n = f^n \hat{\mathbf{n}} = (k\delta + \gamma\dot{\delta}) \hat{\mathbf{n}}, \quad (2.1)$$

where  $k$  is the spring stiffness,  $\gamma$  is the contact viscosity parameter and  $\delta$  or  $\dot{\delta}$  are the overlap or the relative velocity in the normal direction  $\hat{\mathbf{n}}$ . An artificial viscous background dissipation force  $\mathbf{f}_b = -\gamma_b \mathbf{v}_i$  proportional to the moving velocity  $\mathbf{v}_i$  of particle  $i$  is added, resembling the damping due to a background medium, as e.g. a fluid. The background dissipation only leads to shortened relaxation times, reduced dynamical effects and consequently lower computational costs without a significant effect on the underlying physics of the process – as long as quasi-static situations are considered.

The results presented in this study can be seen as “lower-bound” reference case for more realistic material models, see e.g. Ref. [92] and references therein. The interesting, complex behavior and non-linearities *can not be* due to the contact model but due to the collective bulk behavior of many particles, as will be shown below.

## 2.2.2 Simulation Parameters and time-scales

Typical simulation parameters for the  $N = 9261 (= 21^3)$  particles with average radius  $\langle r \rangle = 1[\text{mm}]$  are density  $\rho = 2000 [\text{kg/m}^3]$ , elastic stiffness  $k = 10^8 [\text{kg/s}^2]$  particle damping coefficient  $\gamma = 1 [\text{kg/s}]$ , and background dissipation  $\gamma_b = 0.1 [\text{kg/s}]$ . The polydispersity of the system is quantified by the width ( $w = r_{\text{max}}/r_{\text{min}} = 3$ ) of a uniform distribution with a step function as defined in [51], where  $r_{\text{max}} = 1.5[\text{mm}]$  and  $r_{\text{min}} = 0.5[\text{mm}]$  are the radius of the biggest and smallest particles respectively.

A typical response time is the collision time duration  $t_c$ . For a pair of particles with masses  $m_i$  and  $m_j$ ,  $t_c = \pi / \sqrt{k/m_{ij} - (\gamma/2m_{ij})^2}$ , where  $m_{ij} = m_i m_j / (m_i + m_j)$  is the reduced mass. The coefficient of restitution for the same pair of particle is expressed as  $e = \exp(-\gamma t_c / 2m_{ij})$  and quantifies dissipation. The contact duration  $t_c$  and restitution coefficient  $e$  are dependent on the particle sizes and since our distribution is polydisperse, the fastest response time scale corresponding to the interaction between the smallest particle pair in the overall ensemble is  $t_c = 0.228[\mu\text{s}]$  and  $e$  is 0.804. For two average particles,  $t_c = 0.643[\mu\text{s}]$  and  $e = 0.926$ . Thus, the dissipation time-scale for contacts between two average sized particles,  $t_e = 2m_{ij}/\gamma = 8.37[\mu\text{s}]$  is considerably larger than  $t_c$  and the background damping time-scale  $t_b = \langle m \rangle / \gamma_b = 83.7[\mu\text{s}]$  is much larger again, so that the particle- and contact-related time-scales are well separated. The strain-rate related timescale is  $t_s = 1/\dot{\epsilon}_{zz} = 0.1898[\text{s}]$ . As usual in DEM, the integration time-step was chosen to be about 50 times smaller than the shortest time-scale  $t_c$  [92].

Note that the units are artificial; Ref. [92] provides an explanation of how they can be consistently rescaled to match quantitatively the values obtained from experiments (due to the simplicity of the contact model used).

Our numerical ‘experiments’ are performed in a three-dimensional tri-axial box with periodic boundaries on all sides. One advantage of this configuration is the possibility of realizing different deformation modes with a single experimental set-up and a direct control of stress and/or strain [38, 98]. The systems are ideally homogeneous, which is assumed, but not tested in this study.

The periodic walls can be strain-controlled to move following a co-sinusoidal law such that, for example, the position of the top wall as function of time  $t$  is

$$z(t) = z_f + \frac{z_0 - z_f}{2}(1 + \cos 2\pi f t) \quad \text{with strain} \quad \epsilon_{zz}(t) = 1 - \frac{z(t)}{z_0}, \quad (2.2)$$

where  $z_0$  is the initial box length and  $z_f$  is the box length at maximum strain, respectively, and  $f = T^{-1}$  is the frequency. The maximum deformation is reached after half a period  $t = T/2$ , and the maximum strain-rate applied during the deformation is  $\dot{\epsilon}_{zz}^{\max} = 2\pi f(z_0 - z_f)/(2z_0) = \pi f(z_0 - z_f)/z_0$ . The co-sinusoidal law allows for a smooth start-up and finish of the motion so that shocks and inertia effects are reduced.

Different strain-control modes are possible, like homogeneous strain-rate control for each time-step, applied to all particles and the walls, or swelling instead of isotropic compression, as well as pressure-control of the (virtual) walls. However, this is not discussed, since it had no effect for the simple model used here, and for quasi-static deformations applied. For more realistic contact models and large strain-rates, the modes of strain- or stress-control have to be re-visited and carefully studied.

## 2.3 Preparation and test procedure

In this section, we describe first the sample preparation procedure and then the method for implementing the isotropic, uniaxial and deviatoric element test simulations. For convenience, the tensorial definitions of the different modes will be based on their respective strain-rate tensors. For presenting the numerical results, we will use the true strain as defined in section 2.4.2.

### 2.3.1 Initial Isotropic preparation

Since careful, well-defined sample preparation is essential in any physical experiment to obtain reproducible results [40], the preparation consists of three elements: (i) randomization,

(ii) isotropic compression, and (iii) relaxation, all equally important to achieve the initial configurations for the following analysis. (i) The initial configuration is such that spherical particles are randomly generated in a 3D box, with low density and rather large random velocities, such that they have sufficient space and time to exchange places and to randomize themselves. (ii) This granular gas is then isotropically compressed in order to approach a direction independent configuration, to a target volume fraction  $v_0 = 0.640$ , slightly below the jamming volume fraction  $v_c \approx 0.665$ , i.e. the transition point from fluid-like behavior to solid-like behavior [105, 106, 117, 164]. (iii) This is followed by a relaxation period at constant volume fraction to allow the particles to fully dissipate their energy and to achieve a static configuration in mechanical equilibrium.

Isotropic compression (negative strain-rate in our convention) can now be used to prepare further initial configurations at volume fractions  $v_i$ , with subsequent relaxation, so that we have a series of different initial isotropic configurations, achieved during loading and unloading, as displayed in Fig. 2.1. Furthermore, it can be considered as the isotropic element test [51]. It is realized by a simultaneous inward movement of all the periodic boundaries of the system, with strain-rate tensor

$$\dot{\mathbf{E}} = \dot{\epsilon}_v \begin{pmatrix} -1 & 0 & 0 \\ 0 & -1 & 0 \\ 0 & 0 & -1 \end{pmatrix},$$

where  $\dot{\epsilon}_v (> 0)$  is the rate amplitude applied to the walls until the target volume fraction is achieved.

A general schematic representation of the procedure for implementing the isotropic, uniaxial and deviatoric deformation tests is shown in Fig. 2.2. The procedure can be adapted for other non-volume conserving and/or stress-controlled modes (e.g., bi-axial, tri-axial and isobaric). One only has to use the same initial configuration and then decide which deformation mode to use, as shown in the figure under “other deformations”. The corresponding schematic plots of deviatoric strain  $\epsilon_d$  as a function of volumetric strain  $\epsilon_v$  are shown below the respective modes.

### 2.3.2 Uniaxial

Uniaxial compression is one of the element tests that can be initiated at the end of the “preparation”, after sufficient relaxation. The uniaxial compression mode in the tri-axial box is achieved by a prescribed strain path in the  $z$ -direction, see Eq. 2.2, while the other boundaries  $x$  and  $y$  are non-mobile. During loading (compression) the volume fraction is increased, like



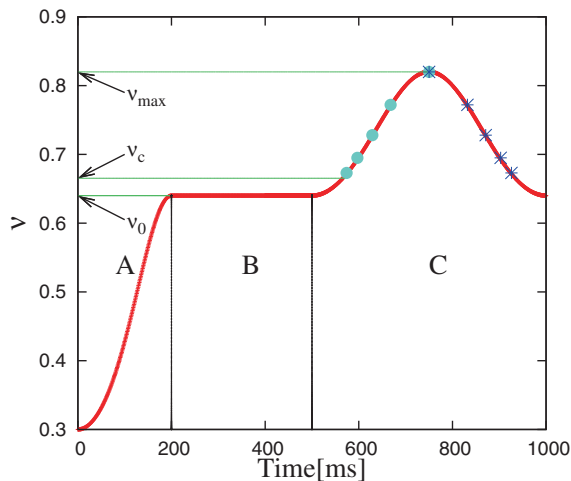


Figure 2.1: Evolution of volume fraction as a function of time. Region A represents the initial isotropic compression until the jamming volume fraction. B represents relaxation of the system and C represents the subsequent isotropic compression up to  $v_{\max} = 0.820$  and then decompression. Cyan dots represent some of the initial configurations, at different  $v_i$ , during the loading cycle and blue stars during the unloading cycle, which can be chosen for further study.

for isotropic compression, from  $v_0 = 0.64$  to a maximum volume fraction of  $v_{\max} = 0.820$  (as shown in region C of Fig. 2.1), and reverses back to the original volume fraction of  $v_0$  during unloading. Uniaxial compression is defined by the strain-rate tensor

$$\dot{\mathbf{E}} = \dot{\epsilon}_u \begin{pmatrix} 0 & 0 & 0 \\ 0 & 0 & 0 \\ 0 & 0 & -1 \end{pmatrix},$$

where  $\dot{\epsilon}_u$  is the strain-rate (compression  $> 0$  and decompression/tension  $< 0$ ) amplitude applied in the uniaxial mode. The negative sign (convention) of  $\dot{E}_{zz}$  corresponds to a reduction of length, so that tensile deformation is positive. Even though the strain is imposed only on the mobile “wall” in the  $z$ -direction, which leads to an increase of compressive stress on this wall during compression, also the non-mobile walls experience some stress increase due to the “push-back” stress transfer and rearrangement of the particles during loading, as discussed in more detail in the following sections. This is in agreement with theoretical expectations for materials with non-zero Poisson ratio. However, the stress on the passive walls is typically smaller than that of the mobile, active wall, as consistent with findings from laboratory element tests using the bi-axial tester [113, 178] or the so-called  $\lambda$ -meter [82, 83].

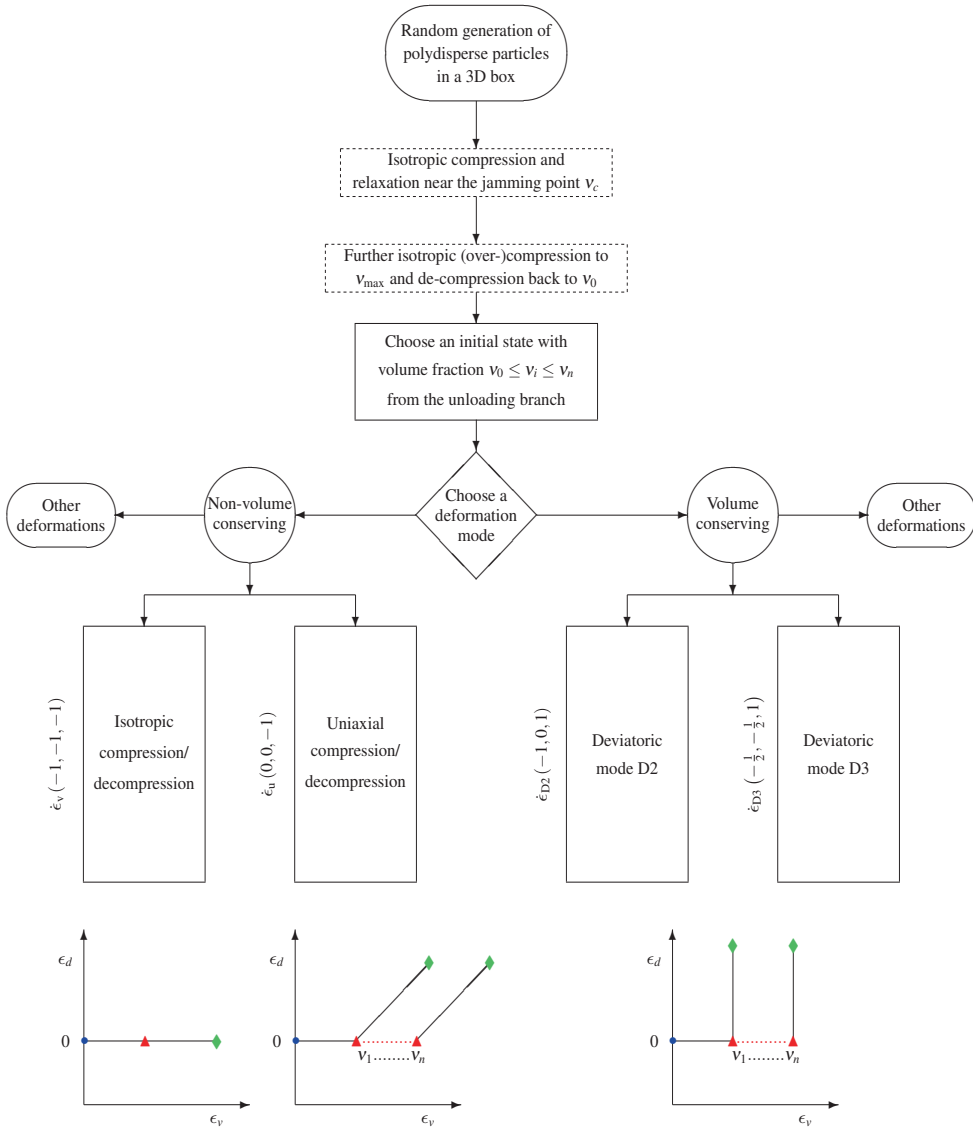


Figure 2.2: Generic schematic representation of the procedure for implementing isotropic, uniaxial and deviatoric deformation element tests. The isotropic preparation stage is represented by the dashed box. The corresponding plots (not to scale) for the deviatoric strain against volumetric strain are shown below the respective modes. The solid square boxes in the flowchart represent the actual tests. The blue circles indicate the start of the preparation, the red triangles represent its end, i.e. the start of the test, while the green diamonds show the end of the respective test.

### 2.3.3 Deviatoric

The preparation procedure, as described in section 2.3.1, provides different initial configurations with densities  $v_i$ . For deviatoric deformation element test, unless stated otherwise, the configurations are from the unloading part (represented by blue stars in Fig. 2.1), to test the dependence of quantities of interest on volume fraction, during volume conserving deviatoric (pure shear) deformations. The unloading branch is more reliable since it is much less sensitive to the protocol and rate of deformation during preparation [51, 78]. Then, two different ways of deforming the system deviatorically are used, not to mention numberless superpositions of these. The deviatoric mode D2 has the strain-rate tensor

$$\dot{\mathbf{E}} = \dot{\epsilon}_{D2} \begin{pmatrix} 1 & 0 & 0 \\ 0 & 0 & 0 \\ 0 & 0 & -1 \end{pmatrix},$$

where  $\dot{\epsilon}_{D2}$  is the strain-rate (compression  $> 0$ ) amplitude applied to the wall with normal in  $z$ -direction. We use the nomenclature D2 since two walls are moving, while the third wall is stationary.

The deviatoric mode D3 has the strain-rate tensor

$$\dot{\mathbf{E}} = \dot{\epsilon}_{D3} \begin{pmatrix} 1/2 & 0 & 0 \\ 0 & 1/2 & 0 \\ 0 & 0 & -1 \end{pmatrix}$$

where  $\dot{\epsilon}_{D3}$  is the  $z$ -direction strain-rate (compression  $> 0$ ) amplitude applied. In this case, D3 signifies that all the three walls are moving, with one wall twice as much (in opposite direction) as the other two, such that volume is conserved during deformation.

Note that the D3 mode is uniquely similar in “shape” to the uniaxial mode <sup>1</sup>, see Table 2.1, since in both cases two walls are controlled similarly. Mode D2 is different in this respect and thus resembles more an independent mode, so that we plot by default the D2 results rather than the D3 ones. The mode D2, with shape factor  $\zeta = 0$ , is on the one hand similar to the simple-shear situation, and on the other hand allows for simulation of the bi-axial experiment (with two walls static, while four walls are moving [113, 178]).

## 2.4 Averaged quantities

In this section, we present the general definitions of averaged microscopic and macroscopic quantities. The latter are quantities that are readily accessible from laboratory experiments,

<sup>1</sup>The more general, objective definition of deviatoric deformations is to use the orientation of the stresses (eigen-directions) in the deviatoric plane from the eigenvalues, as explored elsewhere [63, 159], since this is beyond the scope of this study.

Mode	Strain-rate tensor (main diagonal)	Deviatoric strain-rate (magnitude)	Shape factor $\zeta = (\epsilon_d^{(2)} / \epsilon_d^{(1)})$	Shape factor (when $-\epsilon_d$ is used)
ISO	$\dot{\epsilon}_v (-1, -1, -1)$	$\dot{\epsilon}_{\text{dev}} = 0$	n.a.	
UNI	$\dot{\epsilon}_u (0, 0, -1)$	$\dot{\epsilon}_{\text{dev}} = \dot{\epsilon}_u = \dot{\epsilon}_{zz}$	1	$-1/2$
D2	$\dot{\epsilon}_{D2} (1, 0, -1)$	$\dot{\epsilon}_{\text{dev}} = \sqrt{3}\dot{\epsilon}_{D2}$	0	0
D3	$\dot{\epsilon}_{D3} (1/2, 1/2, -1)$	$\dot{\epsilon}_{\text{dev}} = (3/2)\dot{\epsilon}_{D3}$	1	$-1/2$

Table 2.1: Summary of the deformation modes, and the deviatoric strain-rates  $\dot{\epsilon}_{\text{dev}}$ , as well as shape-factors,  $\zeta$ , for the different modes, in the respective tensor eigensystem, with eigenvalues  $\epsilon_d^{(1)}$  and  $\epsilon_d^{(2)}$  as defined in section 2.4.2.

whereas the former are often impossible to measure in experiments but are easily available from discrete element simulations.

### 2.4.1 Averaged microscopic quantities

In this section, we define microscopic parameters including the coordination number, the fraction of rattlers, and the ratio of the kinetic and potential energy.

#### Coordination number and fraction of rattlers

In order to link the macroscopic load carried by the sample with the microscopic contact network, all particles that do not contribute to the force network – particles with exactly zero contacts – are excluded. In addition to these “rattlers” with zero contacts, there may be a few particles with some finite number of contacts, for some short time, which thus also do not contribute to the mechanical stability of the packing. These particles are called dynamic rattlers [51], since their contacts are transient: The repulsive contact forces will push them away from the mechanically stable backbone [51]. Frictionless particles with less than 4 contacts are thus rattlers, since they cannot be mechanically stable and hence do not contribute to the contact network. In this work, since tangential forces are neglected, rattlers can thus be identified by just counting their number of contacts. This leads to the following abbreviations and definitions for the coordination number (i.e. the average number of contacts per particle) and fraction of rattlers, which must be re-considered for systems with

tangential and other forces or torques:

$$\begin{aligned}
 N & : \text{Total number of particles.} \\
 N_4 & := N_{C \geq 4} : \text{Number of particles with at least 4 contacts.} \\
 M & : \text{Total number of contacts} \\
 M_4 & := M_{C \geq 4} : \text{Total number of contacts of particles with at least 4 contacts.} \\
 C^r & := \frac{M}{N} : \text{Coordination number (simple definition).} \\
 C & := C^m = \frac{M_4}{N} : \text{Coordination number (modified definition).} \\
 C^* & := \frac{M_4}{N_4} = \frac{C}{1 - \phi_r} : \text{Corrected coordination number.} \\
 \phi_r & := \frac{N - N_4}{N} : \text{(Number) fraction of the rattlers.} \\
 v & := \frac{1}{V} \sum_{p \in N} V_p : \text{Volume fraction of the particles.}
 \end{aligned}$$

Some simulations results for the coordination numbers and the fraction of rattlers will be presented below, in subsection 2.5.1.

### Energy ratio and the Quasi-Static Criterion

Above the jamming volume fraction  $v_c$ , in mechanically stable static situations, there exist permanent contacts between particles, hence the potential energy (which is also an indicator of the overlap between particles) is considerably larger than the kinetic energy (which has to be seen as a perturbation).

The ratio of kinetic energy and potential energy is shown in Fig. 2.3 for isotropic compression from  $v_1=0.673$  to  $v_{\max}=0.820$  and back. The first simulation, represented by the solid red line, was run for a simulation time  $T = 5000 \mu\text{s}$  and the second (much slower) simulation, represented by the green dashed line was run for  $T = 50000 \mu\text{s}$ . For these, the maximum strain-rates are  $\dot{\epsilon}_{zz}^{\max} = 52.68[\text{s}^{-1}]$  and  $5.268[\text{s}^{-1}]$ , respectively. During compression, with increasing volume fraction, the energy ratio generally decreases and slower deformation by a factor of 10 leads to more than 100 times smaller energy ratios with stronger fluctuations. Most sharp increases of the energy ratio resemble re-organization events of several particles and are followed by an exponentially fast decrease (data not shown). The decrease is controlled by the interaction and dissipation time-scales and not by the shear rate; only due to the scaling of  $t_s$ , the decrease appears to be faster for the slower deformation. More explicitly, the rate of decay depends on material parameters only and is of the order of  $1/t_e$ . The low initial ratio of kinetic to potential energy ( $E_k/E_p < 0.001$ ) indicates that the system is in the jammed regime and is almost in the quasi-static state [158]. To ensure that the quasi-static

criterion is fulfilled in the simulations performed for the various deformation modes, all the simulations are run at a very small strain-rate. In this way, dynamic effects are minimized and the system is as close as feasible to the quasi-static state. For many situations, it was tested that a slower deformation did not lead to considerably different results. For the majority of the data presented, we have  $E_k/E_p \leq 10^{-3}$ . Lower energy ratios can be obtained by performing simulations at even slower rates but the settings used are a compromise between computing time and reasonably slow deformations.

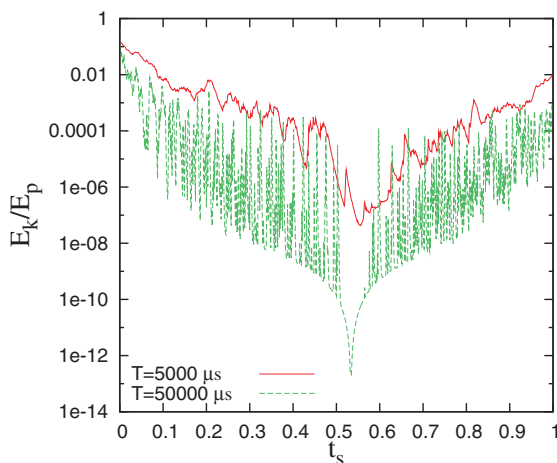


Figure 2.3: Comparison of the ratio of kinetic and potential energy in scaled time ( $t_s = t/T$ ) for two simulations, with different period of one compression-decompression cycle  $T$ , as given in the inset.

## 2.4.2 Averaged macroscopic quantities

Now the focus is on defining averaged macroscopic tensorial quantities – including strain-, stress- and fabric (structure) tensors – that reveal interesting bulk features and provide information about the state of the packing due to its deformation.

### Strain

For any deformation, the isotropic part of the infinitesimal strain tensor  $\epsilon_v$  is defined as:

$$\epsilon_v = \dot{\epsilon}_v dt = \frac{\epsilon_{xx} + \epsilon_{yy} + \epsilon_{zz}}{3} = \frac{1}{3} \text{tr}(\mathbf{E}) = \frac{1}{3} \text{tr}(\dot{\mathbf{E}}) dt, \quad (2.3)$$

where  $\epsilon_{\alpha\alpha} = \dot{\epsilon}_{\alpha\alpha} dt$  with  $\alpha\alpha = xx, yy$  and  $zz$  as the diagonal elements of the strain tensor  $\mathbf{E}$  in the Cartesian  $x, y, z$  reference system. The trace integral of  $3\epsilon_v$  denoted by  $3\epsilon_v$ , is the true

or logarithmic strain, i.e., the volume change of the system, relative to the initial reference volume,  $V_0$  [51].

Several definitions are available in literature [58, 159, 181] to define the deviatoric magnitude of the strain. For the sake of simplicity, we use the following definition of the deviatoric strain to account for all active and inactive directions in a tri-axial experiment, regardless of the deformation mode,

$$\epsilon_{\text{dev}} = \sqrt{\frac{(\epsilon_{xx} - \epsilon_{yy})^2 + (\epsilon_{yy} - \epsilon_{zz})^2 + (\epsilon_{zz} - \epsilon_{xx})^2}{2}}, \quad \epsilon_{xy} = \epsilon_{xz} = \epsilon_{yz} = 0, \quad (2.4)$$

since, for our tri-axial box, for all modes, the Cartesian coordinates resemble the eigensystem, with eigenvalues sorted according to magnitude  $\epsilon_d^{(1)} \geq \epsilon_d^{(2)} \geq \epsilon_d^{(3)}$ , which leaves the eigenvalue  $\epsilon_d^{(1)}$  as the maximal tensile eigenvalue, with corresponding eigen-direction, and  $\epsilon_{\text{dev}} \geq 0$  as the magnitude of the deviatoric strain<sup>2</sup>. The description of the tensor is completed by either its third invariant or, equivalently, by the shape factor  $\zeta$ , as given in Table 2.1. Note that the values for  $\zeta$  are during uniaxial loading, where compression is performed in the  $z$ -direction. The sorting will lead to different values,  $\zeta = -1/2$ , after the strain is reversed for both UNI and D3 modes.

## Stress

From the simulations, one can determine the stress tensor (compressive stress is positive as convention) components:

$$\sigma_{\alpha\beta} = \frac{1}{V} \left( \sum_{p \in V} m^p v_\alpha^p v_\beta^p - \sum_{c \in V} f_\alpha^c l_\beta^c \right), \quad (2.5)$$

with particle  $p$ , mass  $m^p$ , velocity  $v^p$ , contact  $c$ , force  $f^c$  and branch vector  $l^c$ , while Greek letters represent components  $x$ ,  $y$ , and  $z$  [93, 94]. The first sum is the kinetic energy tensor and the second involves the contact-force dyadic product with the branch vector. Averaging, smoothing or coarse graining [172] in the vicinity of the averaging volume,  $V$ , weighted according to the vicinity is not applied in this study, since averages are taken over the total volume. Furthermore, since the data in this study are quasi-static, the first sum can mostly be neglected.

The average isotropic stress (i.e. the hydrostatic pressure) is defined as:

$$P = \frac{\sigma_{xx} + \sigma_{yy} + \sigma_{zz}}{3} = \frac{1}{3} \text{tr}(\boldsymbol{\sigma}), \quad (2.6)$$

---

<sup>2</sup>The objective definition of the deviatoric strain defines it in terms of the eigenvalues  $\epsilon_d^{(1)}$ ,  $\epsilon_d^{(2)}$  and  $\epsilon_d^{(3)}$ , of the (deviatoric) tensor. However, since the global strain is given by the wall motion, the two definitions are equivalent for tri-axial element tests.

where  $\sigma_{xx}$ ,  $\sigma_{yy}$  and  $\sigma_{zz}$  are the diagonal elements of the stress tensor in the  $x$ ,  $y$  and  $z$  box-reference system and  $\text{tr}(\boldsymbol{\sigma})$  is its trace. The non-dimensional pressure [51] is defined as:

$$p = \frac{2\langle r \rangle}{3k} \text{tr}(\boldsymbol{\sigma}), \quad (2.7)$$

where  $\langle r \rangle$  is the mean radius of the spheres and  $k$  is the contact stiffness defined in section 2.2.

We define the deviatoric magnitude of stress (similar to Eq. (2.4) for deviatoric strain) as:

$$\sigma_{\text{dev}} = \sqrt{\frac{(\sigma_{xx} - \sigma_{yy})^2 + (\sigma_{yy} - \sigma_{zz})^2 + (\sigma_{zz} - \sigma_{xx})^2}{2}}, \quad (2.8)$$

which is always positive by definition neglecting the small contributions of  $\sigma_{xy}$ ,  $\sigma_{xz}$  and  $\sigma_{yz}$ . The direction of the deviatoric stress is carried by its eigen-directions, where stress eigenvalues are sorted like strain eigenvalues according to their magnitude. Eqs. (2.4) and (2.8) can easily be generalized to account for shear reversal using a sign convention taken from the orientation of the corresponding eigenvectors, or from the shape-factor, however, this will not be detailed here for the sake of brevity.

It is noteworthy to add that the definitions of the deviatoric stress and strain tensors are proportional to the second invariants of these tensors, e.g., for stress:  $\sigma_{\text{dev}} = \sqrt{3J_2}$ , which makes our definition identical to the von Mises stress criterion [43, 55, 159]<sup>3</sup>.

### Fabric (structure) tensor

Besides the stress of a static packing of powders and grains, the next most important quantity of interest is the fabric/structure tensor. For disordered media, the concept of the fabric tensor naturally occurs when the system consists of an elastic network, or a packing of discrete particles. The expression for the components of the fabric tensor is:

$$F_{\alpha\beta} = \langle F^p \rangle = \frac{1}{V} \sum_{p \in V} V^p \sum_{c=1}^N n_{\alpha}^c n_{\beta}^c, \quad (2.9)$$

where  $V^p$  is the particle volume which lies inside the averaging volume  $V$ , and  $n^c$  is the normal vector pointing from the center of particle  $p$  to contact  $c$ .  $F_{\alpha\beta}$  are thus the components of a symmetric rank two 3x3 tensor like the stress tensor. The isotropic fabric,  $F_v = \text{tr}(\mathbf{F})/3$ , quantifies the contact number density as studied in Ref. [51]. We assume that the structural anisotropy in the system is quantified (completely) by the anisotropy of fabric, i.e., the

<sup>3</sup>Different factors in the denominator of Eqs. (2.4) and (2.8) have been proposed in literature [58, 181] but they only result in a change in the maximum deviatoric value obtained. For consistency, we use the same factor  $\sqrt{1/2}$  for deviatoric stress and strain and a similar definition for the deviatoric fabric, see the next subsection.



deviatoric fabric. To quantify it, we define a scalar similar to Eqs. (2.4) and (2.8) as:

$$F_{\text{dev}} = \sqrt{\frac{(F_{xx} - F_{yy})^2 + (F_{yy} - F_{zz})^2 + (F_{zz} - F_{xx})^2}{2}}, \quad (2.10)$$

where  $F_{xx}$ ,  $F_{yy}$  and  $F_{zz}$  are the three diagonal components of the fabric tensor, again neglecting small  $F_{xy}$ ,  $F_{xz}$  and  $F_{yz}$ . The fabric tensor practically has only diagonal components with non-diagonal elements very close to zero, so that its eigen system is close to the Cartesian, as confirmed by eigen system analysis.

## Conclusion

Three macroscopic rank-two tensors were defined and will be related to microscopic quantities and each other in the following. The orientations of all the tensor eigenvectors show a tiny non-collinearity of stress, strain and fabric, which we neglect in the next sections, since we attribute it to natural statistical fluctuations. Furthermore, the shape factor defined for strain can also be analyzed for stress and fabric, as will be shown elsewhere.

## 2.5 Evolution of micro-quantities

In this section, we discuss the evolution of the microscopic quantities studied – including coordination number and fraction of rattlers – as function of volume fraction and deviatoric strain respectively, and compare these results for the different deformation modes.

### 2.5.1 Coordination number and fraction of rattlers

It has been observed [51] that under isotropic deformation, the corrected coordination number  $C^*$  follows the power law

$$C^*(\nu) = C_0 + C_1 \left( \frac{\nu}{\nu_c} - 1 \right)^\alpha, \quad (2.11)$$

where  $C_0 = 6$  is the isostatic value of  $C^*$  in the frictionless case. For the uniaxial unloading simulations, we obtain  $C_1 \approx 8.370$ ,  $\alpha \approx 0.5998$  and  $\nu_c^{\text{UNI}} \approx 0.6625$  as best fit parameters.

In Fig. 2.4, the evolution of the simple, corrected and modified coordination numbers are compared as functions of volume fraction during uniaxial deformation (during one loading and unloading cycle). The compression and decompression branches are indicated by arrows pointing right and left, respectively. The contribution to the contact number originating from

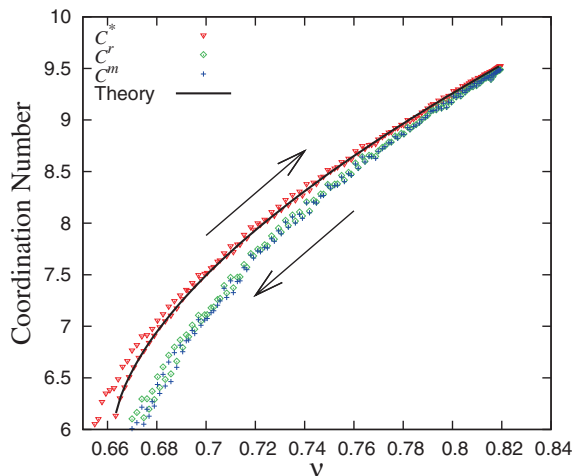


Figure 2.4: Comparison between coordination numbers using the simple ('+', blue), modified ('◇', green) and corrected ('▼', red) definitions. Data are from a uniaxial compression-decompression simulation starting from  $v_0 = 0.64 < v_c \approx 0.6625$ . The solid black line represents Eq. (2.11), with parameters given in the text, very similar to those measured in Ref. [51], see Table 2.2.

particles with  $C = 1, 2$  or  $3$  is small – as compared to those with  $C = 0$  – since  $C^r$  and  $C^m$  are very similar, but always smaller than  $C^*$ , due to the fraction of rattlers, as discussed below. The number of contacts per particle grows with increasing compression to a value of  $C^* \approx 9.5$  at maximum compression. During decompression, the contacts begin to open and the coordination number decreases and approaches the theoretical value  $C_0 = 6$ <sup>4</sup> at the critical jamming volume fraction after uniaxial de-compression  $v_c^{\text{UNI}} \approx 0.662$ . Note that the  $v_c^{\text{UNI}}$  value is smaller than  $v_c^{\text{ISO}} \approx 0.665$  reached after purely isotropic over-compression to the same maximal volume fraction. The coordination numbers are typically slightly larger in the loading branch than in the unloading branch, due to the previous over-compression.

In Fig. 2.5, we plot the corrected coordination number for deformation mode D2 as a function of the deviatoric strain for five different volume fractions. Two sets of data are presented for each volume fraction starting from different initial configurations, either from the loading or the unloading branch of the isotropic preparation simulation (cyan dots and blue stars in Fig. 2.1). Given initial states with densities above the jamming volume fraction, and due to the volume conserving D2 mode, the value of the coordination number remains practically constant. Only for the lowest densities, close to jamming, a slight increase (decrease) in  $C^*$

<sup>4</sup>The value,  $C_0 = 6$ , is expected since it is the isostatic limit for frictionless systems in three dimensions [51], for which the number of constraints (contacts) is twice the number of degrees of freedom (dimension) – in average, per particle – so that the number of unknown forces matches exactly the number of equations. ( $C_0$  is different from the minimal number for a mechanically stable sphere  $C_{\text{min}} = 4$  in 3D).

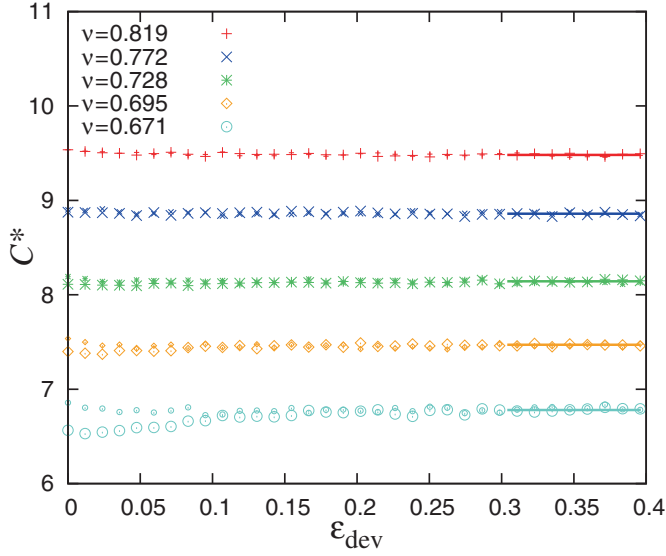


Figure 2.5: Evolution of coordination number with deviatoric strain for the D2 mode. Smaller symbols represent data with initial configuration from the loading branch of an isotropic simulation, while the larger symbols start from an initial configuration with the same volume fraction, but from the isotropic unloading branch. The horizontal line at the large strain of the dataset indicates an average after saturation at steady state.

can be seen, for initial states chosen from the unloading (loading) branch of the preparation step. However, both reach similar steady-state values after large strain, as indicated by the solid lines. Hence, for further analysis, unless otherwise stated, we will only present the steady-state values of micro- and macro-quantities from deviatoric modes D2 and D3.

The re-arrangement of the particles during shear thus does not lead to the creation (or destruction) of many contacts – in average. There is no evidence of the change of average contacts after 10 – 15 percent of strain. However, close to jamming, a clear dependence of  $C^*$  on the initial state exists, which vanishes in steady state when one gets saturated values in micro- and macro-quantities, after large enough strain. For the same volume fraction, we evidence a range of  $C_{oc}^* \leq C_s^* \approx C_{ic}^*$ , where the subscripts refer to over-compressed, steady, and initially compressed states, respectively. The coordination number (or alternatively the contact number density, as related to the trace of the fabric tensor) is thus a control parameter closely linked to the volume fraction that contains more information about the structure than  $v$  (above the jamming volume fraction), see Refs. [85, 86] and references therein.

In Fig. 2.6, the corrected coordination number is shown as a function of volume fraction for the purely isotropic- the uniaxial unloading- and the large strain deviatoric deformation

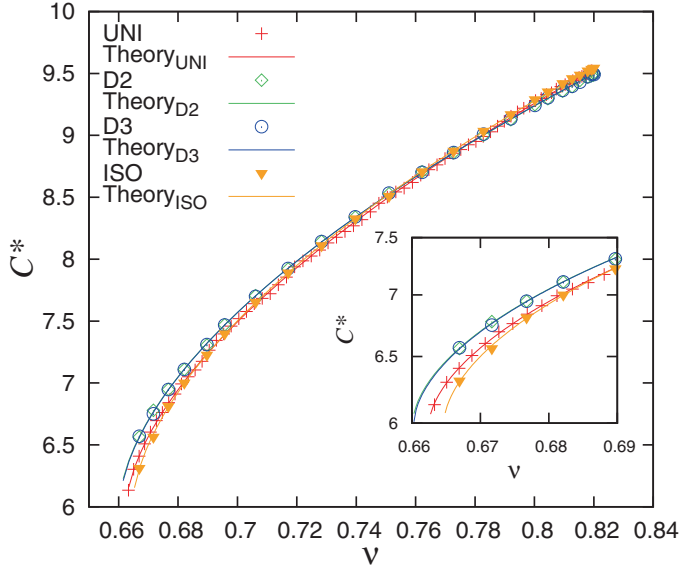


Figure 2.6: Evolution of the corrected coordination number as a function of volume fraction during unloading for all modes. The symbols represent the respective simulation data while the solid lines represent the analytical equation according to Eq. (2.11) with the respective values of  $C_0$ ,  $C_1$ ,  $\alpha$  and  $v_c$  shown in Table 2.2. Inset shows the corrected coordination number at lower volume fractions closer to jamming.

datasets. Different symbols show the values of  $C^*$  for the different deformation modes for various volume fractions. Interestingly, the power law for the coordination number, derived from isotropic data, describes well also the uniaxial and deviatoric data, with coefficients given in Table 2.2. This suggests that (for the cases considered), when particles are frictionless, the coordination number is independent on the deviatoric strain, in steady state, and the limit values can be approximated by Eq. (2.11), as proposed for simple isotropic deformation. The distinction between the modes at the small (isotropic) strain region is shown as zoom in the inset of Fig. 2.6. The mixed mode (uniaxial) is bordered on both sides by the pure modes, namely isotropic and deviatoric (D2 and D3 cannot be distinguished), indicating that the two pure modes are limit states or extrema for  $C^*$ . Alternatively, the range in  $C^*$  values can be seen as caused by a range in  $v_c$ , with  $v_c^{\text{ISO}} > v_c^{\text{UNI}} > v_c^{\text{DEV}}$ , which represent the maximal jamming volume fraction after previous (isotropic, strong) over-compression, the intermediate jamming volume fraction after (mixed mode) deformation, and the minimal jamming volume fraction after large deviatoric strain, respectively, with  $v_c^{\text{ISO}} \approx 0.6646$  and  $v_c^{\text{DEV}} \approx 0.6602$ . In other words, deviatoric deformations reduce the jamming volume fraction of the packing, i.e., can disturb and dilate a dense (over-compressed) packing so that it becomes less efficiently packed. This is opposite to isotropic over-compression, where

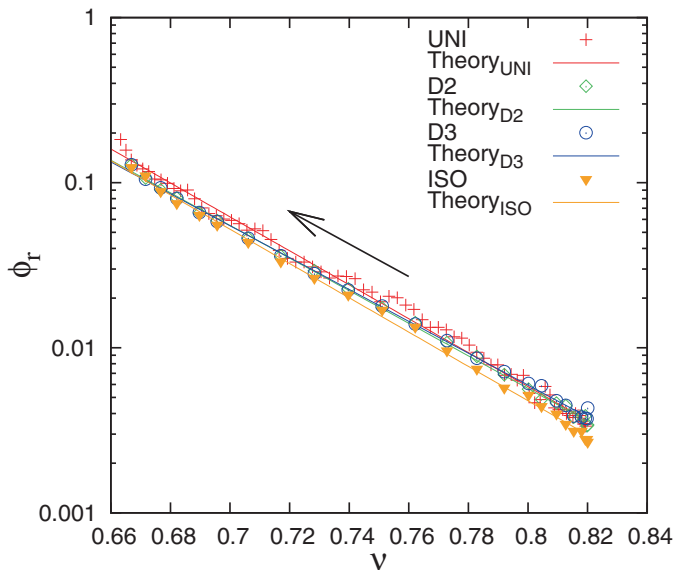


Figure 2.7: Evolution of the fraction of rattlers as a function of volume fraction during unloading for all modes. The symbols represent the respective simulation data. The solid lines are the analytical fits of Eq. (2.12) for each mode with the values of fit parameters  $\phi_c$  and  $\phi_v$  for each mode shown in Table 2.2. The arrow indicates the unloading direction.

after unloading, the jamming volume fraction is higher, i.e., the system is more efficiently packed/structured. This behavior is qualitatively to be expected for frictional particles, however, this is to our knowledge the first time that this small but systematic range of jamming volume fractions is reported for frictionless packings – where the most relevant and only mechanism is structural reorganization, as will be discussed further in section 2.6.1.

As related interesting microscopic quantity, we recall the analytical expression for the fraction of rattlers proposed in Ref. [51]:

$$\phi_r(\nu) = \phi_c \exp \left[ -\phi_v \left( \frac{\nu}{\nu_c} - 1 \right) \right], \quad (2.12)$$

where the fit parameters for the different deformation modes are given in Table 2.2, and  $\nu_c \approx 0.6646$  is obtained from extrapolation of  $C^*$  to the isostatic coordination number  $C_0 = 6$ . In Fig. 2.7, the evolution of the fraction of rattlers is plotted as a function of volume fraction for both isotropic and uniaxial unloading as well as for steady state deviatoric mode simulations. We then compare these with the prediction/fit (solid lines) from the exponential decay equation, Eq. (2.12). Interestingly, in contrast to the coordination number, the fraction of rattlers displays strongest differences at the highest densities ( $\nu = 0.82$  in Fig. 2.7), and it is lowest during isotropic unloading, as compared to the steady state deviatoric mode

$C^*$	$C_1$	$\alpha$	$v_c$
ISO [51]	$8 \pm 0.5$	$0.58 \pm 0.05$	$0.66 \pm 0.01$
ISO	8.2720	0.5814	0.6646
UNI	8.370	0.5998	0.6625
D2	7.9219	0.5769	0.6601
D3	7.9289	0.5764	0.6603
$\phi_r$	$\phi_c$	$\phi_v$	
ISO [51]	$0.13 \pm 0.03$	$15 \pm 2$	
ISO	0.1216	15.8950	
UNI	0.1507	15.6835	
D2	0.1363	15.0010	
D3	0.1327	14.6813	
$p^*$	$p_0$	$\gamma_p$	$v_c$
ISO [51]	0.0418	0.110	0.666
ISO	0.04172	0.06228	0.6649
UNI	0.04006	0.03270	0.6619
D2	0.03886	0.03219	0.6581
D3	0.03899	0.02893	0.6583

Table 2.2: Fit parameters for the analytical predictions of coordination number, fraction of rattlers, and pressure in Eqs. (2.11) with  $C_0 = 6$ , (2.12) and (2.14), respectively. For the  $\phi_r$  fits,  $v_c$  is used from the  $C^*$  fits for the different deformation modes. The first rows of isotropic data are from Ref. [51], for various polydispersities and also during unloading, but for different over-compression.

situations, and somewhat higher during uni-axial unloading. The difference between the modes is smallest close to jamming. For uniaxial simulations, at the end of unloading, close to  $v_c^{\text{UNI}}$ , a considerable fraction (almost 20 percent) of the total number of particles are rattlers that do not contribute to the stability of the network. For higher densities, a strong exponential decay is evidenced.<sup>5</sup>

To better understand the peculiar behavior of the systems jamming volume fraction under the different modes of deformation, some macroscopic quantities are studied next.

## 2.6 Evolution of macro-quantities

In this section, we discuss results for the evolution of the macroscopic tensor quantities stress and fabric, as defined in section 2.4.2. For clarity, we split them in isotropic and deviatoric parts in subsections 2.6.1 and 2.6.2, respectively.

### 2.6.1 Evolution of macro-quantities: Isotropic part

#### Isotropic pressure

In this section, the relation between pressure and volume fraction is studied. First, we consider the contact deformations, since the force is related to the contact overlap/deformation  $\delta_c$ , and stress is proportional to the force. The infinitesimal change  $d\langle\Delta\rangle_c = 3D\epsilon_v$ , of the normalized average overlap,  $\Delta_c = \delta_c/\langle r \rangle$ , can be related to the volumetric strain under the simplifying assumption of uniform, homogeneous deformation in the packing. As defined in subsection 2.4.2,  $\epsilon_v = \epsilon_{ii}/3$  is the trace of the infinitesimal strain tensor increment, and  $D \approx 0.425$  is a proportionality constant that depends on the size distribution and can be readily obtained from the average overlap and volume fraction (data not shown), see Eq. (2.13). The integral of  $\epsilon_v$ , denoted by  $\mathcal{E}_v$ , is the true or logarithmic volume change of the system, relative to the reference volume  $V_{\text{ref}}$ . This is chosen, without loss of generality, at the critical jamming volume fraction  $v_{\text{ref}} = v_c$ , so that the average normalized overlap is [51]

$$\langle\Delta\rangle_c = -D \int_{V_0}^V \epsilon_v = -D\mathcal{E}_v = D \ln \left( \frac{V}{V_c} \right). \quad (2.13)$$

As in Eq. (2.7), see Refs. [51, 141] for details, the non-dimensional pressure is:

$$p = \frac{2\langle r \rangle}{3k} \text{tr}(\boldsymbol{\sigma}) = p_0 \frac{vC}{v_c} (-\mathcal{E}_v) [1 - \gamma_p(-\mathcal{E}_v)], \quad (2.14)$$

---

<sup>5</sup>The sharp jump observed in Ref. [51] at the jamming transition during unloading is not seen here because the system remains above the jammed state. Interestingly, the simulation data for the uniaxial and deviatoric mode all collapse close to the (isotropic) exponential prediction.

and the scaled pressure is:

$$p^* = \frac{pV_c}{\nu C} = p_0(-\varepsilon_\nu)[1 - \gamma_p(-\varepsilon_\nu)] \quad (2.15)$$

where  $p_0 \approx 0.04006$ ,  $\gamma_p \approx 0.03270$ , and the critical volume fraction  $\nu_c \approx 0.6619$  are fit parameters to pressure for uniaxial unloading. Combining the quasi-static parts of Eqs. (2.5) and (2.14), leads to the proportionality  $p \propto \nu C \Delta_c$ , which makes the  $p$  a measure for the average overlap relative to the average particle diameter, and  $p^*$  scales all  $p$  on the same reference density, i.e., the jamming density.

Note that the critical volume fraction  $\nu_c \approx 0.6625$  obtained from extrapolation of  $C^*$  to the isostatic coordination number  $C_0 = 6$  is very close to that obtained from Eq. (2.14). When fitting all modes with pressure, one confirms again that  $\nu_c^{\text{UNI}}$  falls in between the pure modes ( $\nu_c^{\text{ISO}}$  and  $\nu_c^{\text{DEV}}$ ), with all fits quite consistent within each mode, as summarized in Table 2.2.

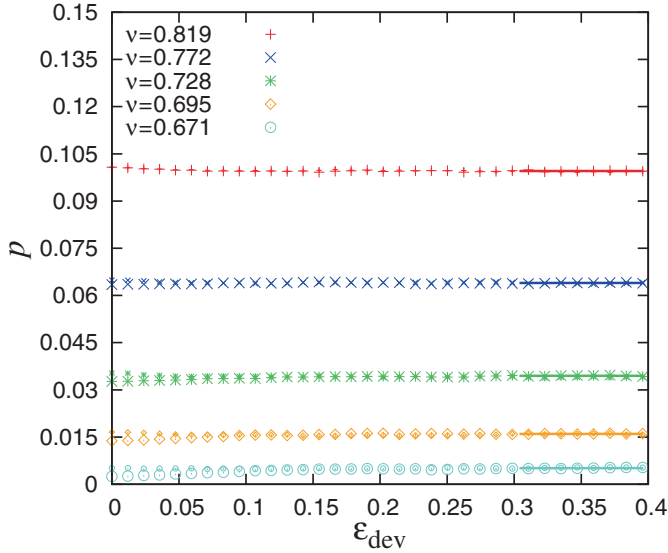


Figure 2.8: Evolution of (non-dimensional) pressure, Eq. (2.7), with deviatoric strain for the D2 deformation mode, at different initial volume fractions  $\nu_i$ . Small and large symbols represent simulations starting with initial isotropic configurations from the loading and unloading branch, respectively. The horizontal line at the large strain of the dataset indicates an average value of the pressure after saturation at steady state.

In Fig. 2.8, we plot the total (non-dimensional) pressure  $p$  for deformation mode D2 as a function of the deviatoric strain for different volume fractions. Above the jamming volume fraction, the value of the pressure remains practically constant except for the lowest densities close to jamming where a slight increase in  $p$  can be seen when initial states are chosen from



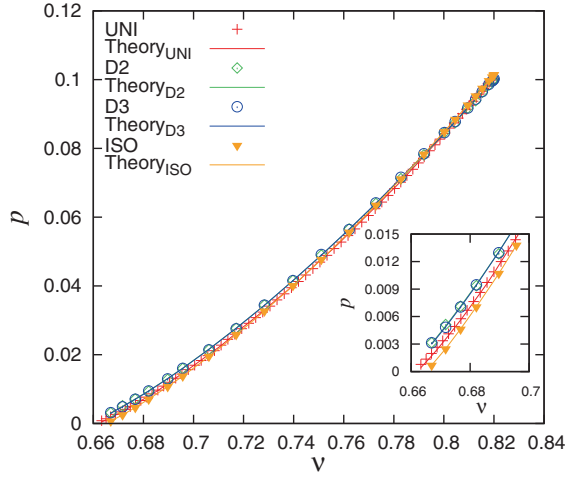


Figure 2.9: Total (non-dimensional) pressure, Eq. (2.14), plotted as function of volume fraction for the uniaxial and isotropic datasets during unloading, and for the D2/D3 deviatoric modes after large strain. The solid lines are the analytical fits of Eq. (2.14), for each mode, with parameters  $p_0$ ,  $\gamma_p$  and  $v_c$  shown in Table 2.2.

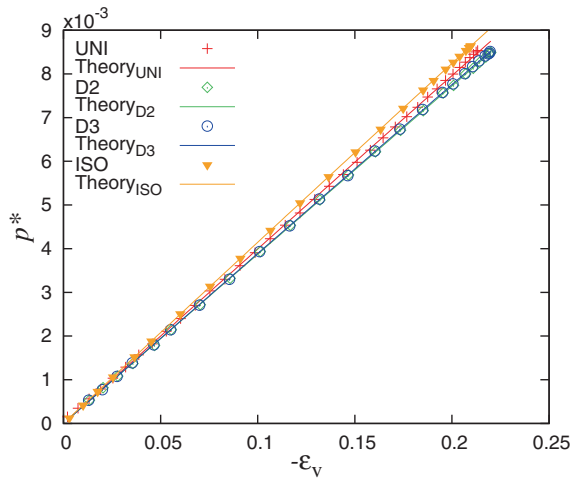


Figure 2.10: The scaled pressure plotted against the (negative) volumetric strain, for the same data as presented in Fig. 2.9. The solid lines are the prediction from Eq. (2.15), using the fits of  $p$  and  $C$  for each mode.

the unloading branch of isotropic modes (blue stars in Fig. 2.1), whereas a slight decrease in  $p$  is observed for initial states chosen from the loading branch (cyan dots in Fig. 2.1). Independent of the initial configuration, pressure reaches the same steady state value at larger

strains, very similar to the behavior of the coordination number.

Fig. 2.9 shows the total pressure as a function of the volume fraction for isotropic and uniaxial unloading. The deviatoric mode D2 and D3 data, are obtained after large deviatoric strain, as shown for D2 in Fig. 2.8. The pressure increases non-linearly during loading (data not shown) until the predetermined maximum volume fraction is reached [51], and also during unloading, the pressure decays non-linearly. Due to the linear contact model, this can be directly related to contact number density, i.e., the isotropic fabric, which quantifies the isotropic, direction independent changes of structure due to re-arrangements and closing/opening of contacts.

In Fig. 2.10, we plot the scaled pressure defined in Eq. (2.15) against the volumetric strain from the same data as in Fig. 2.9. The three datasets almost collapse for small strain. For increasing densities (larger  $-\varepsilon_v$ ) the isotropic mode scaled pressure is considerably larger than the uniaxial and the deviatoric datasets, where again the uniaxial data fall in between isotropic and deviatoric data sets. This is consistent with the fact that the uniaxial mode is a superposition of the purely isotropic and deviatoric deformation modes and resembles very much the behavior of  $C^*$ .

The dependence of pressure on isotropic strain can be interpreted in relation to sample history. The deviatoric modes (D2 or D3) lead to dilatancy and thus to the highest steady state pressure, with respectively lowest  $v_c^{\text{DEV}}$ ; the isotropic mode is strictly compressive, with the lowest pressure, after over-compression, during unloading, with respectively the highest  $v_c^{\text{ISO}}$ ; and the uniaxial mode is mixed and thus interpolates between the two other modes.

The apparent collapse of all scaled  $p^*$  data at small strain, with similar pre-factors  $p_0 \approx 0.040$ , is interesting since, irrespective of the applied deformation mode – purely isotropic, uniaxial, and D2 or D3 deviatoric, it boils down to a linear relation between  $p^*$  and  $-\varepsilon_v$  with a small quadratic correction – not showing small non-linear powers as proposed earlier, e.g. in Ref. [105]. The nonlinearity in  $1 - v/v_c$  is hidden in  $vC$ , which is actually proportional to the isotropic fabric.

### Isotropic fabric

The random, isotropic orientation of the contact directions in space was studied in detail in Refs. [51, 141] and is referred to as the contact number density, with  $\text{tr}(\mathbf{F}) = g_3 vC$ , where  $g_3$  is of order unity and depends only on the size-distribution (for our case with  $w = 3$ , one has  $g_3 \approx 1.22$ ). Note that  $vC$  directly connects to the dimensionless pressure which, remarkably, hides the corrected coordination number and the fraction of rattlers in the relation  $C = (1 - \phi_r)C^*$ , which fully determines  $\text{tr}(\mathbf{F})$ .

## 2.6.2 Evolution of macro-quantities: Deviatoric part

In the following, we present the evolution of the deviatoric stress ratio (which can be seen as a measure of stress anisotropy) and also the evolution of the structural anisotropy, both as a function of the deviatoric strain. In this sub-section, we will mostly present the raw data from deviatoric and uniaxial simulations and their phenomenology, together with the fits of the former (D2 element tests) to calibrate the constitutive model. The constitutive model, as presented in Refs. [98, 101], is presented later in section 2.7, and is used to predict the stress and fabric response under uniaxial (UNI) loading. By doing this, we do not fit the uniaxial tests but qualitatively predict the evolution of stress and fabric.

### Deviatoric Stress

The deviatoric stress ratio ( $s_{\text{dev}} = \sigma_{\text{dev}}/P$ ) quantifies the (stress) anisotropy [78]. The loading response of the deviatoric stress ratio for the deformation mode D2, as function of the deviatoric strain, is shown in Fig. 2.11. Some exemplary results of this dimensionless stress ratio are shown for different volume fractions. The stress grows initially linearly with applied strain until an asymptote (of maximum stress anisotropy) is reached where it remains fairly constant. The reached asymptote, is referred to as the deviatoric steady state and the initial increase and the approach are well fitted by the exponential relation proposed in Refs. [98, 101] for the bi-axial box. Interestingly, the stress response observed from mode D3 (not shown) follows practically the same path as for mode D2, as discussed in section 2.7.

In Fig. 2.12, exemplary uniaxial (compression) simulations are shown, beginning from different initial volume fractions, to a maximum volume fraction defined by similar strain amplitudes. Unlike the deviatoric modes discussed previously, the evolution of the deviatoric stress ratio during uniaxial compression leads to larger fluctuations that do not allow the clear observation of a possible increase or decrease in the saturation regime. This difference is because the uniaxial deformation mode is not a volume conserving mode with continuously increasing pressure in contrast, for example to a similar mode D3, where  $\sigma_{zz}$  is increasing and  $\sigma_{xx} \approx \sigma_{yy}$  are decreasing, such that the pressure remains (almost) constant. The corresponding solid lines in the plot represent the predictions of the constitutive relations in Eq. (2.17), with the parameters obtained from the deviatoric modes, D2 and D3, as explained in detail in section 2.7.

Moreover, as the deviatoric strains increase from the uniaxial simulations for different volume fractions, the deviatoric stress ratios,  $s_{\text{dev}}$  also increase (sometimes with a maximum). For smaller volume fractions the values are higher, similar to what we observe in Fig. 2.11. It is astonishing that uniaxial deformation for different initial volume fractions, lead to convergence and collapse after 7.5% deviatoric strain. This feature of the uniaxial simulations is also captured by the anisotropy model in section 2.7.3.

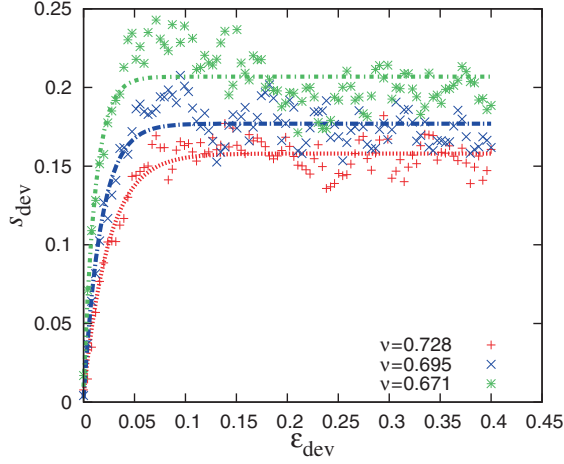


Figure 2.11: Deviatoric stress ratio ( $s_{\text{dev}} = \sigma_{\text{dev}}/P$ ) plotted against deviatoric strain from the D2 deformation mode for initial volume fractions  $v_i$  during unloading, from which the simulations were performed, as given in the inset. The symbols ('\*', 'x' and '+') are the simulation data while the solid lines through them represent a fit to the data using Eq. (2.17).

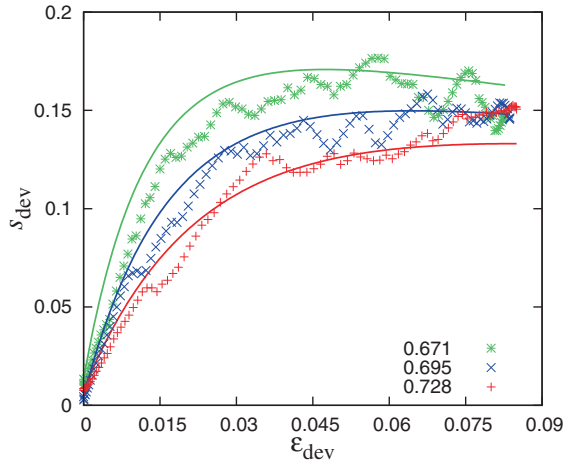


Figure 2.12: Deviatoric stress ratio plotted against deviatoric strain from the uniaxial compression mode data, for different initial volume fractions  $v_i$  during unloading, from which the uniaxial deformations were initiated, as given in the inset. The symbols ('\*', 'x' and '+') are the simulation data while the solid lines represent the prediction, Eq. (2.17).

### Deviatoric fabric evolution

The evolution of the deviatoric fabric,  $F_{\text{dev}}$  as a function of the deviatoric strain is shown in Fig. 2.13 for mode D2 simulations with three different volume fractions. It builds up from

different random, small initial values to different maximum values. The deviatoric fabric builds up faster at lower volume fractions like the  $G^{\text{oct}}/P$  ratio, where  $G^{\text{oct}}$  is the octahedral shear modulus [23], and the maximal values also are larger for smaller volume fractions. The evolution of the deviatoric fabric for the D3 mode is not shown, since it is practically identical to the D2 mode, implying that the fabric evolution is pretty much insensitive to the deviatoric deformation protocol employed, as was observed before also for the stress ratio. The saturation of the maximum deviatoric fabric for the deviatoric deformation data shown in Fig. 2.13 is well defined, and the approach is very similar to that of  $s_{\text{dev}}$  in Fig. 2.11.

Figure 2.14 shows the evolution of the deviatoric fabric for the uniaxial deformation mode from the same simulations as presented in section 2.6.2. The deviatoric fabric builds up as the deviatoric strain (and the volume fraction) increases. After a few percent of deviatoric strain, it begins to saturate even though a slight decreasing trend is seen towards the end of the simulation. The convergence of the deviatoric stress after large strain for different volume fractions, as seen in Fig. 2.12, does not appear so clearly for the deviatoric fabric. The solid lines representing the theoretical prediction of the constitutive relation in Eq. (2.17) agree qualitatively well, but over-predict the deviatoric fabric for larger strains. Their analytical form and parameters involved will be discussed in detail in section 2.7 below.

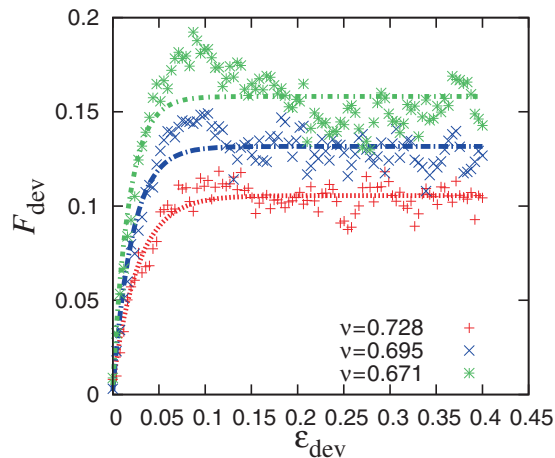


Figure 2.13: Deviatoric fabric plotted against deviatoric strain from the D2 deformation simulations of Fig. 2.11. The symbols ('\*', 'x' and '+') are the simulation data while the solid lines through them represent a fit to the data using Eq. (2.18).

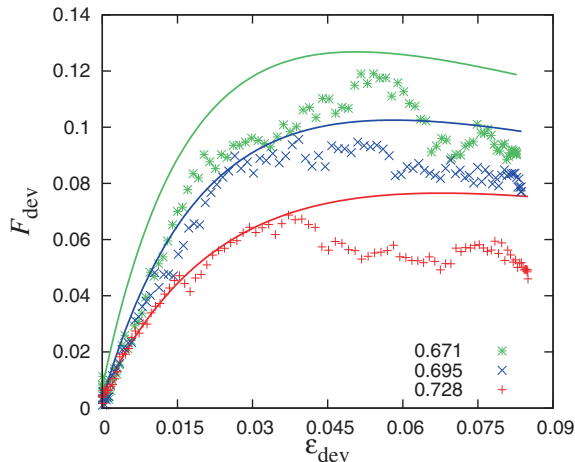


Figure 2.14: Deviatoric fabric plotted against deviatoric strain from the uniaxial deformation simulations in Fig. 2.12. The symbols ('\*', 'x' and '+') are the simulation data while the solid lines through them represent a prediction to the data using Eq. (2.18).

## 2.7 Theory: Macroscopic evolution equations

Constitutive models are manifold and most standard models with wide application fields, like elasticity, elasto-plasticity, or fluid-/gas-models of various kinds, were applied also to granular flows – sometimes with success, but typically only in a very limited range of parameters and flow conditions; for overviews see e.g. Ref. [98, 111]. Only for rapid granular flows, the framework of kinetic theory is an established tool with quantitative predictive value – but it is hardly applicable in dense, quasi-static and static situations [95]. Further models, like hyper- or hypo-elasticity, are complemented by hypo-plasticity and the so-called granular solid hydrodynamics, where the latter provide incremental evolution equations for the evolution of stress with strain, and involve limit-states [107], instead of a plastic yield surface as in plasticity theory, where a strict split between elastic and plastic behavior seems invalid in granular materials, see e.g. Ref. [11]. More advanced models involve so-called non-associated / non co-axial flow rules, where some assumptions on relations between different tensors are released, see e.g. Ref. [159]. While most of these theories can be or have been extended to accommodate anisotropy of the micro-structure, only very few models account for an independent evolution of the microstructure as for example Refs. [98, 151], as found to be important in this study and many others.

In the following, we use the anisotropy constitutive model, as proposed in Refs. [81, 98, 101],

generalized for a  $\mathcal{D}$ -dimensional system:

$$\begin{aligned}\delta P &= \mathcal{D}B\delta\epsilon_v + AS\delta\epsilon_{\text{dev}}, \\ \delta\sigma_{\text{dev}} &= A\delta\epsilon_v + \mathcal{D}G^{\text{oct}}S\delta\epsilon_{\text{dev}}, \\ \delta A &= \beta_A \text{sign}(\delta\epsilon_{\text{dev}})(A^{\text{max}} - A)\delta\epsilon_{\text{dev}}.\end{aligned}\tag{2.16}$$

In its simplest form, the model involves only three moduli: the classical bulk modulus  $B$  [51], the octahedral shear modulus  $G^{\text{oct}}$ , and the new variable ‘‘anisotropy modulus’’  $A$ , evolving independently of stress due to deviatoric strain. Due to  $A$ , the model provides a cross coupling between the two types of stress and strain in the model, namely the hydrostatic and the shear (deviatoric) stresses react to both isotropic and deviatoric strains.  $S = (1 - s_{\text{dev}}/s_{\text{dev}}^{\text{max}})$  is an abbreviation for the stress isotropy. The parameter  $s_{\text{dev}}^{\text{max}}$  resembles the macroscopic friction and  $\beta_s$  is the growth rate of  $s_{\text{dev}} = \sigma_{\text{dev}}/P$  with deviatoric strain  $\epsilon_{\text{dev}}$ . The parameters  $A^{\text{max}}$  in the evolution equation of  $A$  represents the maximum anisotropy that can be reached at saturation, and  $\beta_A$  determines how fast the asymptote is reached (growth rate). Both  $A^{\text{max}}$  and  $\beta_A$  are model parameters for the anisotropy modulus and can be extracted from fits to the macroscopic, average simulation results. Note that the evolution of  $A$  is assumed to be kinematic, i.e., not explicitly dependent on pressure, but there is a possible volume fraction dependence of  $\beta_A$  and  $A^{\text{max}}$ , as detailed below.

In the following, we test the proposed model by extracting the model parameters from various volume conserving deviatoric simulations as a function of volume fraction  $v$ . The calibrated model is then used to predict the uniaxial deformation behaviour (see the previous section). The theory will be discussed elsewhere in more detail [81, 102].

In short, it is based on the basic postulate: There is an independent evolution of stress and structure possible. It comes together with some simplifying assumptions as:

- (i) the new macroscopic field  $A$  is proportional to the microscopic rank-two deviatoric fabric  $F_{\text{dev}}$ , so that they have the same non-dimensional growth rates  $\beta_F = \beta_A$ ;
- (ii) both  $A$  and  $s_{\text{dev}}$  – to lowest order, i.e., neglecting additional (missing) terms in Eqs. (2.16) – approach their limit states exponentially fast;
- (iii) only one anisotropy modulus  $A$  is sufficient (valid in 2D, questionable in 3D, possibly  $A_1$  and  $A_2$ ).

All these lead to Eqs. (2.17) and (2.18) below. (We use these two equations as empirical fit functions, which turned out to be special cases of an advanced constitutive model with anisotropy, and use the fit-result to predict one other solution of the (simplified) theory.)

### 2.7.1 Reduced theoretical model

The reduced model thus consists of two evolution equations for the deviatoric stress ratio  $s_{\text{dev}}$ , related to the mobilized macroscopic friction, and the deviatoric fabric  $F_{\text{dev}}$ , based on DEM observations in 2D, see Ref. [87, 89]. For volume conserving pure shear, Figs. 2.11 and 2.13 show that  $s_{\text{dev}}$  and  $F_{\text{dev}}$  grow non-linearly until they approach exponentially a constant value at steady state, with fluctuations, where the material can be indefinitely sheared without further change. As discussed in Ref. [98], the coupled evolution equations (2.16) are (with above assumptions) consistent with  $s_{\text{dev}}$  approximated by:

$$s_{\text{dev}} = s_{\text{dev}}^{\text{max}} - (s_{\text{dev}}^{\text{max}} - s_{\text{dev}}^0) e^{-\beta_s \epsilon_{\text{dev}}}, \quad (2.17)$$

where  $s_{\text{dev}}^0$  and  $s_{\text{dev}}^{\text{max}}$  represent the initial and maximum values of  $s_{\text{dev}}$  and  $\beta_s$  is its growth rate. Similarly, the deviatoric fabric is approximated by:

$$F_{\text{dev}} = F_{\text{dev}}^{\text{max}} - (F_{\text{dev}}^{\text{max}} - F_{\text{dev}}^0) e^{-\beta_F \epsilon_{\text{dev}}}, \quad (2.18)$$

where  $F_{\text{dev}}^0$  and  $F_{\text{dev}}^{\text{max}}$  represent the initial and maximum (saturation) values of the deviatoric fabric and  $\beta_F$  is its rate of change. To study the variation of the parameters  $s_{\text{dev}}^{\text{max}}$ ,  $\beta_s$ ,  $F_{\text{dev}}^0$  and  $F_{\text{dev}}^{\text{max}}$  with volume fraction  $v$  during deviatoric deformation, we perform several isochoric simulations at different volume fractions  $v_i$ , and obtain the coefficients as shown in Figs. 2.15 and 2.16 from fits to Eqs. (2.17) and (2.18).

As final step, but not shown in this paper, in order to relate the macroscopic anisotropy (modulus)  $A$  to the evolution of the deviatoric fabric  $F_{\text{dev}}$ , one can measure the elastic modulus  $A$  directly. For this the sample is deformed a little (either isotropically or purely deviatoric) at various different stages along the (large strain) deviatoric paths for D2 and D3 deformation modes. Details of the procedure and the results will be reported elsewhere [81]. Here, we only note that a linear relation is found such that:

$$A \approx a_0^* F_{\text{dev}} \frac{P v_c^2}{(v - v_c)} \approx \frac{a_0 k}{2 \langle r \rangle} F_v F_{\text{dev}}, \quad (2.19)$$

where  $a_0 = 0.137$  is a combination of numerical constants including  $g_3$ ,  $p_0$ .

Fitting the data of the volume conserving deviatoric simulations, in Figs. 2.11 and 2.13 through Eqs. (2.17) and (2.18), respectively, we get the dependence of  $s_{\text{dev}}^{\text{max}}$ ,  $\beta_s$ ,  $F_{\text{dev}}^{\text{max}}$  and  $\beta_F$  on volume fraction  $v$ . When the same equations are used to predict the evolution of deviatoric stress and fabric with strain (and volume fraction) for uniaxial deformation in subsection 2.6.2, perfect qualitative and satisfactory quantitative agreement is obtained (see Figs. 2.12 and 2.14).



### 2.7.2 Fitting of deviatoric deformations

For various deviatoric D2 and D3 simulations with different volume fraction, using Eq. (2.17), we obtain the variation of  $s_{\text{dev}}^{\text{max}}$  and  $\beta_s$  with  $v$ . As seen from Fig. 2.15(a), the factor  $s_{\text{dev}}^{\text{max}}$  decreases with increasing volume fraction  $v$  and in Fig. 2.15(b), where a similar decreasing trend for  $\beta_s$  with some larger scatter is seen. Both  $s_{\text{dev}}^{\text{max}}$  and  $\beta_s$  seem to saturate towards a finite limit for large volume fractions and these values can be extrapolated by the fitting procedure, described later in this section. The two parameters  $s_{\text{dev}}^{\text{max}}$  and  $\beta_s$ , as obtained from the different D2 and D3 deformation modes are very similar. This is not astonishing since the same net deviatoric strain applied in the two modes leads to the same net deviatoric stress ratio response.

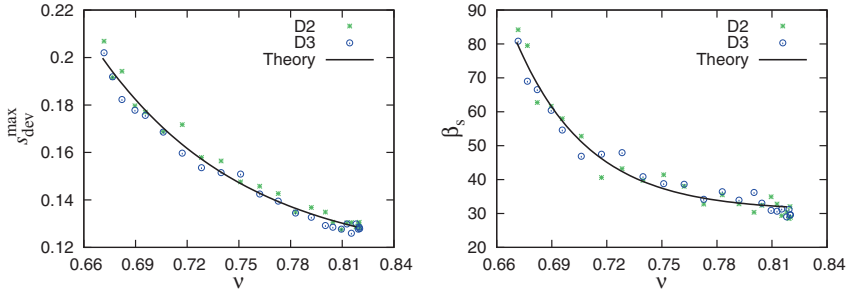


Figure 2.15: Comparison of evolution parameters from Eq. (2.17): the maximum normalized deviatoric stress  $s_{\text{dev}}^{\text{max}}$  and the growth rate  $\beta_s$ , plotted against volume fraction  $v$  for the D2 and D3 deviatoric modes. Each point represents a unique simulation; the green ‘\*’ represent the D2 mode while the blue ‘ $\odot$ ’ represent the D3 mode. The solid black line is the proposed analytical form in Eq. (2.20), with parameters given in Table 2.3.

Figure 2.16(a) shows the variation of  $F_{\text{dev}}^{\text{max}}$  with volume fraction for the same simulations as in Fig. 2.15, where the two deviatoric deformation modes D2 and D3 almost collapse on each other. The  $F_{\text{dev}}^{\text{max}}$  values decrease strongly with volume fraction  $v$  for the two modes. For higher volume fractions the motion of spheres is more constrained by more contacts and hence the anisotropy developed in the system is smaller. Figure 2.16(b) shows a similar decreasing behavior of  $\beta_F$  with volume fraction  $v$ , where stronger scatter is seen. In Fig. 2.16, the analytical fits of the normalized stress parameters ( $s_{\text{dev}}^{\text{max}}$  and  $\beta_A$ ) are also shown for comparison. A different behaviour between the normalized stress and the deviatoric fabric with respect to both parameters (maximum saturation value and the evolution rate), proves that stress and fabric evolve independently with deviatoric strain [85], as is the basic postulate for the anisotropic constitutive model.

We propose a generalized analytical relation for both the stress parameters  $s_{\text{dev}}^{\text{max}}$ ,  $\beta_s$  and the fabric parameters  $F_{\text{dev}}^{\text{max}}$ ,  $\beta_F$ , obtained from various different volume conserving deviatoric

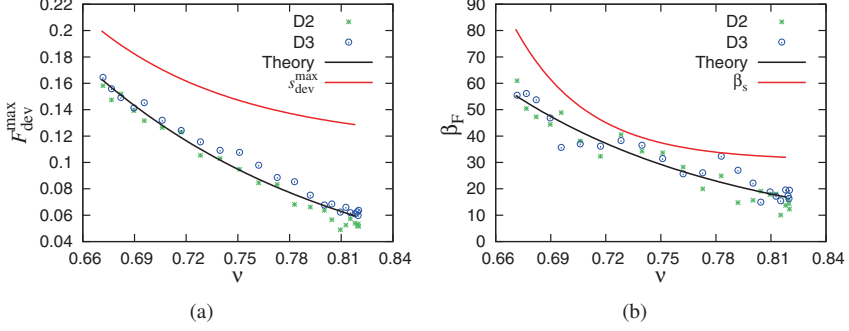


Figure 2.16: Comparison of evolution parameters from Eq. (2.18): the maximum anisotropy  $F_{\text{dev}}^{\text{max}}$  and the growth rate  $\beta_F$  plotted against volume fraction  $v$  for the D2 and D3 deviatoric modes. The solid black line is the proposed theory, Eq. (2.20), for  $F_{\text{dev}}^{\text{max}}$  and  $\beta_F$  respectively, while the red lines are the corresponding parameters  $s_{\text{dev}}^{\text{max}}$  and  $\beta_s$  from Eq. (2.17), in Fig. 2.15.

Evolution parameters	$Q_a$	$Q_c$	$\alpha$
$s_{\text{dev}}^{\text{max}}$	0.1137	0.09166	7.916
$\beta_s$	30.76	57.00	16.86
$F_{\text{dev}}^{\text{max}}$	0	0.1694	4.562
$\beta_F$	0	57.89	5.366

Table 2.3: Fitting coefficients for the parameters in Eqs. (2.17) and (2.18) with  $v_c = 0.6653$

D2/D3 deformation simulations. The dependence of the parameters on volume fraction  $v$ , is well described by the general relation:

$$Q = Q_{\text{max}} + Q_v e^{-\alpha \left( \frac{v}{v_c} - 1 \right)}, \quad (2.20)$$

where  $Q_{\text{max}}$ ,  $Q_v$  and  $\alpha$  are the fitting parameters with values presented in Table 2.3,  $v$  is the volume fraction and  $v_c \approx 0.6653$  is chosen as the jamming volume fraction, see Table 2.2. For all four parameters, the  $Q_{\text{max}}$  values are the limit for large volume fractions, while  $Q_c = Q_{\text{max}} + Q_v$  represents the limit at  $v \rightarrow v_c$ , and  $\alpha$  is the rate of variation (decay) with the volume fraction increasing above  $v_c$ . We assume, as consistent with the data, that the structural anisotropy parameters  $F_{\text{dev}}^{\text{max}}$  and  $\beta_F$  tend to 0 as the volume fraction increases, therefore keeping  $Q_{\text{max}} = 0$  in the fitting function for the deviatoric fabric coefficients. Eq. (2.20) represents the solid black lines shown in Figs. 2.15 and 2.16, with coefficients given in Table 2.3.

### 2.7.3 Prediction of uniaxial deformation

We use the parameters determined from the deviatoric simulations presented in Table 2.3, to predict the behaviour of uniaxial simulations, where the volume fraction is changing with deviatoric strain and hence dependence on  $v$  is needed to properly describe the deformation path.

Figure 2.12 shows the normalized deviatoric stress  $s_{\text{dev}}$  against deviatoric strain  $\epsilon_{\text{dev}}$  for uniaxial deformations starting from three different volume fractions ( $v = 0.671, 0.695$  and  $0.728$ ), and compared with the predictions of Eqs. (2.17) with coefficients  $s_{\text{dev}}^{\text{max}}(v)$  and  $\beta_s(v)$  taken from Table 2.2. The proposed model, although in its simplified version, is able to properly capture the behavior of the material qualitatively, approaching exponentially a maximum value and then decreasing due to the volume fraction dependence of the parameters. Note that the softening present in some of the deviatoric DEM data, is on purpose not plugged into the model as a constraint. This renders the softening present in the uniaxial deformation data as a valuable prediction of the model. Furthermore, the convergence of  $s_{\text{dev}}$  for uniaxial loading simulations with different initial volume fraction at large strains, as discussed in section 2.6.2, is also well captured by the theoretical model with calibrated parameters from the deviatoric simulations, where this does not happen.

Figure 2.14 shows the evolution of deviatoric fabric,  $F_{\text{dev}}$ , with deviatoric strain,  $\epsilon_{\text{dev}}$ , for uniaxial deformations – as above – together with the predictions of Eqs. (2.18) and (2.20). The model is still able to qualitatively describe the behavior of the deviatoric fabric, but with order of 30% over-prediction. The complete coupled model needs to be used and possibly improved, as will be presented elsewhere [79].

## 2.8 Conclusions and Outlook

The discrete element method has been used to investigate the bulk response of polydisperse, linear, frictionless sphere packings in 3D to various deformation modes in terms of both their micro- and macroscopic response. Main goal was to present a procedure to calibrate a constitutive model with the DEM data and then use the same to predict another simulation (mode). The (overly) simple material (model) allows to focus on the collective/bulk response of the material to *different* types of strain, excluding complex effects due to normal or tangential non-linearities. Therefore, the present study has to be seen as a reference “lower-limit” and the procedure rather than the material is the main subject.

We focused on strain-controlled loading and unloading of isotropic, uniaxial and two deviatoric (pure shear) type deformation modes (D2 and D3). Experimentally most difficult to realize is isotropic deformation, while both uniaxial and deviatoric modes can be realized in

various element tests where, however, often mixed strain- and stress-control is applied. Both micro-mechanical and coarse grained macroscopic properties of the assemblies are discussed and related to each other. The study covers a very wide range of isotropic, uniaxial and deviatoric deformation amplitudes and thus practically all densities with mechanically stable packings – except for those very close to the jamming volume fraction and higher than about 10% contact deformation, above which DEM pair contact models are questionable.

### 2.8.1 Microscopic quantities

The microscopic coordination number  $C$ , defined as the ratio of the total number of contacts to the total number of particles, has been analyzed as function of volume fraction and deviatoric strain. By disregarding particles with less than four contacts (called rattlers), the corrected coordination number  $C^*$  is well described by Eq. (2.11) for all deformation modes (since the particles are frictionless). For the uniform size-distribution used here, the fraction of rattlers shows an exponentially decaying trend towards higher densities, very similar for all modes, see Eq. (2.12), and Table 2.2. These analytical relations provide *a prediction for the coordination number*  $C = (1 - \phi_r) C^*$  that, notably, shows up in the macroscopic relations for both pressure and isotropic fabric, in combination with  $v$ , instead of  $C^*$ . (Note that  $C^*$  is better accessible to theory, while  $vC$  is related to the wave-propagation speed, which is experimentally accessible, while both are linked by the fraction of rattlers, which was already identified as a control parameter of utmost importance [25].)

A small but systematic difference in the  $C^*$  and  $\phi_r$  parameters appears for the different deformation modes. Most important, *the jamming volume fraction  $v_c$  is not a single, particular volume fraction*, but we observe a range of jamming densities dependent on the deformation modes, i.e., the “history” of the sample. Over-compression leads to an increase of  $v_c$ , i.e., to a better, more efficient packing. Subsequent deviatoric (pure shear) deformations slightly reduce the jamming volume fraction of such a previously over-compressed packing, causing it to become less efficiently packed. Note that more/less efficient packing is reflected by a large/small jamming volume fraction and, inversely, small/large coordination numbers. The effects described are more pronounced as the volume fraction becomes lower. For example, a slight increase in the fraction of rattlers due to deviatoric deformations is also reported, as consistent with the decrease in coordination number. Deviatoric modes (shear) can create more rattlers, while isotropic modes (compression) reduce the fraction of rattlers.

### 2.8.2 Macroscopic quantities

When focusing on macroscopic quantities, an important result from this study is that at small strains, the uniaxial, deviatoric and isotropic modes can be described by the same

analytical pressure evolution Eq. (2.15), with parameters given in Table 2.2, evidenced by the collapse of the data from these deformation modes on each other when the scaled pressure is plotted as a linear function of the volumetric strain. This linearity is due to the scaling with the non-linear terms,  $p^* \propto p/(vC)$  in particular. Thanks to the linear contact model used allows to conclude that the non-linear (quadratic) corrections are due to the structural rearrangements and non-affine deformations. A deviation of the scaled deviatoric and uniaxial from isotropic pressure data appears at larger strains, due to the build up of anisotropy in the system caused by deviatoric strain, obviously not present in the isotropic deformation mode. The good match of the data suggests an advantage of the “cheaper” uniaxial (and deviatoric) deformation modes over the experimentally difficult to realize isotropic deformation mode. (Three walls have to be moved simultaneously in the isotropic case, while a less complicated set-up is required for the other modes.)

The evolution of the deviatoric stress ratio (the deviatoric stress scaled with the isotropic pressure) as a function of the deviatoric strain is developing almost independently of the volume conserving deformation modes, when the deviatoric magnitude is defined in a similar fashion to the second deviatoric invariant [159], for all quantities studied. The deviatoric stress builds up with increasing deviatoric strain until a steady state is reached (where we do not focus on peak- and softening-behavior in this study, which is becoming more pronounced closer to the jamming volume fraction). Starting from isotropic initial configurations, we also show that the slope ( $G^{\text{oct}}/P$ ) of the normalized deviatoric stress as function of deviatoric strain decreases with increasing volume fraction, unlike the shear modulus  $G^{\text{oct}}$ , which increases with volume fraction. This indicates, that the pressure (and bulk modulus  $B$ ) are dependent on volume fraction “stronger” than the shear modulus.

From the macroscopic data, one observes that deviatoric and isotropic stresses and strains are cross-coupled by the structural anisotropy. The latter is quantified by the deviatoric fabric, which is proportional to the bulk-anisotropy modulus/moduli  $A$ , as relevant for the constitutive model. Cross-coupling means that – in the presence of structural anisotropy – isotropic strain can cause deviatoric stress responses and deviatoric strain can cause isotropic stress responses (dilatancy or compactancy). The structural anisotropy behaves very similar to the deviatoric stress ratio with deviatoric strain, but has different response rates as the latter. The response rates of the anisotropy of both stress and structure with deviatoric strain are functions of density and, most important, different from each other.

### 2.8.3 Constitutive model calibration

As first step, the parameters of the simplest constitutive model that involves anisotropy, as proposed in Refs. [98, 101] for 2D, have been extracted from DEM data for calibration. From the isotropic deformation mode, one can extract the bulk-modulus  $B$ , as done in Ref. [51]. From the volume conserving D2 and D3 modes, by fitting the idealized evolution equations

for shear stress in Eq. (2.17), the macroscopic friction,  $s_{\text{dev}}^{\text{max}}$ , and the deviatoric stress rate  $\beta_s$  can be inferred as functions of the volume fraction, entering the shear modulus  $G^{\text{oct}}$ . Similarly, the fit of Eq. (2.18) provides a relation for the maximum structural anisotropy at steady state,  $F_{\text{dev}}^{\text{max}}$ , and the fabric rate  $\beta_F$ , as functions of volume fraction. A relation between the deviatoric fabric and the anisotropy modulus/moduli  $A$ , in the model is finally needed to close the system and allow to integrate the coupled evolution equations for stress and structure.

As second step, and major result, the constitutive model calibrated on deviatoric data was used to predict qualitatively (and to some extent also quantitatively) both the stress and fabric evolution under uni-axial deformation. This is very promising, since the basic qualitative features are caught by the model, even though it was used in a very idealized and short form, with only main new ingredient the single anisotropy modulus  $A \propto F_{\text{dev}}$ . Several additional terms of assumed lesser magnitude are ignored and have to be added to complete the model, see Refs. [81, 101, 151, 159] and references therein, as postponed to future studies. (For example, an objective tensorial description of stress, strain and fabric, involves also the third tensor invariants. Alternatively/equivalently, these deviatoric tensors can be completely classified by their shape factors in their respective eigen-systems, which allows to distinguish all possible deformation and response modes in 3D.)

In this paper, we have reviewed and presented new results for frictionless particles undergoing isotropic, uniaxial, and (pure) shear deformation. Since the particles are too idealized, they provide insufficient freedom for direct application to practical systems, where shape, friction, and other non-linearities are relevant. However, they form the basic reference study with details given on the calibration procedure that yields a constitutive model with satisfactory predictive quality. Therefore, the next steps in our research will involve more realistic contact models with friction, cohesion, and other physically meaningful material parameters. Only then, the validity of the analytical expressions, which predict well the phenomenology, and the observations for pressure as well as the scaling arguments presented for the deviatoric stress and fabric, can be tested for realistic frictional, cohesive systems.

#### 2.8.4 Outlook

Laboratory element test experiments should also be performed with the bi-axial box to validate the simulation results with realistic material properties. Macroscopic quantities that can be readily obtained experimentally – for example the pressure-volume fraction relation and the shear stress evolution with deviatoric (shear) strain – can then be compared with simulation data. Moreover, the work underlines the predictive power of constitutive models with anisotropy, see Refs. [98, 101, 151], that can be further tested, validated and extended with more advanced physical and numerical experiments.

Given the detailed insights from DEM, the (missing) terms and the parameters for the constitutive models can now be further analyzed to perform the rigorous micro-macro transition. Open questions concern, among others:

- (i) the validity of the 2D model in 3D, related to missing terms and parameters,
- (ii) the validity of global versus local coarse-graining, i.e., the scale of the micro-macro transition [77],
- (iii) the microscopic (restructuring) and macroscopic (non-affine motions) origins of the peak- and softening phenomenology at the lower densities, related to the (in-)homogeneity of the packings,
- (iv) the validity of the model predictions for strain-reversal and cyclic deformations, and
- (v) the possible dependence of the moduli in the constitutive relations on other quantities (e.g., pressure) than the volume fraction, as focused on in this study.

For future application, the present calibration procedure should be checked also for other materials and applied to other element tests, among which there are (cylindrical) tri-axial tests, ring-shear tests and also avalanche flow experiments like in a rotating drum, all of which are more widely available than the “academic” bi-axial box. At the end the material properties and parameters should *not* depend on the element test chosen and the predictive value of the model(s) should be proven for more than only one validation test, be it another element test or a real-size or lab-scale process like, e.g., granular flow in a silo or during a landslide.

## Acknowledgement

Helpful discussions with M. B. Wojtkowski, F. Göncü, J. Ooi and M. Ramaioli are gratefully acknowledged. This work is financially supported by the European Union funded Marie Curie Initial Training Network, FP7 (ITN-238577), see <http://www.pardem.eu/> for more information.

## Chapter 3

# Effect of particle friction under uniaxial loading and unloading\*

### Abstract

*The influence of contact friction on the behavior of dense, polydisperse granular assemblies under uniaxial (oedometric) loading and unloading deformation is studied using discrete element simulations. Even though the uniaxial deformation protocol is one of the “simplest” element tests possible, the evolution of the structural anisotropy necessitates its careful analysis and understanding, since it is the source of interesting and unexpected observations.*

*On the macroscopic, homogenized, continuum scale, the deviatoric stress ratio and the deviatoric fabric behave in a different fashion during uniaxial loading and unloading. The maximal stress ratio and strain increase with increasing contact friction. In contrast, the deviatoric fabric reaches its maximum at a unique strain level independent of friction. For unloading, the reversal of stress displays a friction-dependent delay, while the reversal of fabric is found to occur also with delay, but slightly earlier.*

*On the micro-level, a friction-dependent non-symmetry of the proportion of weak/strong and sliding/sticking contacts with respect to the total contacts during loading and unloading is observed. Coupled to this, from the directional probability distribution, the*

---

\*Based on O. I. Imole, M. B. Wojtkowski, V. Magnanimo, and S. Luding. Micro-Macro Correlations and Anisotropy in Granular Assemblies under Uniaxial Loading and Unloading. *Phys. Rev. E (Under Review)*, 2013



*“memory” and history-dependent behavior of granular systems is confirmed. Surprisingly, while a rank-2 tensor is sufficient to describe the evolution of the normal force directions, a sixth order harmonic approximation is necessary to describe the contact probability distribution, the tangential force and the mobilized friction.*

*We conclude that the simple uniaxial deformation activates microscopic phenomena not only in the active Cartesian directions, but also at intermediate orientations, with the tilt angle being dependent on friction, so that the microstructure and forces cause the interesting macroscopic behavior.*

### 3.1 Introduction and Background

Granular materials are omnipresent in nature and widely used in various industries ranging from food, pharmaceutical, agriculture and mining – among others. In many granular systems, interesting phenomena like dilatancy, anisotropy, shear-band localization, history-dependence, jamming and yield have attracted significant scientific interest over the past decade [10, 62, 92]. The bulk behavior of these materials depends on the behavior of their constituents (particles) interacting through contact forces. To understand their deformation behavior, various laboratory element tests can be performed [111, 140]. Element tests are (ideally homogeneous) macroscopic tests in which one can control the stress and/or strain path. Such macroscopic experiments are important ingredients in developing and calibrating constitutive relations, but they provide little information on the microscopic origin of the bulk flow behavior. An alternative is the Discrete Element Method (DEM) [92], since it provides information about the micro-structure beyond what is experimentally accessible.

One element test which can easily be realized (experimentally or numerically) is the uniaxial (or oedometric) compression (in a cylindrical or box geometry) involving an axial deformation of a bulk sample while the lateral boundaries of the system are fixed. This test is particularly suited for determining the poroelastic properties of granular materials. During uniaxial loading, isotropic compression and non-isotropic deformation (pure shear) are superposed, so that pressure and shear stress build up. After reversal, pressure and shear stress decay and the latter changes sign after a finite strain, which depends on friction. When a granular material is sheared, along with the shear stress, also anisotropy of the contact network begins to develop.

It is known that besides density and stress, geometric anisotropy (contact fabric) is an important ingredient to fully understand the micro-macro-mechanics of granular materials. In addition, the effects of contact friction between the constituent grains influences the micromechanical response under uniaxial loading, such that a rather simple element test begins to reveal interesting features. Several studies have numerically investigated the extent to

which the response of granular media is affected by friction [12, 14, 15, 38, 145], especially in the triaxial geometry but not many studies exist on uniaxial loading and unloading of frictional systems [21].

Also, the transmission of stress between grain contacts is relevant, as detailed in this study. Experimental visualizations of the distribution of forces using photo-elastic particles in 2D is about the only way to access this information – see [104, 180] and references therein – even though 3D photoelasticity and other neutron diffraction methods [173] have also been employed. Earlier numerical studies have highlighted the particular character of the contact force network, showing that strong contacts carrying force larger than the average, are oriented anisotropically, with preferred direction parallel to the axis of compression, while those originating from weak contacts are isotropic or have a weak orientation orthogonal to the compression axis [125]. Another interesting issue is the distribution and orientation of tangential forces during the deformation of dense frictional packings [124, 150, 158]. In early, two-dimensional studies on frictional avalanching [124], it has been observed that friction is mobilized mostly from weak contacts, whereas strong contacts resist friction mobilization.

It is important at this point to distinguish between the three-dimensional uniaxial element test and the triaxial test. In the standard triaxial test, stress is imposed on test sample in the axial (vertical) direction ( $\sigma_1$ ) while the stress in the lateral (horizontal) directions ( $\sigma_2$  and  $\sigma_3$ ) are kept constant (i.e.  $\sigma_1 \neq \sigma_2 = \sigma_3$ ). As with the uniaxial test, the stress in the axial direction is typically higher than the two lateral stresses during loading. A striking difference between both tests is in the lateral direction where stress is kept constant in the triaxial test ( $\sigma_2 = \sigma_3 = \sigma_0$ ) but different in the uniaxial test ( $\sigma_2 \approx \sigma_3 > \sigma_0$ ), increasing from its initial value  $\sigma_0$ , since the walls are fixed. It is also worth mentioning that the triaxial test is mostly used in geotechnical applications such as the testing of sands and rocks at very high stress levels. Since the broader focus of our research is the testing of frictional and cohesive granular materials for applications in the food, chemical and agricultural industries, we focus on the much simpler confined uniaxial compression test and juxtapose our findings with those obtained in the triaxial test.

In the present study, we use discrete element simulations of confined uniaxial compression tests to investigate and relate the dependencies between the microscopic observations presented hereafter with the evolution of macroscopic quantities such as pressure and deviatoric stress – and to further extend this to explain the evolution of the structural/contact and force/stress anisotropies.

This work is structured as follows. We first describe the simulation method and model parameters along with the preparation and test procedures in 3.2. The definitions of averaged micro-macro quantities including strain, stress and structural anisotropies are presented in 3.3. Where given, anisotropy refers to not only the deviatoric stress, but also to

the direction-dependence and inhomogeneity of forces, i.e., its microscopic origin. Next, we discuss the results of the current study by presenting the evolution of the stress and structural anisotropies during uniaxial loading and unloading in 3.4.2 followed by the magnitude and orientation of their respective eigenvalues in 3.4.3. Furthermore, we discuss friction mobilization in Section 3.4.4 followed by the probability density functions of the normal and tangential forces in 3.4.5 and the classification of weak and strong forces in 3.4.5. In Section 3.5, we discuss the polar representation of the contact distribution based on the constant surface and constant bin width method and extract the structural anisotropy parameters using a 6th order Legendre spherical harmonic approximation in section 3.5.1. Finally, the summary, conclusions and outlook are presented in Section 3.6.

## 3.2 Simulation details

We use the Discrete Element Method (DEM) [92] with a simple linear visco-elastic normal contact force law  $f^n \hat{\mathbf{n}} = (k\delta + \gamma\dot{\delta})\hat{\mathbf{n}}$ , where  $k$  is the spring stiffness,  $\gamma_n$  is the contact viscosity parameter and  $\delta$  or  $\dot{\delta}$  are the overlap or the relative velocity in the normal direction  $\hat{\mathbf{n}}$ . The normal force is complemented by a tangential force law [92], such that the total force at contact  $c$  is:  $\mathbf{f}_c = f_n \hat{\mathbf{n}} + f_t \hat{\mathbf{t}}$ , where  $\hat{\mathbf{n}} \cdot \hat{\mathbf{t}} = 0$ , with tangential force unit vector  $\hat{\mathbf{t}}$ . A summary of the values of the parameters used is shown in Table 3.1, with sliding and sticking friction  $\mu = \mu_{sl} = \mu_{st}$  and rolling- and torsion-torques inactive ( $\mu_r = \mu_t = 0$ ). An artificial viscous dissipation force proportional to the velocity of the particle is added for both translational and rotational degrees of freedom, resembling the damping due to a background medium, as e.g. a fluid.

### 3.2.1 Simulation set-up and boundary conditions

The simulation set-up is a cuboid volume [60], triaxial box, with periodic boundaries on all sides. Since careful, well-defined sample preparation is essential, to obtain reproducible results [40], we follow a three-step procedure where friction is active in all the preparation stages:

- (i) Spherical particles are randomly generated in the 3D box with low volume fraction and rather large random velocities, such that they have sufficient space and time to exchange places and to randomize themselves.
- (ii) This granular gas is then isotropically compressed to a target volume fraction  $v_0$  slightly below the jamming volume fraction.
- (iii) This is followed by a relaxation period at constant volume fraction to allow the parti-

	Value	Unit	Description
$N$	9261	[-]	Number of particles
$\langle r \rangle$	1	[mm]	Average radius
$w$	1.5	[-]	Polydispersity $w = r_{\max}/r_{\min}$
$\rho$	2000	[kg/m <sup>3</sup> ]	Particle density
$k_n$	$10^5$	[kg/s <sup>2</sup> ]	Normal spring stiffness
$k_t$	$2 \cdot 10^4$	[kg/s <sup>2</sup> ]	Tangential spring stiffness
$\mu$	vary	[-]	Coefficient of friction
$\gamma_n$	1000	[kg/s]	Viscosity – normal direction
$\gamma_t$	200	[kg/s]	Viscosity – tangential direction
$\gamma_{bt}$	100	[kg/s]	Background damping – translational
$\gamma_{br}$	20	[kg/s]	Background damping – rotational
$t_c$	0.64	[ $\mu$ s]	Contact duration (average)

Table 3.1: Summary and numerical values of particle parameters used in the DEM simulations, where  $\mu$ , the contact coefficient of friction is varied in the following. For more details, see Ref. [92].

cles to dissipate their kinetic energy before further preparation or the actual element test is initiated.

### 3.2.2 Isotropic Compression Methods

After the three-step preparation, an isotropic compression test can be initiated to measure isotropic properties and to prepare further initial configurations at different volume fractions, with subsequent relaxation, so that we have a series of different reference isotropic configurations, achieved during loading and unloading, as displayed in Fig. 3.1. The goal here is to approach a direction independent isotropic configuration above the jamming volume fraction  $v_c$ , i.e. the transition point from fluid-like behavior to solid-like behavior [164]. Note that the initial packings for the respective frictional configurations are inherently different since they are prepared with the different friction coefficients active from the beginning of the first isotropic preparation stage (stage A in Fig. 3.1). We only keep as control parameter the volume fraction which is identical for the different configurations even though other micro-macro quantities such as pressure and coordination number will be different at a given volume fraction.

In the current study, to obtain a homogeneous initial isotropic configuration, several driving modes have been compared and these modes are discussed briefly in the following section.

Later, for uniaxial tests, unless explicitly mentioned, the wall-driven uniaxial deformation protocol is applied. We tested the wall-driven against the strain-rate driven protocols for some quantities of interest to this work and realize that they lead to mostly the same results – besides some small details (see Sec. 3.2.2). Note that particular attention must be placed on the choice of the preparation protocol when other boundary conditions or quantities are considered as this conclusion may no longer hold. Even though strain-rate driven produces more homogeneous systems, we use the wall-driven mode since it more resembles the real experiment therefore important for future experimental validation of this work [29].

### Wall-driven isotropic compression

In the first method, the periodic walls of the box are subjected to a strain-controlled motion following a co-sinusoidal law such that the position of e.g., the top wall as function of time  $t$  is

$$z(t) = z_f + \frac{z_0 - z_f}{2}(1 + \cos 2\pi ft) \quad (3.1)$$

with engineering strain

$$\epsilon_{zz}(t) = 1 - \frac{z(t)}{z_0}, \quad (3.2)$$

where  $z_0$  is the initial box length and  $z_f$  is the box length at maximum strain, respectively, and  $f = T^{-1}$  is the frequency. The maximum deformation is reached after half a period  $t = T/2$ , and the maximum strain-rate applied during the deformation is  $\dot{\epsilon}_{zz}^{\max} = 2\pi f(z_0 - z_f)/(2z_0) = \pi f(z_0 - z_f)/z_0$ . The co-sinusoidal law allows for a smooth start-up and finish of the motion so that shocks and inertia effects are reduced. Also, the walls were driven in a quasi-static manner such that the ratio of the kinetic and potential energy ( $E_k/E_p \leq 10^{-5}$ ). By performing slower deformations, the energy ratio can be reduced even further [60].

### Pressure controlled isotropic deformation

In the pressure controlled mode, the (virtual) periodic walls of the system are subjected to a co-sinusoidal periodic pressure-control until the target pressure is achieved, for details see [88]. To achieve this, we set the mass of the virtual periodic walls of the system  $m_w$ , to be of the order of the total mass of the particles in the system, leading to consistent behavior. The pressure controlled motion of the walls is described by [88]:

$$m_w \ddot{x}_w(t) = F_x(t) - pA_x(t) - \gamma_w \dot{x}(t), \quad (3.3)$$

where  $F_x(t)$  is the force due to the bulk material,  $pA_x(t)$  is the force related to the external load and the last term is a viscous force, which damps the motion of the wall so that oscillations are reduced.  $A_x$  is the area of the wall perpendicular to  $x$  where  $x$  can be replaced by  $y$  or  $z$  in Eq. 3.3, for other walls. We find that large values of  $m_w$  generally lead to large energy fluctuations/oscillations while the final pressure is more rapidly approached for systems with smaller  $m_w$ . In contrast, too small  $m_w$  can lead to violent motions and should be avoided. Additionally, we must mention that for our simulations, the sensitivity of the system to the wall dissipation is small since the simulations are performed in the very slow, quasi-static regime.

### Homogeneous strain-rate controlled isotropic deformation

In this method, we apply a homogeneous strain rate to all particles in the ensemble and to the walls in each time-step, such that each particle experiences an affine simultaneous displacement according to the diagonal strain rate tensor:

$$\dot{\mathbf{E}} = \dot{\epsilon}_v \begin{pmatrix} -1 & 0 & 0 \\ 0 & -1 & 0 \\ 0 & 0 & -1 \end{pmatrix},$$

where  $\dot{\epsilon}_v (> 0)$  is the rate amplitude applied until a target maximum volume fraction of e.g.,  $v_{\max} = 0.82$  is achieved. A pictorial representation of the strain rate tensor is shown in Fig. 2.2. The DEM dynamics allows the particles to approach mechanical equilibrium by following the new unbalanced forces that lead to non-affine displacements due to the new forces at each time-step, or after a relaxation period.

### Swelling of Particles

An alternative isotropic deformation protocol is to allow the particle radii  $r$  to slowly ‘grow’ at rate  $g_r$  from an initial volume fraction according to the relation  $dr/dt = g_r r$ . The swelling of the particles leads to a change in the volume fraction until the target volume fraction is achieved [96, 116]. During the growth period, the particle mass changes with the radius. Additionally, the volume fraction also changes with time according to the relation  $dv/dt = 3vg_r$ , leading to the volume fraction  $v = v_0 \exp\{3g_r t\}$  as function of time  $t$ . The detailed form of the growth law with time is not relevant here, since all rates are very small.

### Comparison of driving modes

In summary, comparing the preparation methods, we find that isotropic quantities like pressure, coordination number or isotropic fabric evolve in a similar fashion for all driving modes. However, the strain-rate controlled isotropic preparation leads to very homogeneous configurations especially when viewed in terms of the mobilized friction. In the wall driven case, we find that friction is more highly mobilized in the contacts closest to the virtual periodic walls of the system leading to slight inhomogeneities. However, when the particles closest to the wall (up to  $\approx 30\%$  of the box length) are excluded from the computation, the resulting probability distributions as well as the field quantities show negligible differences with respect to the data from the full sample analysis. Due to this assessment, we choose here to focus on the wall driven isotropic compression since this more resembles experimental set-ups and is especially suitable for the subsequent uniaxial compression mode. Additionally, the cosinusoidal wall motion allows for a smooth start-up and end of the compression cycle unlike the “kick” (even though tiny) to each particle in the strain rate controlled protocol. To be confident with our conclusions, some data are checked by comparing them with simulations performed with the strain-rate protocol, without coming to different conclusions.

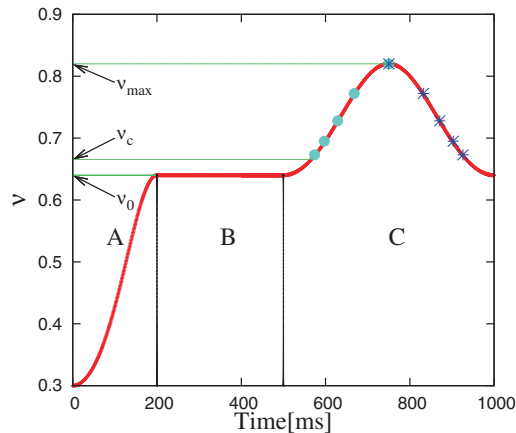


Figure 3.1: Evolution of volume fraction as a function of time. Region A represents the initial isotropic compression below the jamming volume fraction. B represents relaxation of the system to fully dissipate the systems potential and kinetic energy and C represents the subsequent isotropic compression up to  $v_{max} = 0.820$  and then subsequent decompression. Cyan dots represent some of the initial configurations, at different  $v_i$ , during the loading cycle; blue stars, for the same  $v_i$  are different configurations, since obtained during the unloading cycle; both can be chosen for further study.

### 3.2.3 Uniaxial Loading and Unloading

After isotropic compression, initial states can be chosen from the loading or unloading branch (after relaxation to allow for kinetic energy dissipation) from which the uniaxial test is initiated.

As element test, uniaxial compression is achieved by moving the periodic walls in the  $z$ -direction according to a prescribed co-sinusoidal strain path [60], as shown in Eq. (3.1), with diagonal strain-rate tensor

$$\dot{\mathbf{E}} = \dot{\epsilon}_u \begin{pmatrix} 0 & 0 & 0 \\ 0 & 0 & 0 \\ 0 & 0 & -1 \end{pmatrix},$$

where  $\dot{\epsilon}_u$  is the strain-rate (compression  $> 0$  and decompression/tension  $< 0$ ) amplitude applied in the uniaxial mode. The negative sign (convention) of  $\dot{E}_{zz}$  corresponds to a reduction of length, so that tensile deformation is positive. During loading (compression) the volume fraction increases from  $v_0$  (at dimensionless time  $\tau = t/T_{\max} = 0$ ) to a maximum  $v_{\max} = 0.820$  ( $\tau = 0.5$ ) and reverses back to the original  $v_0$  at the end of the cycle ( $\tau = 1$ ), after complete unloading. For more details on preparation and other parameters, see Ref. [60].

Even though the strain is imposed only on one mobile periodic “wall” with normal in the  $z$ -direction, which leads to an increase of compressive stress during compression, also the non-mobile  $x$  and  $y$  directions experience some stress increase as expected for “solid” materials with non-zero Poisson ratio, as discussed in more detail in the following sections.

However, during decompression the stress on the passive walls is typically smaller than that of the mobile, active wall, as consistent with anisotropic materials and findings from simulations and laboratory element tests using the bi-axial tester [82, 178] or the so-called lambdameter [83]. One of the main goals of this study is to also understand the behavior of the packing when compression is changed/reversed to tension.

## 3.3 Definitions of Averaged Quantities

In this section, we present the general definitions of averaged microscopic and macroscopic quantities.



### 3.3.1 General Tensor Formulation

To describe and better understand the relationships between macroscopic quantities, tensors are split up into isotropic, deviatoric and antisymmetric parts. For a general decomposition theorem, each tensor can be decomposed as:

$$\mathbf{T} = \frac{1}{2}(\mathbf{T} + \mathbf{T}^T) + \frac{1}{2}(\mathbf{T} - \mathbf{T}^T) = \mathbf{T}_{\text{sym}} + \mathbf{T}_{\text{skew}}, \quad (3.4)$$

where  $\mathbf{T}_{\text{sym}}$  and  $\mathbf{T}_{\text{skew}}$  are the symmetric and antisymmetric parts of the tensor. Since we will focus on the symmetric part, we further decompose  $\mathbf{T}_{\text{sym}}$  uniquely into its spherical and deviatoric parts as

$$\mathbf{T} = T_v \mathbf{I} + \mathbf{T}_D \quad (3.5)$$

with  $T_v = (1/3)\text{tr}(\mathbf{T})$  and the traceless deviator  $\mathbf{T}_D = \mathbf{T} - T_v \mathbf{I}$ . The latter contains information about the eigensystem of  $\mathbf{T}$ , that is identical to the eigensystem of  $\mathbf{T}_D$  itself.

Any (deviatoric) tensor can be transformed using a transformation matrix  $\mathbf{R}$  to obtain its diagonal form:

$$\mathbf{T}_D^{\text{eig}} = \begin{pmatrix} T_D^{(1)} & 0 & 0 \\ 0 & T_D^{(2)} & 0 \\ 0 & 0 & T_D^{(3)} \end{pmatrix} = \mathbf{R}^T \cdot \mathbf{T}_D \cdot \mathbf{R}, \quad (3.6)$$

$\mathbf{T}_D = T_i - T_v/3$ , where  $T_i$ 's are eigenvalues of  $\mathbf{T}$ . Also,  $T_D^{(1)}$ ,  $T_D^{(2)}$  and  $T_D^{(3)}$  are the eigenvalues sorted such that, as convention,  $T_D^{(1)} \geq T_D^{(2)} \geq T_D^{(3)}$ .  $\mathbf{R} = (\hat{\mathbf{n}}_1, \hat{\mathbf{n}}_2, \hat{\mathbf{n}}_3)$  is the orthogonal transformation matrix, composed of the corresponding eigenvectors, which transforms  $\mathbf{T}_D$  to its eigensystem. According to linear algebra, Eq. (3.6) can also be expressed as:

$$\mathbf{T}_D \cdot \hat{\mathbf{n}}_\alpha = T_D^\alpha \hat{\mathbf{n}}_\alpha \quad (3.7)$$

with  $T_D^\alpha$  and  $\hat{\mathbf{n}}_\alpha$  the  $\alpha$ -eigenvalue and eigenvector of  $\mathbf{T}_D$ , respectively. The symbol “ $\cdot$ ” represents the inner product of the tensor  $\mathbf{T}_D$  and the vector  $\hat{\mathbf{n}}_\alpha$  which leads to a vector parallel to  $\hat{\mathbf{n}}_\alpha$ .

In the following, we provide a consistent decomposition for strain, stress and fabric tensors. We choose here to describe each tensor in terms of its isotropic part (first invariant) and the second ( $J_2$ ) and third ( $J_3$ ) invariant of the deviator:

$$J_2 = \frac{1}{2} \left[ (T_D^{(1)})^2 + (T_D^{(2)})^2 + (T_D^{(3)})^2 \right] \quad (3.8)$$

$$J_3 = \det(\mathbf{T}_D) = T_D^{(1)} T_D^{(2)} T_D^{(3)} \quad (3.9)$$

$J_3$  can further be decomposed as  $J_3 = T_D^{(1)} T_D^{(2)} (-T_D^{(1)} - T_D^{(2)})$ , since we are dealing with deviators.

### 3.3.2 Strain

For any deformation, the isotropic part of the infinitesimal strain tensor  $\epsilon_v$  (in contrast to the true strain  $\epsilon_v$ ) is defined as:

$$\epsilon_v = \dot{\epsilon}_v dt = \frac{\epsilon_{xx} + \epsilon_{yy} + \epsilon_{zz}}{3} = \frac{1}{3} \text{tr}(\mathbf{E}) = \frac{1}{3} \text{tr}(\dot{\mathbf{E}}) dt, \quad (3.10)$$

where  $\epsilon_{\alpha\alpha} = \dot{\epsilon}_{\alpha\alpha} dt$  with  $\alpha\alpha = xx, yy$  and  $zz$  as the diagonal elements of the strain tensor  $\mathbf{E}$  in the Cartesian  $x, y, z$  reference system. The integral of  $3\epsilon_v$  denoted by  $\epsilon_v = 3 \int_{V_0}^V \epsilon_v$ , is the true or logarithmic strain, i.e., the volume change of the system, relative to the initial reference volume,  $V_0$  [51].

Several definitions are available in literature [159] to define the deviatoric magnitude of the strain. Here, we use the objective definition of the deviatoric strain in terms of its eigenvalues  $\epsilon_d^{(1)}$ ,  $\epsilon_d^{(2)}$  and  $\epsilon_d^{(3)}$  which is independent of the sign convention.

The deviatoric strain is defined as:

$$\epsilon_{\text{dev}} = \sqrt{\frac{\left(\epsilon_d^{(1)} - \epsilon_d^{(2)}\right)^2 + \left(\epsilon_d^{(2)} - \epsilon_d^{(3)}\right)^2 + \left(\epsilon_d^{(3)} - \epsilon_d^{(1)}\right)^2}{2}}, \quad (3.11)$$

where  $\epsilon_{\text{dev}} \geq 0$  is the magnitude of the deviatoric strain.

Note that the wall motion is strain controlled and the infinitesimal strain corresponds to the external applied strain. Hence the eigenvalues for the strain tensor are in the Cartesian coordinate system (thus no transformation is needed). For the purely isotropic strain,  $\epsilon^{\text{ISO}} = \epsilon_v \mathbf{I}$ , with  $\epsilon_{\text{dev}} = 0$ , which is direction independent by definition. The corresponding shape factor for the deviatoric strain  $\Lambda^{(-\epsilon)}$ , is represented as the ratio  $\Lambda^{(-\epsilon)} := \epsilon_d^{(2)} / \epsilon_d^{(1)}$ .

### 3.3.3 Stress

From the simulations, one can determine the stress tensor (compressive stress is positive as convention) components:

$$\sigma_{\alpha\beta} = \frac{1}{V} \left( \sum_{p \in V} m^p v_{\alpha}^p v_{\beta}^p - \sum_{c \in V} f_{\alpha}^c l_{\beta}^c \right), \quad (3.12)$$

with particle  $p$ , mass  $m^p$ , velocity  $v^p$ , contact  $c$ , force  $f^c$  and branch vector  $l^c$ , while Greek letters represent components  $x$ ,  $y$ , and  $z$  [60, 89]. The first sum is the kinetic energy density tensor while the second involves the contact-force dyadic product with the branch vector. Averaging, smoothing or coarse graining [170, 172] in the vicinity of the averaging volume,  $V$ , weighted according to the vicinity is not applied in this study, since averages are taken over the total volume. Furthermore, since the data in this study are quasi-static, the first sum can mostly be neglected. The isotropic stress is denoted as hydrostatic pressure:

$$p = \sigma_v = \frac{1}{3} \text{tr}(\boldsymbol{\sigma}) \quad (3.13)$$

As already mentioned, we will focus on the eigenvalues of the deviatoric stress tensor  $\lambda_i^s = \sigma_i^D = \sigma_i - p$ , as defined in section 3.3.1, with the principal directions being the same for  $\boldsymbol{\sigma}$  and  $\boldsymbol{\sigma}^D$ . The (scalar) deviatoric stress for our 3D uniaxial simulations is:

$$\sigma_{\text{dev}} = \sqrt{\frac{(\lambda_1^s - \lambda_2^s)^2 + (\lambda_1^s - \lambda_3^s)^2 + (\lambda_2^s - \lambda_3^s)^2}{2}}, \quad (3.14)$$

The deviatoric stress ratio,  $s_{\text{dev}} = \sigma_{\text{dev}}/p$ , quantifies the “stress anisotropy” - where  $\sigma_{\text{dev}} = \sqrt{3J_2^{\sigma}}$ , with  $J_2^{\sigma}$  the second invariant of the deviatoric stress tensor. The third stress invariant  $J_3^{\sigma} = \lambda_1^s \lambda_2^s \lambda_3^s = \lambda_1^s \lambda_2^s (-\lambda_1^s - \lambda_2^s) = (\lambda_1^s)^3 (-\Lambda^{\sigma} - (\Lambda^{\sigma})^2)$  can be replaced by the shape factor  $\Lambda^{\sigma} := \lambda_2^s/\lambda_1^s$ , which switches from +1 at maximum uniaxial loading to  $-1/2$  after some unloading as will be shown below.

### 3.3.4 Structural (Fabric) Anisotropy

Besides the stress of a static packing of powders and grains, an important microscopic quantity of interest is the fabric/structure tensor. For disordered media, the concept of a fabric tensor naturally occurs when the system consists of an elastic network or a packing of discrete particles. A possible expression for the components of the fabric tensor is provided in

[89, 99]:

$$F_{\alpha\beta}^v = \langle F^p \rangle = \frac{1}{V} \sum_{p \in V} V^p \sum_{c=1}^N n_{\alpha}^c n_{\beta}^c, \quad (3.15)$$

where  $V^p$  is the particle volume of particle  $p$  which lies inside the averaging volume  $V$ , and  $n^c$  is the normal vector pointing from the center of particle  $p$  to contact  $c$ .  $F_{\alpha\beta}^v$  are thus the components of a symmetric rank two  $3 \times 3$  tensor. In a large volume with some distribution of particle radii, the relationship between the trace of fabric, volume fraction  $v$  and the average coordination number  $C$  is given by  $3F_v^v := F_{\alpha\alpha}^v = g_3 v C$ , as first reported in [94] and also confirmed from our wider friction ( $\mu$ ) data. The term  $g_3$  corrects for the fact that the coordination number for different sized particles is proportional to their surface area such that for a monodisperse packing  $g_3 = 1$  and for a polydisperse packing  $g_3 > 1$  [51, 99, 141].

A different formulation for the fabric tensor considers simply the orientation of contacts normalized with the total number of contacts  $N_c$ , as follows [85, 114, 134]:

$$F_{\alpha\beta} = \frac{1}{N_c} \sum_{c=1}^N n_{\alpha}^c n_{\beta}^c, \quad (3.16)$$

The relationship between Eq. (3.15) and Eq. (3.16) is:

$$F_{\alpha\beta} = \frac{F_{\alpha\beta}^v}{g_3 v C} = \frac{3F_{\alpha\beta}^v}{F_v}. \quad (3.17)$$

We can define the deviatoric tensor  $\mathbf{F}^D$  and calculate the eigenvalues  $\lambda_i^f = F_i - F_v/3$  with  $F_v = 1$ , and  $F_i$  the eigenvalues of the deviatoric fabric based on Eq. (3.16).

We assume that the structural anisotropy in the system is quantified (completely) by the anisotropy of fabric, i.e., the deviatoric fabric, with scalar magnitude similar to Eqs. (3.11) and (3.14) as:

$$F_{\text{dev}} = \sqrt{\frac{(\lambda_1^f - \lambda_2^f)^2 + (\lambda_1^f - \lambda_3^f)^2 + (\lambda_2^f - \lambda_3^f)^2}{2}}, \quad (3.18)$$

proportional to the second invariant of  $\mathbf{F}^D$ ,  $F_{\text{dev}} = \sqrt{3J_2^F}$ , where  $\lambda_1^f$ ,  $\lambda_2^f$  and  $\lambda_3^f$  are the three eigenvalues of the deviatoric fabric tensor.

Alternatively, a simpler definition of the deviatoric fabric for an axial symmetric element

test takes into account the difference between the fabric eigenvalue of the main compressive (axial) direction and the average values in the isotropic plane as follows:

$$F_{\text{dev}}^* = \lambda_1^f - \frac{\lambda_2^f + \lambda_3^f}{2}. \quad (3.19)$$

Note that if  $\lambda_2^f = \lambda_3^f$ , Eqs. (3.18) and (3.19) coincide. Analogous to the definitions in Eqs. (3.18) and (3.19),  $F_{\text{dev}}$  and  $F_{\text{dev}}^*$  can also be defined using the definition of the fabric presented in Eq. (3.15).

### 3.3.5 Eigenvector Orientation

Due to the axial symmetry of the uniaxial compression mode, the orientation of the eigenvectors of stress and fabric can be defined with reference to the main compressive  $z$ -direction as:

$$\theta_\alpha = \arccos(\hat{\mathbf{n}}^{(\alpha)} \cdot \hat{\mathbf{z}}) \quad (3.20)$$

where  $\hat{\mathbf{z}}$  is the unit vector in the  $z$ -direction. Additionally, orientations are projected such that they lie within the range to  $\pi/2$ .

## 3.4 Results and Observations

In this section, as results of the current study, first we will discuss the influence of friction on the evolution of stress and structural anisotropy as functions of deviatoric strain during loading and unloading. To complement these results, we investigate the magnitude and orientation of the eigenvalues of stress and fabric during loading and unloading and their respective shape factors. To gain an insight into the relationship between the normal and tangential force on the macroscopic stress and structure, we report briefly their probability density functions (pdfs) for different frictional systems, as well as the force intensity weighted by the contact state. Finally, we present a 6th order harmonic approximation of the polar representation of contacts and forces to describe the axial-symmetric structural anisotropy, relating fabric to the pdfs.

### 3.4.1 Pressure and Coordination Number

Isotropic quantities during loading and unloading for various deformation paths were presented in Ref. [60] for frictionless particles and in Ref. [52] for frictional particles and will

not be discussed in detail here. We only note that the coordination number and the hydrostatic pressure scale quantitatively differently with isotropic strain but behave in a very similar fashion irrespective of the deformation mode applied. The pressure is coupled to the deviatoric strain via the structural anisotropy. The effects of polydispersity on the evolution of the isotropic quantities have also been extensively studied in Ref. [79] for various deformation paths. The isotropic quantities, namely pressure, coordination number and fraction of rattlers show a systematic dependence on the deformation mode and polydispersity via the respective jamming volume fractions.

In Figs. 3.2a and 3.2b, we plot the non-dimensional pressure  $p$  for different friction coefficients  $\mu = 0$  to 1 during loading and unloading, respectively. Here we define the non-dimensional pressure as

$$p = \frac{2\langle r \rangle}{3k_n} \text{tr}(\boldsymbol{\sigma}) \quad (3.21)$$

where  $\text{tr}(\boldsymbol{\sigma})$  is the trace of the stress tensor. The uniaxial test starts from an initial volume fraction  $v_i = 0.692$  above the jamming volume fraction and reaches a maximum volume fraction  $v_{\text{max}} = 0.82$  during loading before returning to  $v_i$ . The loading and unloading branches are close with the unloading branch having a tiny shift to the right due to hysteretic effects [51]. We observe that even though the different initial configurations are identical with respect to the initial volume fraction, their initial pressure states are different since their friction coefficients are activated right from the initial preparation stage (as in material being filled into a constant volume sample-holder). We also note that  $p$  increases with increasing  $v$  during uniaxial loading for all friction coefficients. For any given volume fraction, we observe an increase in  $p$  with increasing  $\mu$  as indicated by the direction of the arrow.

Extrapolating the pressure data to  $p \rightarrow 0$  leads to the respective jamming densities  $v_c(\mu)$ , which decreases with  $\mu$  increasing [52], which is the main reason for the observed behavior.

Furthermore, in Figs. 3.2c and 3.2d, we plot the evolution of the coordination number  $C^*$  as function of the volume fraction  $v$  and show its dependence on friction during loading and unloading, respectively. The coordination number here is defined as the average number of contacts per particle in the ensemble. Here, we exclude the particles with less than four contacts (called rattlers) since they do not contribute to the mechanical stability of the packing [51, 60, 79]. During loading, we observe an increase in the coordination number followed by a decrease after strain reversal. We observe a systematic decrease in the coordination number with friction with the largest friction showing the smallest coordination number. This indicates that fewer contacts are necessary for stability with increasing friction, even though  $p$  is larger.

In the following sections, we will focus on the non-isotropic quantities and their evolution with respect to the deviatoric strain.

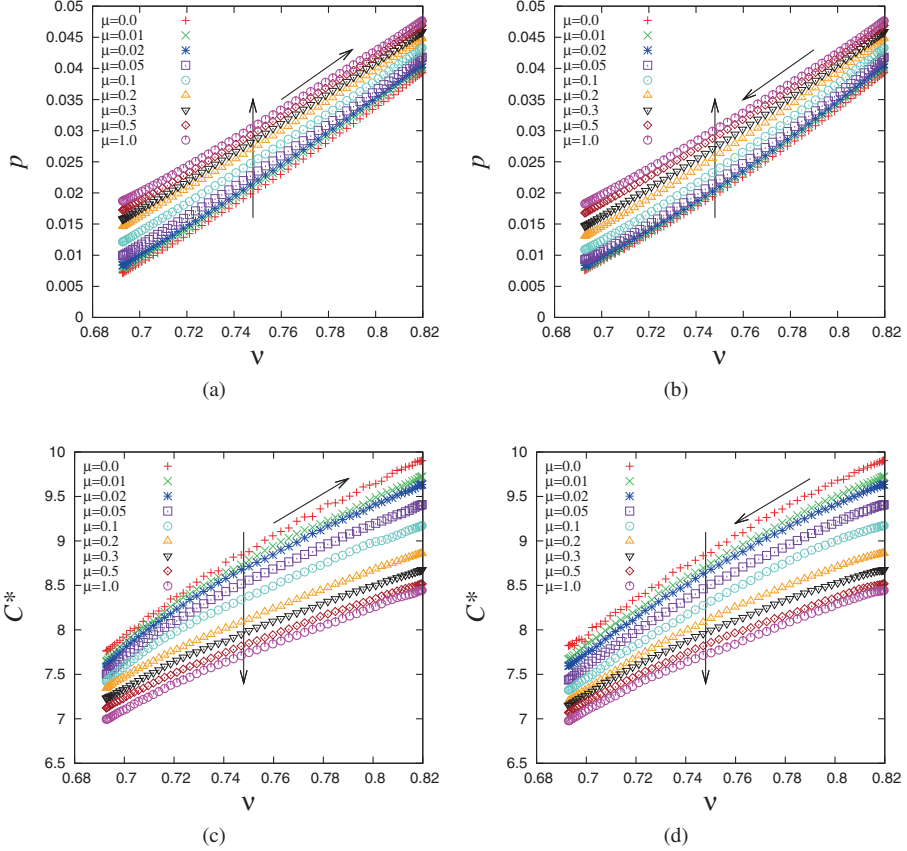


Figure 3.2: The non-dimensional pressure plotted as function of volume fraction under uniaxial deformation for different friction coefficients during (a) loading and (b) unloading and coordination number (excluding rattlers) for the same dataset during (a) loading and (b) unloading.

### 3.4.2 Deviatoric Stress and Fabric

Under uniaxial compression, not only does shear stress build up, but also the anisotropy of the contact and force networks develops, as it relates to the creation and destruction of new contacts [60]. We term the deviatoric part of the stress tensor and its microscopic force-direction dependence as the “stress anisotropy”, in parallel to the contact direction-dependency of the structural anisotropy.

The deviatoric stress ratio,  $s_{\text{dev}} = \sigma_{\text{dev}}/p$  is shown in Figs. 3.3a and 3.3b for a frictionless ( $\mu = 0$ ) and several frictional ( $\mu = 0.01, 0.02, 0.05, 0.1, 0.2, 0.3, 0.5$  and  $1.0$ ) systems during

uniaxial loading and unloading, respectively. As the deviatoric strain applied to the system is increased during uniaxial loading, the deviatoric stress ratio initially grows for all the friction coefficients shown. In some cases (for small  $\mu$ ), the maximal  $s_{\text{dev}}$  is reached before the maximum deviatoric strain applied ( $\epsilon_{\text{dev}}^{\text{max}} = 0.1549$ ) is reached. For some of the configurations studied, an asymptote (or steady state) is observed in which further application of deviatoric strain does not lead to visible further increase/decrease in the deviatoric stress. At the maximum applied deviatoric strain, we observe that not all configurations (especially the highest friction coefficients) have reached full saturation. For the systems with lower microscopic friction coefficients, a slight decrease of the deviatoric stress ratio for larger deviatoric strains is seen. The slope of the deviatoric stress ratio, which represents its growth rate shows a decreasing trend with increasing friction. Recall that the initial packings are different since they are prepared with different friction coefficients. Due to this, the pressure increases with increasing friction while the coordination number decreases with friction. The slope of the deviatoric stress ratio in Fig. 3.3a, related to the initial shear stiffness of the isotropic packing is proportional to these two quantities [37, 100, 167].

The evolution of the deviatoric stress during unloading (after strain reversal) is presented in Fig. 3.3b. Note that due to the square-root definition used in Eq. (3.14), the deviatoric stress remains positive<sup>1</sup> During deviatoric unloading,  $s_{\text{dev}}$  begins to decrease until the system approaches an isotropic stress configuration, where  $s_{\text{dev}} = 0$ . The  $\epsilon_{\text{dev}}$  values where  $s_{\text{dev}} \approx 0$  consistently decrease with increasing friction – as consistent with the trend of the maximum  $s_{\text{dev}}$  values reached during uniaxial loading at larger  $\epsilon_{\text{dev}}$  for stronger friction. For systems with large friction coefficients ( $\mu = 0.3, 0.5$  and  $1.0$ ), the  $\epsilon_{\text{dev}}$  values at which  $s_{\text{dev}} = 0$  are closer to each other than for weakly frictional systems – see Fig. 3.9 below.

Along with the deviatoric stress ratio, for a characterization of the contact network of the particles, we plot the deviatoric fabric magnitudes  $F_{\text{dev}}$  of the systems discussed above as function of the deviatoric strain during uniaxial loading and unloading in Figs. 3.3c and 3.3d, respectively. In Fig. 3.3c, the deviatoric fabric magnitude builds up from different (random, but small) initial values and reaches different maxima within the same range of deviatoric strain ( $\epsilon_{\text{dev}} \approx 4 - 6\%$ ). For larger strains, we observe a decrease in the structural anisotropy towards zero. Interestingly, for systems with higher friction coefficients ( $\mu = 0.3, 0.5$  and  $1.0$ ), after the decrease in the structural anisotropy, further loading in the axial direction leads to a (small) second increase of the deviatoric fabric, until at maximum compression, the deviatoric fabric again reaches a local maximum.

This is explained by the fact that more contacts are created in the axial compressive direction compared to the horizontal plane at the beginning of the loading cycle. At the first maximum

---

<sup>1</sup>An alternative way to enforce the sign convention is to multiply the deviatoric stress Eq. (3.14) by the sign of the difference between the eigenvalue of the main compressive direction and the average in the other two fixed directions as given for fabric in Eq. (3.19). This leads to positive and negative  $s_{\text{dev}}$ , which should take care of the strain reversal [80].



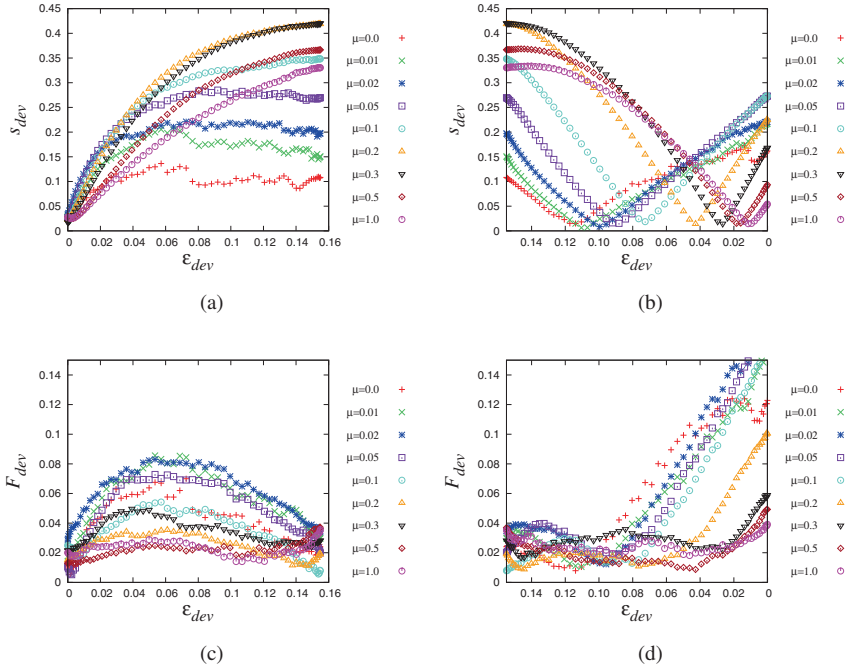


Figure 3.3: The deviatoric stress ratio plotted as function of deviatoric strain during uniaxial (a) loading and (b) unloading. The corresponding plots of the deviatoric fabric plotted during uniaxial (c) loading and (d) unloading, for different microscopic friction coefficients.

( $\epsilon_{dev} \approx 0.06$ ), the material behavior changes such that the number of contacts created in the horizontal plane becomes higher with respect to the vertical plane. This trend reverses again as maximum compression is reached for systems with higher friction coefficients. This interesting behavior will be further discussed when we analyze the magnitude and orientation of the respective eigenvectors in Section 3.4.3.

After strain reversal, as presented in Fig. 3.3d, the initial isotropic state is not recovered – a clear signature of history dependence and structural anisotropy being independent of (or decoupled from) the deviatoric stress ratio. Additionally, a strong difference can be seen in the fabric response of systems with lower and higher friction, respectively. As we will see later, the orientation of the eigenvalues of these systems provide interesting insights into these observations.

In general, comparing the evolution of deviatoric stress ratio and deviatoric fabric, we observe a strongly decoupled and non-linear qualitative behavior with the linear contact model used in this study. This confirms that the non-linearity observed is a peculiarity of the deformation mode and the structure of the packing.

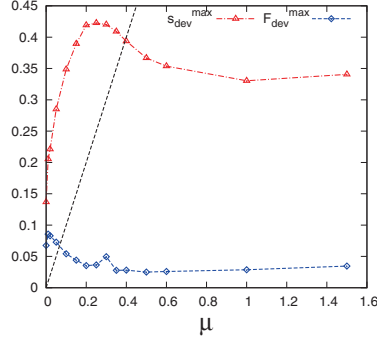


Figure 3.4: Trend of the peak deviatoric stress and peak deviatoric fabric with increasing microscopic friction coefficient  $\mu$  under uniaxial loading, given a maximal strain  $\varepsilon_{\text{dev}}^{\text{max}} = 0.1549$ .  $s_{\text{dev}}^{\text{max}}$  values for  $\mu > 0.1$  are taken at  $\varepsilon_{\text{dev}}^{\text{max}}$  since no clear maximum is achieved. Dashed line indicates  $\mu^{\text{macro}} = \mu$ .

In Fig. 3.4, we plot the maximum deviatoric stress ratio and maximum deviatoric fabric reached from Figs. 3.3a and 3.3c for the respective friction coefficients. Interestingly, the maximum deviatoric stress ratios increase with increasing friction coefficient until  $\mu \approx 0.25$ , where it peaks at  $s_{\text{dev}}^{\text{max}} \approx 0.43$  and subsequently decrease for higher friction coefficients. From Fig. 3.3a we observe that the highest friction coefficients (between  $\mu = 0.1$  and 1.0) appear not to have reached a final saturation; the application of further strain could lead to a higher maximum deviatoric stress ratio. Due to this, the decrease in the maximum deviatoric stress ratio at higher friction coefficients under uniaxial compression requires further attention. For our system where we control volume, we argue that at a maximum volume fraction  $v_{\text{max}} = 0.82$ , we are already close to the upper limit for realistic deformations with about 5% average overlaps, i.e. compression is very strong. Note that the maximum deviatoric stress ratio reached is termed the “macroscopic friction coefficient”,  $\mu^{\text{macro}} := s_{\text{dev}}^{\text{max}}$  [60], representing the macroscopic mobilized friction, i.e. shear resistance of the material. We note that the maxima reached are higher than the microscopic friction coefficient for systems with low friction, between  $\mu = 0$  and 0.4, while for higher friction, the maxima are lower [163].

In Fig. 3.4, we also show the trend of the maximum structural anisotropy reached,  $F_{\text{dev}}^{\text{max}}$ , with increasing friction. Besides the increase between,  $\mu = 0$  and 0.01, the maximum deviatoric fabric shows a decreasing trend with increasing friction and saturates at  $F_{\text{dev}}^{\text{max}} \approx 0.025$  for the highest friction coefficients. In comparison, the structural anisotropy is much smaller than the deviatoric stress ratio and it is reached at comparable  $\varepsilon_{\text{dev}}$ , whereas the extreme stress anisotropy is reached much later for higher  $\mu$ . Under triaxial loading, the coordination number decreases with increasing strain (dilatancy) while it increases under uniaxial loading (due to ongoing compaction). The decrease in the structural anisotropy with increasing friction is different from observations reported for triaxial tests [15, 74] where the maximal structural anisotropy is observed to increase with increasing friction. In frictionless systems,

the maximum fabric anisotropy decreases as the distance from the jamming volume fraction increases [60]. For our system and preparation procedure, the distance from the jamming point increases with increasing friction, so that  $F_{dev}^{max}$  consequently decreases.

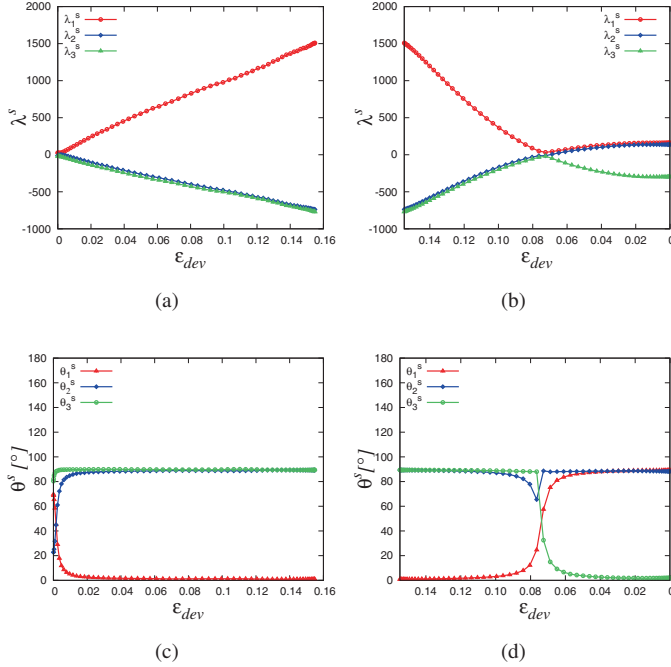


Figure 3.5: Eigenvalues of stress for  $\mu = 0.1$  plotted as functions of the deviatoric strain for (a) loading and (b) unloading along with their corresponding orientations with respect to the compressive direction during uniaxial (c) loading and (d) unloading.

### 3.4.3 Eigenvalues and Eigenvectors of Stress and Fabric

In this section, we will discuss the magnitude of the eigenvalues of deviatoric stress and deviatoric fabric during uniaxial loading and unloading as well as the orientation of the eigenvectors. As reference and representative example, we will show the data for only one of the coefficients of friction ( $\mu = 0.1$ ) and discuss in words the interesting trends for the others. Finally, we will couple the observations to the evolution of stress and structural anisotropies presented in section 3.4.2.

In Figs. 3.5a and 3.5b, we plot the eigenvalues of the deviatoric stress for the frictional system with  $\mu = 0.1$  during loading and unloading against deviatoric strain  $\epsilon_{dev}$ . During loading  $\lambda_1^s$  which corresponds to the stress eigenvalue of the axial compression direction increases

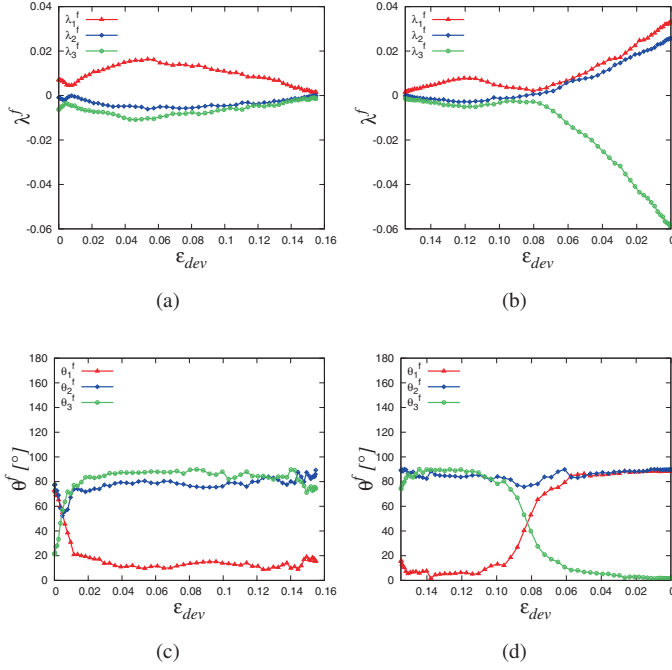


Figure 3.6: Eigenvalues of the deviatoric fabric for  $\mu = 0.1$  plotted as functions of the deviatoric strain for (a) loading and (b) unloading along with their corresponding orientations with respect to the compressive direction during uniaxial (c) loading and (d) unloading.

linearly from 0 and remains positive while the eigenvalues  $\lambda_2^s$  and  $\lambda_3^s$  of the two non-mobile direction are negative and very similar in magnitude. During unloading,  $\lambda_1^s$  decreases but remains positive; at  $\epsilon_{dev} \approx 0.075$ , all eigenvalues become zero and then switch order, so that the axial direction eigenvalue is becoming increasingly negative. The intermediate  $\lambda_2^s$  then gets identical to  $\lambda_1^s$ , both growing to positive values. The orientation of the corresponding eigenvectors during loading and unloading are shown in Figs. 3.5c and 3.5d. At  $\epsilon_{dev} = 0$ , the orientations are different and random which is an indication of the almost isotropic initial configuration. With increasing strain,  $\theta_1^s$ , which corresponds to the orientation of the compressive stress eigenvalue, converges to  $\theta^s = 0^\circ$  and remains until the end of the loading path. During this period, the stress and strain eigenvectors are said to be colinear with respect to each other. On the other hand, the orientation  $\theta_2^s$  and  $\theta_3^s$  of the other eigenvalues also drops to  $\theta^s = 90^\circ$  showing a perpendicular alignment with respect to the compression direction. After strain reversal, the eigen-directions of stress do not instantaneously respond to the directional change until at  $\epsilon_{dev} \approx 0.10$  where  $\theta_1^s$  begins to increase to  $90^\circ$  and finally reaches at  $\epsilon_{dev} \approx 0.03$ . Accordingly,  $\theta_3^s$  drops to  $0^\circ$ , while  $\theta_2^s$  remains close to  $90^\circ$  all the time.

Shape factor	$\tau \approx 0$	$\tau \approx 0.5$	$\tau \approx 1$
$\Lambda^\sigma = \lambda_2^s / \lambda_1^s$	Random	-1/2	1
$\Lambda^f = \lambda_2^f / \lambda_1^f$	Random	-1/2	1
$\Lambda^{(-\epsilon)} = \epsilon_d^{(2)} / \epsilon_d^{(1)}$	Undefined	-1/2	1

Table 3.2: Shape-factors of stress and fabric in the respective tensor eigensystem at the beginning, maximum and end of uniaxial compression.

The corresponding eigenvalue and eigenvector orientations of the deviatoric fabric for  $\mu = 0.1$  are presented in Figs. 3.6a and 3.6b during uniaxial loading and unloading. Similar to the eigenvalues of stress, the major eigenvalue  $\lambda_1^f$ , remains positive while the two lower eigenvalues are negative. In contrast to stress,  $\lambda_1^f$  increases and reaches a peak at  $\epsilon_{\text{dev}} \approx 0.05$  after which it begins to decrease towards zero as the maximum strain is approached. Also,  $\lambda_2^f$  and  $\lambda_3^f$  are not identical, i.e.,  $\lambda_3^f$  has a slightly higher magnitude than  $\lambda_2^f$ . This is an indication of the existence of anisotropy in the plane perpendicular to  $\lambda_1^f$  even though the stress picture shows isotropy. At maximum deviatoric strain, however, the magnitudes of all the eigenvalues are close to zero. After strain reversal,  $\lambda_1^f$  and  $\lambda_2^f$  show an increasingly positive trend from  $\epsilon_{\text{dev}} \approx 0.08$  but are not exactly identical in magnitude while  $\lambda_1^f$  is negative and consistently decreases from  $\epsilon_{\text{dev}} \approx 0.08$  until the end of the decompression cycle.

Similar to the stress, the orientations of the fabric components are interesting. Starting from random values,  $\theta_1^f$  decreases and is close but distinct from  $0^\circ$  during loading, while  $\theta_2^f$  and  $\theta_3^f$  are close to  $90^\circ$  during the same period. This indicates that  $\theta_1^f$  is not fully aligned with the strain eigenvector with the deviation showing the non-colinearity. After strain reversal, a delay can be seen before  $\theta_1^f$  and  $\theta_3^f$  transit to  $90^\circ$  and  $0^\circ$ , respectively, while  $\theta_2^f$  remains close to  $90^\circ$ .

Additionally, to fully describe the tensors, one can calculate the respective shape factors for stress and fabric, respectively, as the ratio of the eigenvalues as shown in Table 3.2 at the initial, maximum and end of the uniaxial compression–decompression cycle.

In the following analysis, we will investigate how the orientation changes with increasing the microscopic friction coefficient and the relationships with the force network.

In Figs. 3.7a and 3.7b, we plot the orientations of the first eigenvectors of stress  $\theta_1^s$  and fabric  $\theta_1^f$  for all contacts and different friction coefficients, respectively. The initial value of  $\theta_1^s$  is random at the beginning of the loading path for the different friction coefficients. As loading begins,  $\theta_1^s$  decreases and at  $\epsilon_{\text{dev}} \approx 0.02$ ,  $\theta_1^s \approx 0^\circ$  for all friction. The relaxation rate (data scaled with the initial value of the respective  $\theta_1^s$ ), shown as an inset on a log-scale is non-systematic for the different friction coefficients possibly due to the initial isotropic configuration. Note that since the angle  $\theta_1^s$  does not exactly decrease to zero since  $\theta_1^s$  is always positive even though it fluctuates around zero. Observing the behavior of the eigenvectors

$\hat{n}_x$  and  $\hat{n}_y$  of the largest eigenvalue, we find that during loading, they approach zero (aligned with the compression direction) and remain until maximum compression. After strain reversal, a slight delay is seen before the vectors finally flip back to the plane [53]. After strain reversal at  $\epsilon_{\text{dev}} = 0.16$ , the response of  $\theta_{1(s)}$  is slow and it only begins to increase at  $\epsilon_{\text{dev}} \approx 0.12$  for  $\mu = 0$ . It is interesting to note that the delay time increases with friction and possibly due to the higher maximum deviatoric stress values reported with increasing friction. The corresponding orientation of the major eigenvector of fabric  $\theta_{1(f)}$  for all contacts and different friction coefficients also starts from different random values before decreasing to  $0^\circ$  with increasing loading. Surprisingly at  $\epsilon_{\text{dev}} = 0.08$ , for the configurations with lower friction ( $\mu = 0, 0.01, 0.02$  and  $0.05$ ),  $\theta_{1(f)}$  remains close to  $0^\circ$  while those with higher friction ( $\mu = 0.2, 0.3, 0.5$  and  $1.0$ ) begin to increase towards  $90^\circ$  as we approach maximum compression. This indicates that the orientations and build-up of contacts for systems with lower/higher friction behave in opposite fashion to each other and makes clear the reason for the decrease seen in the deviatoric fabric evolution in Fig. 3.6a. At the lower friction case, with increasing loading, contacts are mostly built along the main compression direction. However with increasing friction, a ‘saturation’ of contact build-up in the vertical direction sets in and an increasing number of contacts begin to build-up in the horizontal direction. As strain is reversed, the eigenvector orientation for systems with low friction increases to  $90^\circ$  while a decrease before an increase to  $90^\circ$  is seen for systems with higher friction.

To further understand this interesting observation we sub-divide the respective systems into strong and weak contacts and we plot the orientation of the stress and fabric eigenvector corresponding to the compression direction for the two sub-divisions. Strong contacts are termed as those whose normal force intensity is greater than the mean normal force while those with lower intensity with respect to the mean normal force are termed weak.

We plot the orientation of the major direction eigenvector of stress and fabric respectively in Figs. 3.7c and 3.7d for strong contacts. From Fig. 3.7c, the orientation of the strong contact main eigenvector of stress and fabric behaves in a similar fashion as the total contact in the ensemble. This is consistent with earlier findings [158] where the strong contacts have been observed to carry most of the load during deformation. Interestingly and in contrast to the observation for all contacts, the fabric eigenvalue for systems with both low and high friction all stay close to  $0^\circ$  during loading and initial unloading.

Next, the orientation of the main eigenvector of stress and fabric for weak contacts is shown in Figs. 3.7e and 3.7f. Similar to the strong contacts, the stress and fabric orientation of weak contacts behave in a similar fashion but in contrast are mostly oriented at  $90^\circ$  during loading. During unloading, the orientation tends towards  $0^\circ$ .

Comparing Figs. 3.7b, 3.7d and 3.7f, it can be seen that strong contacts predominate for the system with very low friction while for higher friction, the orientation of the weak contacts play a much significant role.

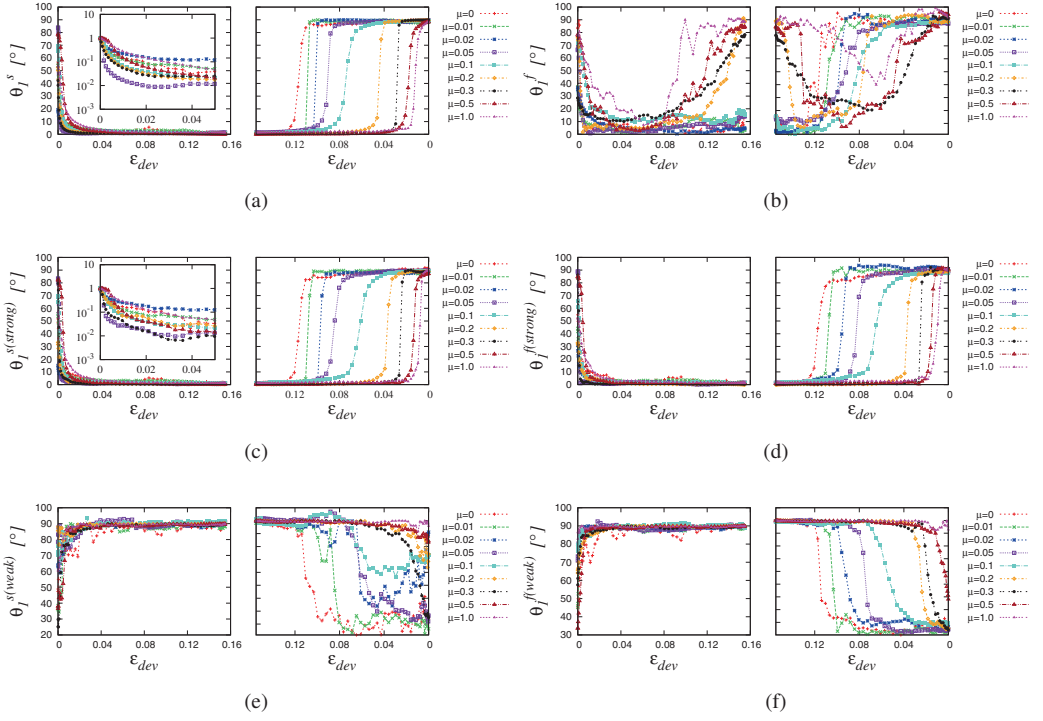


Figure 3.7: Orientation of the largest positive (a) Stress eigenvector for all contacts (b) fabric eigenvector for all contacts (c) Stress eigenvector for strong contacts (d) Fabric eigenvector for strong contacts (e) Stress eigenvector for weak contacts (f) Fabric eigenvector for weak contacts plotted against dimensionless time for different coefficient of friction.

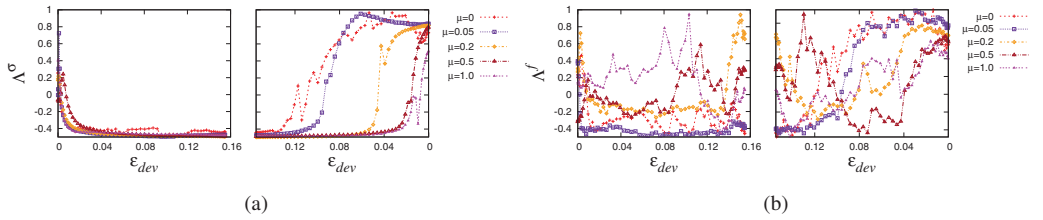


Figure 3.8: Shape factors of (a) stress and (b) fabric as function of the deviatoric strain for some exemplary friction coefficients.

We also plot the respective shape factors as ratio of the eigenvalues of stress and fabric for some exemplary friction coefficients during uniaxial loading and unloading in Fig. 3.8. For stress, shown in Fig. 3.8a, beginning from random values,  $\Lambda^\sigma$  decreases to  $-1/2$  during load-

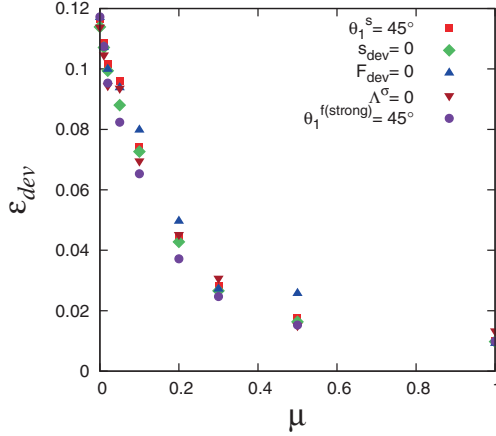


Figure 3.9: Strains at which the orientations of the stress eigenvectors cross  $\theta = 45^\circ$  and at which the deviatoric stress ratio, deviatoric fabric and the stress shape factor cross zero for frictions  $\mu = 0, 0.01, 0.02, 0.05, 0.1, 0.2, 0.5$  and  $1.0$ .

ing and reverses to 1 at the end of the unloading cycle. The rates of change during loading and unloading are almost identical, for different  $\mu$  while during unloading, the deviatoric strain at which the increase occurs decreases with increasing friction. As with the stress, the shape factor of fabric  $\Lambda^f$ , shown in Fig. 3.8b, also begins from random values and during loading approaches  $\Lambda^f \approx -1/2$  with stronger fluctuations for higher friction coefficients. At the end of unloading however  $\Lambda^f$  approach unity.

In Fig. 3.9, we plot the deviatoric strains at which the major eigenvalues  $\theta_1^s$  cross  $45^\circ$  during unloading for different friction coefficients. Additionally, we also plot the deviatoric strains at which the deviatoric stress ratio, deviatoric fabric and the stress shape factor cross zero from Figs. 3.3b, 3.3d and 3.8a, respectively. As shown, the transition point decreases non-linearly with increasing friction. All data originating from the stress tensor, namely the major eigenvalue of stress, its orientation and the stress shape factor all collapse on each other. On the other hand, it is not surprising that the transition points for the fabric quantities are slightly off since the fabric behaves differently from the stress. The definition of the fabric tensor takes into account only the normal directions and does not include the strong tangential contributions to the contacts. Therefore, as friction is increased, the deviations can be stronger.

In the following section, we will investigate in more detail the fraction of weak and strong contacts in these systems and discuss their interplay and relation to the observations on the orientations of the strong and weak contacts. For clarity and to better view the evolution of the quantities, instead of the deviatoric strain  $\epsilon_{dev}$ , we will study the evolution of the quantities against dimensionless time  $\tau = t/T$  – where  $T$  is the simulation time.



### 3.4.4 Friction Mobilization

Mobilization of contact friction, during uniaxial deformation of the bulk material, is quantified by the factor  $f_i/\mu f_n \leq 1$  for each contact. The tangential forces grow towards their limit and support larger shear stress; for tangential forces at/above the Coulomb limit, i.e., at fully mobilized friction, sliding sets in and rearrangements of contacts can lead to new, more stable configurations. It has been observed [147] that sliding is *mostly* active at weak contacts (termed weak sliding, *wsl*), while stronger contacts stay in the sticking regime and sustain larger friction forces while being less mobilized (termed strong sticking *sst*). We refer to this as the *ws*-rule. Weak and strong contacts are defined relative to the average normal force at each timestep;

$$f^* = f_n/\langle f_n \rangle < 1 \quad (3.22)$$

are termed weak and

$$f^* = f_n/\langle f_n \rangle > 1 \quad (3.23)$$

are termed strong [147], with dominating sliding and sticking, respectively.

As we will see shortly, we find that this friction mobilization rule may not strictly hold in certain cases, as there may be a considerable number of weak contacts with friction not fully mobilized (termed weak sticking, *wst*), as well as strong contacts fully mobilized (termed strong sliding, *sst*).

As representative examples, in Fig. 3.10, we track two different contacting pairs during uniaxial loading and unloading of the system with  $\mu = 0.1$  and study the force intensity and friction mobilization as they evolve as function of the dimensionless time  $\tau$ . For the first contact pair shown in Fig. 3.10a, during the first stages of loading, the contact is weak since  $f^* < 1$ ; friction is fully mobilized and sliding occurs at the contact, i.e. weak contacts tend to full friction mobilization. For a short period at  $\tau \approx 0.2$ , the contact becomes stronger and  $f_i/\mu f_n$  correspondingly reduces (with strong fluctuations) indicating a strong contact where sticking predominates. At  $\tau \approx 0.36$ , the contact between this particle pair is lost (opened) and is only recovered at  $\tau \approx 0.7$ , where it can again be classified as weak sliding (*wsl*) contact. As the end of the compression cycle is reached, the contact intensity increases and  $f_i/\mu f_n$  decreases, with strong fluctuations again, and sometimes sliding. In general, the *ws*-rule is mostly true for this contact pair except during the transition from weak to strong where some fluctuations in  $f_i/\mu f_n$  can be seen, transitions from sliding to sticking can happen for weak contacts (*wst*) well below  $f^* = 1$  during increase of  $f^*$ , but also sliding can happen for strong contacts (*sst*).

The second contact pair shown in Fig. 3.10b is even more interesting. Like the first particle pair, the second pair also begin as a weak sliding contact and  $f^*$  grows until  $\tau \approx 0.15$ , where

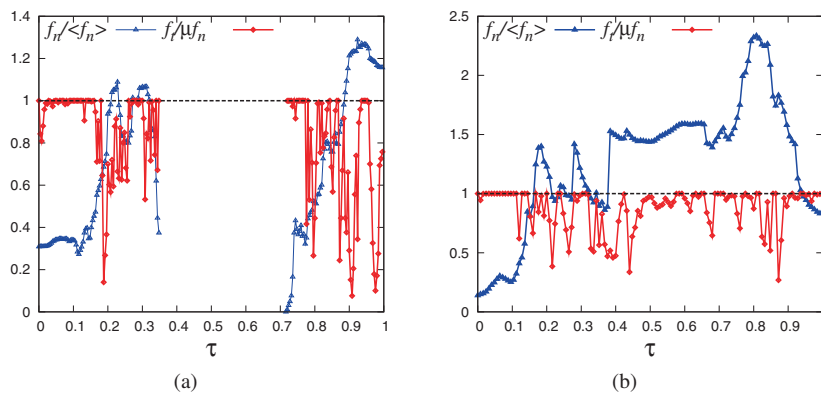


Figure 3.10: Tracking  $f_i/\mu f_n$  and  $f^* = f_n/\langle f_n \rangle$  for two single particle pairs randomly selected from the ensemble during compression and decompression where  $\tau$  is the dimensionless time. (a) Particle pair 1 (b) Particle pair 2.

it becomes strong. Interestingly, while the contact remains very strong for almost all of the loading–unloading cycle, friction is highly mobilized  $f_i/\mu f_n$  remains close to 1.

Since studying just two contact pairs within an ensemble containing tens of thousands of contacts provides very little information, we first extract the total fraction of weak and strong contacts in the system. In Fig. 3.11a, we plot the total proportion of weak contacts with reference to the total number of contacts for the different friction coefficients (which was studied in detail in Refs. [60, 79] so that those data are not shown here). Surprisingly, as with the orientation of the largest eigenvalue of fabric for weak and strong forces plotted in Fig. 3.7, we see a clear difference between the fraction of weak and strong contacts. In the following, we will discuss in detail the observations for weak contacts – which have opposite trends as the observations for strong contacts.

The first observation from Fig. 3.11a is that a greater fraction (over 50%) of the contacts in the respective systems are weak – an indication that fewer contacts carry a larger than average proportion of the load in the system, which is due to the shape of the force probability density function  $P(f^*)$ , see Section 3.4.5. Secondly, for systems with lower friction, the fraction of weak contacts at the beginning of the loading cycle is significantly higher than for higher friction, meaning that the load is more evenly (not exactly proportionally) distributed between weak and strong contacts for systems with higher friction coefficient. With increasing loading, while the total number  $C_{tot}$  strongly increases (not shown), the fraction of weak contacts decreases for packings with lower friction coefficients, and increases for those with higher friction. Also, the decrease of weak contacts with increasing loading for lower friction systems is stronger and occurs earlier than the increase for systems with higher friction. At maximum loading  $\tau = 0.5$ , the proportion of weak contacts are close for all fric-

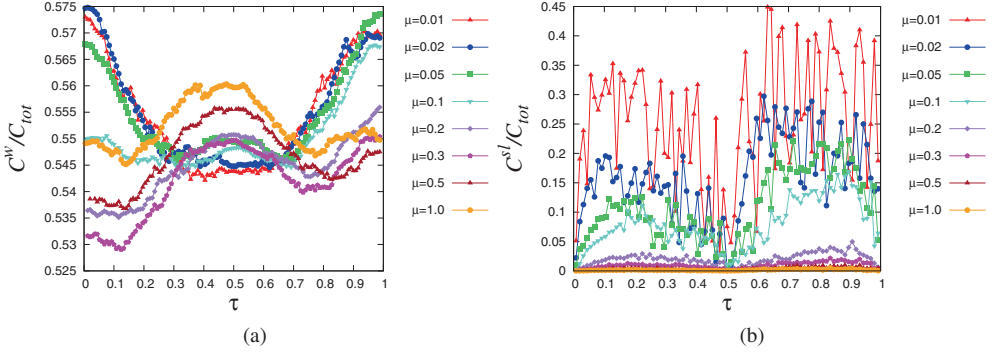


Figure 3.11: Proportion of (a) weak contacts (c) sliding contacts with respect to the total number of contacts during uniaxial loading- and unloading-cycle for different friction coefficients.

tion coefficients with slightly higher fraction for the highest friction coefficients  $\mu = 0.5$  and  $1.0$ . This observation, that the packings with higher friction behave in a qualitatively different fashion, is consistent with the earlier observation in Fig.3.7b, where the difference in orientation of strong/weak contacts for low/high friction coefficients can be seen too.

It is surprising that the fractions of weak contacts are close for systems with lower friction and evolve in a similar (almost symmetric) fashion during loading and unloading. For  $\mu = 0.01$  and  $0.05$ , the fractions of weak contacts at the end of unloading are slightly lower than at the beginning of loading. With increasing friction, the fractions of weak contacts at the end of unloading are higher than at the beginning of loading; the anti-symmetry between the loading and unloading phases is more visible for  $\mu \geq 0.1$ .

To evaluate the proportion of weak and strong contacts contributing to sliding and sticking at contacts, we plot in Fig. 3.12, the number of weak sliding ( $\sum wsl$ ) and strong sticking ( $\sum sst$ ) contacts with respect to the the total weak ( $\sum w$ ) and strong ( $\sum s$ ) contacts, respectively. From Fig. 3.12a, the fraction of weak sliding contacts grows during loading and reaches a peak before it begins to decrease towards zero as maximum loading ( $\tau = 0.5$ ) is approached. The initial growth rate of the weak sliding contacts and the peak reached decreases with increasing friction but all approach zero at  $\tau = 0.5$  because the deformation rate decreases to zero before reversal. During unloading, a second growth phase of the weak sliding contacts is seen and the maximum reached is higher than that reached during loading – thus leading to a non-symmetry around  $\tau = 0.5$ . Additionally, only a small proportion (much less than  $\approx 50\%$ ) of the total weak contacts are sliding. This indicates that even though an increase in the number of weak sliding contacts is seen during loading and unloading, more and more weak contacts stick ( $f_t/\mu f_n < 1$ ) for increasing  $\mu$ .

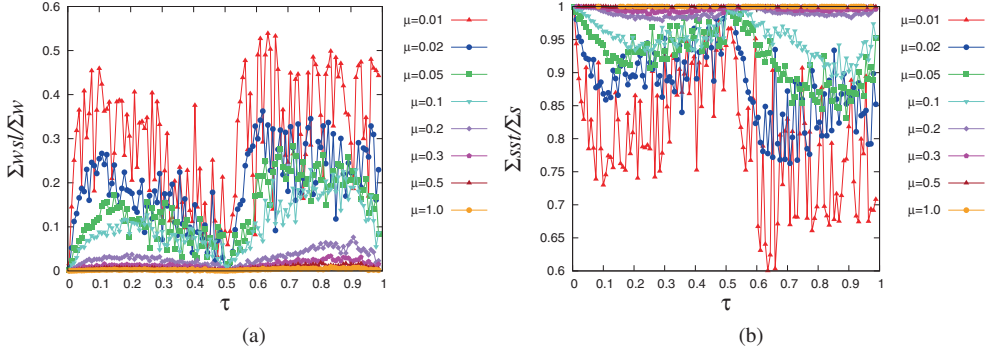


Figure 3.12: Fraction of (a) weak sliding contacts ( $wsI$ ) and (b) strong sticking contacts ( $sst$ ) with respect to the total number of weak ( $\Sigma w$ ) and strong ( $\Sigma s$ ) contacts, respectively, during uniaxial loading- and unloading for different friction coefficients.

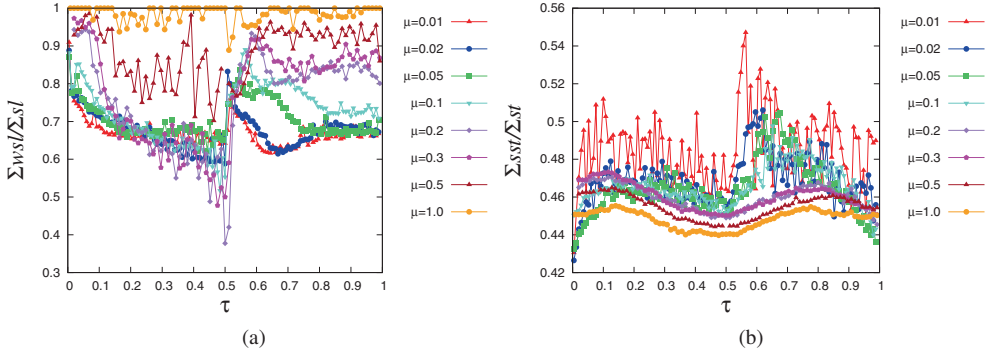


Figure 3.13: Fraction of (a) weak sliding contacts ( $wsI$ ) and (b) strong sticking contacts ( $sst$ ) with respect to the total number of sliding ( $\Sigma sl$ ) and sticking ( $\Sigma st$ ) contacts, respectively, during uniaxial loading- and unloading for different friction coefficients.

In contrast to the weak sliding contacts, the fraction of strong sticking contacts, as presented in Fig. 3.12b decreases during loading until it reaches a minimum before an increase towards  $\tau = 0.5$  can be seen. The rate of decrease and the minima reached decrease with increasing friction and the minima are lower during unloading, i.e. all data are non-symmetric around  $\tau = 0.5$ .

In Fig. 3.13, we plot the number of weak sliding ( $\Sigma wsl$ ) and strong sticking ( $\Sigma sst$ ) contacts with respect to the total sliding and sticking contacts, respectively. In Fig. 3.13a, we confirm that a higher proportion ( $> 0.5$ ) of the sliding contacts are weak [17, 18, 147, 148]. The proportions of weak sliding contacts for  $\mu = 0.01 - 0.3$  are almost identical and decrease

during loading. During unloading, however, the proportions of weak sliding contacts behave differently with increasing friction. We again observe the non-symmetry of the loading and unloading data. In Fig. 3.13b, we plot the fraction of strong sticking contacts with respect to the total sticking contacts. A little less than 50 % of the sticking contacts are strong. The fractions of strong sticking contacts increase initially during loading and later decrease as maximum compression is approached. The fraction of strong sticking contacts show a decreasing trend at  $\tau = 0.5$  with increasing  $\mu$ . During unloading, the fractions of strong sticking contacts increase and later decrease towards the end of the unloading branch. With increasing friction, the non-symmetry of the data decreases. For the highest friction coefficients, the fraction of strong sticking contacts during loading is slightly more than those present during unloading.

In summary, strong and weak forces have been analyzed along with the level of friction mobilization. It has been shown that a higher proportion of the total contacts in the system are weak, irrespective of the friction coefficient. Among these weak contacts, the contacts which are sliding are less in number compared to the sticking contacts. In contrast, when the total sliding contacts are considered, a higher proportion of them are weak, as also reported in earlier literature.

### 3.4.5 Probability density function

To better understand the relationship between contact forces and the macroscopic stress and structure, we first study the probability density function of normal contact forces in different directions [74, 76].

In the following analysis, we will consider the probability distribution of the normal forces during uniaxial compression with reference to the compressive  $z$ -direction and the two lateral  $x$  and  $y$ -direction. Keeping each direction as reference, we define a cut off  $\chi$  such that the contact forces admitted for the probability distribution analysis fulfill the criteria  $|\hat{n}_c \cdot \hat{n}_\epsilon| > \chi$  where  $\hat{n}_c$  is the normal unit vector of the reference direction and  $\hat{n}_\epsilon$  is the strain eigenvector corresponding to a compressive or tensile direction. The strain eigenvector is fixed due to the deformation mode, but will be different for other test set-ups. In the case  $\chi = 0$ , all contact forces in the ensemble will be considered while no contacts exist when  $\chi = 1$ . For the present study, we set  $\chi = 0.8$  and only note that as  $\chi$  approaches 1, less data are available and the noise level increases, but not changing much the following results.

In Fig. 3.14, we plot the normalized probability density of the normal force  $P(f/\langle f_{all} \rangle)$  against the normalized force  $f_* = f/\langle f_{all} \rangle$  for the three reference directions ( $x$ ,  $y$  and  $z$ ) and for all contacts. In this case,  $\mu = 0.1$  and cut-off  $\chi$  has been set to 0.8. To allow for comparison, the forces have been normalized with the mean of the normal force for all contacts. As shown in Fig. 3.14a, at  $\tau = 0$ , the force probabilities from the three reference directions

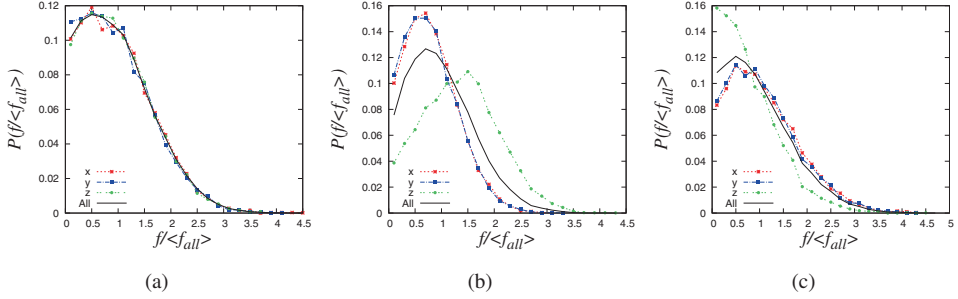


Figure 3.14: Normalized probability density of the normal force  $P(f/\langle f_{all} \rangle)$  for the three reference directions and for all contacts forces plotted against the normalized force  $f_* = f/\langle f_{all} \rangle$  for  $\mu = 0.1$  and cut-off  $\chi = 0.8$ . Three snapshots are shown at (a) initial,  $\tau = 0$ , (b) maximum,  $\tau = 0.5$ , and (c) final,  $\tau = 1.0$  compression.

and for all contacts are virtually the same evidenced by the apparent collapse of the different curves on each other. This is not surprising since the initial state is isotropic and no direction-dependent deformation has taken place. At maximum compression (in Fig. 3.14b), a difference between the force distribution in the compression  $z$ -direction and the radial  $x$  and  $y$  direction is evident. Firstly, we observe that the force probability in the radial directions ( $x, y$ ) are close since no active deformation takes place in these directions. Another observation is that the proportion of weak forces in the radial direction significantly exceeds those in the compression direction. Also, the mean force in the  $z$ -direction is observed to be higher than in the radial direction. At maximum compression, we observe a wider distribution in the compressive  $z$ -direction compared to the force distribution for all contacts and the two lateral directions.

The longer tail seen in the force distribution in the  $z$ -direction is due to the presence of stronger forces compared to the other directions. At the end of the decompression cycle, shown in Fig. 3.14c, we observe that the initial state is not recovered due to the deformation history of the sample and there is a higher proportion of weak forces in the decompression  $z$ -direction compared to the radial directions.

### 3.5 Polar Representation

To understand the orientation and arrangement of the contacts over the whole angular spectrum during uniaxial deformations, we introduce now the polar representation of contacts, forces and mobilized friction. For the analysis, we test two different averaging methods, namely the constant bin width ( $b$ ) and constant height ( $h$ ), which give comparable results

and are shown in detail in Appendix I. In the following, we will use data obtained using the constant bin width method.

### 3.5.1 Harmonic approximations

The axial distribution of contact force orientations  $P(\theta)$ , along with the degree of anisotropy in a granular packing, can be approximated by a Legendre polynomial based on spherical harmonics of the form  $Y_l^m(\theta, \varphi)$  [19, 30, 74, 76]. The approximation is simplified by admitting only functions that are consistent with the symmetry of the deformation mode, namely functions independent with respect to  $\varphi$  and periodic as a function of  $\theta$ . With this criteria, the two lowest admissible functions are  $Y_0^0=1$  and  $Y_2^0 = 3 \cos^2 \theta - 1$  such that the second order harmonic representation of contacts is of the form:

$$P_2(\theta) = a_0[1 + \epsilon(3 \cos^2 \theta - 1)] \quad (3.24)$$

with the factor  $a_0$  as constant and a unique anisotropy descriptor  $\epsilon$ . In our case, due to normalization,  $a_0 \approx 0.5$ . For the uniaxial mode, snapshots of the contact probability density data are presented in Fig. 3.16a during uniaxial loading and unloading. We observe distributions with two peaks and a dip around  $\pi/2$  indicating that a higher order approximation is needed. The higher order needed for the present uniaxial dataset is possibly due to the peculiarity of the deformation mode. Unlike the triaxial test which involves an active stress control on the lateral boundaries of the system, the stress on the lateral boundaries of the uniaxial mode evolve, albeit with smaller magnitude in comparison to the stress in the axial direction.

Eq. (3.24) can be extended to admit higher order spherical harmonic functions with  $l = 4, 6$ . For  $l=4$ ,  $Y_4^0 = 35 \cos^4 \theta - 30 \cos^2 \theta + 3$  and for  $l=6$ ,  $Y_6^0 = 231 \cos^6 \theta - 315 \cos^4 \theta + 105 \cos^2 \theta - 5$  all with different prefactors. For a 6th order expansion, the contact distribution will take the form:

$$P_6(\theta) = a_0[1 + \epsilon_2 Y_2^0 + \epsilon_4 Y_4^0 + \epsilon_6 Y_6^0], \quad (3.25)$$

where the axial symmetry is implied. Eq. (3.25) introduces now three anisotropy state descriptors  $\epsilon_i$ , with  $i = 2, 4, 6$ . Also, Equations (3.24) and (3.25) can be further simplified for the well defined limits at  $\theta = 0, \pi/2$  and  $\pi$  as shown in Table 3.3.

Different methods of obtaining the anisotropy state descriptors have been attempted in this study. The details and comparison of the methods are discussed in Appendix II. For all methods, we consistently observe that the contact distribution is approximated by a sixth order

$\theta$	$P_2(\theta)$	$P_6(\theta)$
$\theta = 0$	$a_0[1 + 2\epsilon]$	$a_0[1 + 2\epsilon_2 + 8\epsilon_4 + 16\epsilon_6]$
$\theta = \pi/2$	$a_0[1 - \epsilon]$	$a_0[1 - \epsilon_2 + 3\epsilon_4 - 5\epsilon_6]$
$\theta = \pi$	$a_0[1 + 2\epsilon]$	$a_0[1 + 2\epsilon_2 + 8\epsilon_4 + 16\epsilon_6]$

Table 3.3: Second and sixth order harmonic expansion of the contact distribution for the axial direction (compression:  $\theta = 0, \pi$ ) and the lateral direction ( $\theta = \pi/2$ ).

polynomial with two peaks and a strong depression at  $\pi/2$ . In the following, as a reference case, we use the azimuthal fit to the constant probability data discussed in Appendix II.

### 3.5.2 Discussion of Results

Having established that the contact distribution is approximated by a sixth order distribution with three anisotropy state descriptors, we compare descriptors  $\epsilon_2$ ,  $\epsilon_4$  and  $\epsilon_6$  for different friction coefficients as functions of the deviatoric strain during uniaxial loading and unloading. From Fig. 3.15a, besides a slight increase in the maximum  $\epsilon_2$  values between  $\mu = 0$  and 0.02, the maximum  $\epsilon_2$  value shows a decreasing trend with friction and almost saturates for the highest friction coefficients. This is consistent with the trend of the maximum deviatoric fabric shown in Fig. 3.4. Also consistent with the deviatoric fabric evolution during unloading is that the initial state is not recovered. In Fig. 3.15b, beginning from different random values,  $\epsilon_4$  is negative and systematically decreases for all friction coefficients during loading followed by a slight increase during unloading. The descriptor  $\epsilon_6$  is distributed around zero and remains fairly constant during loading and unloading but has some variation within either deformation.

In addition to the contact probabilities in Fig. 3.16a, we now study the distribution for other quantities. The polar distributions of the normal force shown in Fig. 3.16b during loading displays a high and increasing normal force along the compression (axial  $0^\circ$ ) direction compared to the lateral ( $\pi/2$ ) direction reaching their maximum at  $\tau = 0.5$ . After strain reversal (unloading), the normal force in the tensile (extension) direction is reduced until the force in the lateral ( $\pi/2$ ) direction becomes higher. Interestingly, in contrast to  $P(\theta)$ , the distribution of the normal forces  $f_n(\theta)$  is well described by a second-order harmonic approximation similar to Eq. (3.24) during loading and unloading.

For the distribution of the tangential force and mobilized friction, shown respectively in Fig. 3.16c and 3.16d, we observe a distribution similar to that of the contacts shown in Fig. (3.19), with two strong peaks and a depression around  $\pi/2$ . This indicates the need for a higher order tensorial descriptor also for these two quantities that appear to be strongly re-



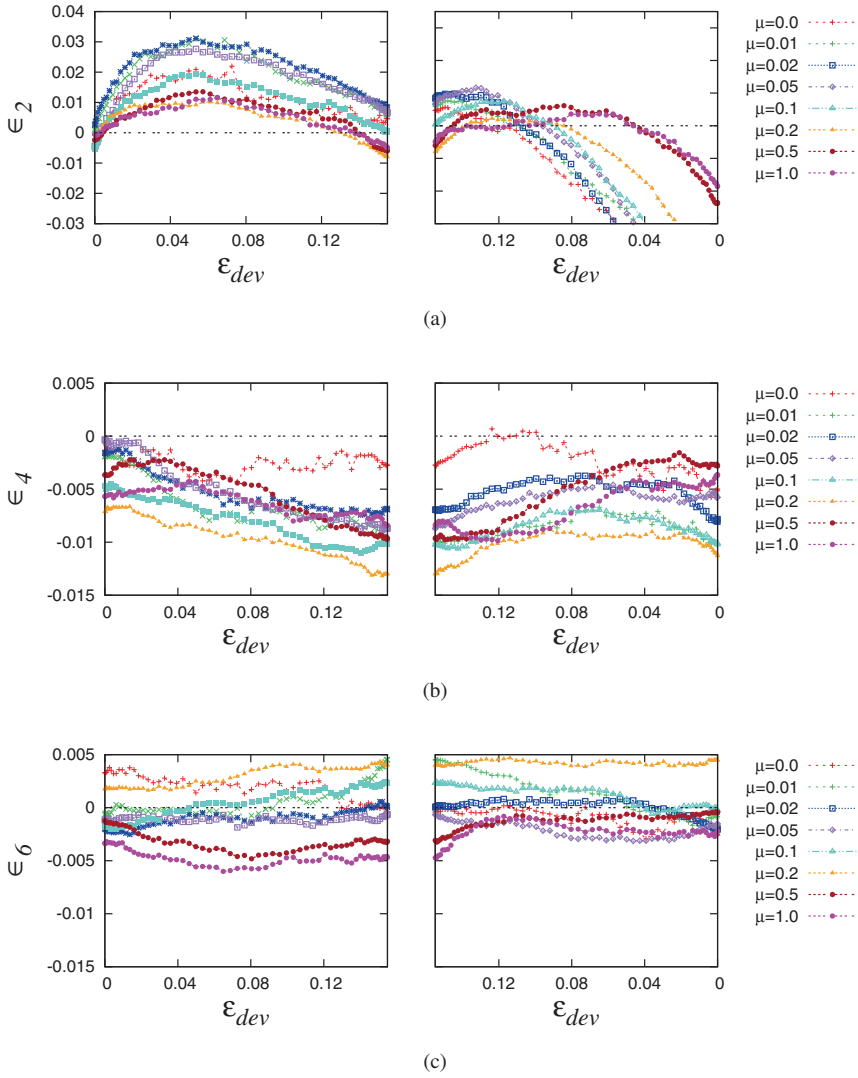


Figure 3.15: Comparison of the 6th order anisotropy state descriptors (a)  $\epsilon_2$  (b)  $\epsilon_4$  (c)  $\epsilon_6$  as a function of the deviatoric strain for different friction coefficients during loading (left) and unloading (right).

lated with the behavior of the contact network, rather than with the normal forces. Similar to  $f_n(\theta)$ , the distribution of the tangential force  $f_t(\theta)$  also shows an increase along the compression direction followed by a decrease during decompression. We also find that during loading, the mobilized friction increases along the tensile ( $\pi/2$ ) direction while remaining fairly stable and flat in the lateral direction. After strain reversal, the mobilized friction increases again along the tensile direction (which is now  $0^\circ$ ). Coupling these observations to

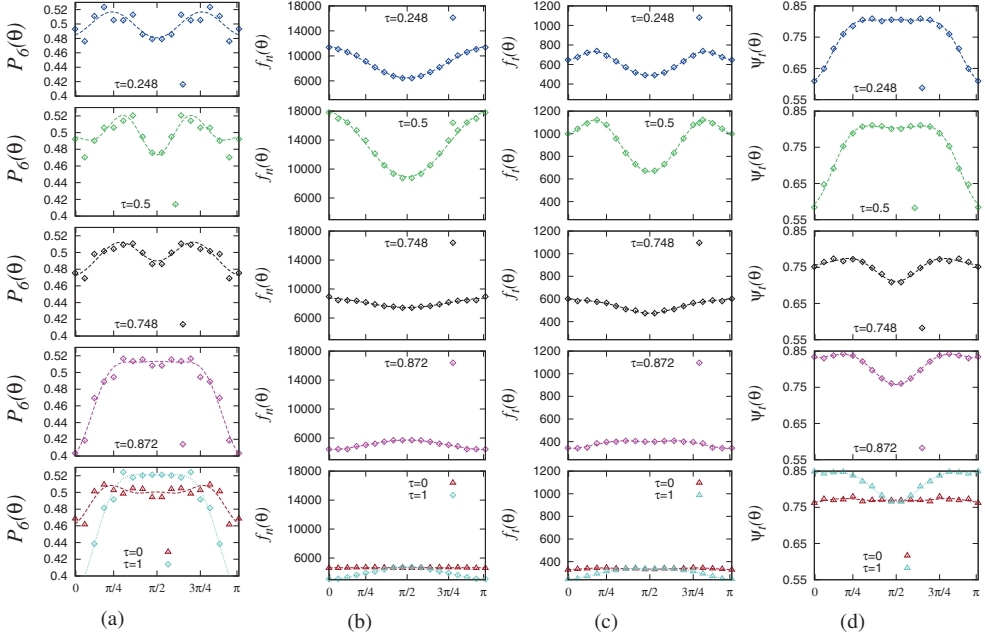


Figure 3.16: Snapshots of the polar distribution of the (a) contacts  $P_6(\theta)$  (b) normal force  $f_n(\theta)$  (c) tangential force  $f_t(\theta)$  (d) mobilized friction  $\psi_f(\theta)$  at different dimensionless time ( $\tau$ ) during uniaxial loading and unloading for friction  $\mu = 0.1$ .

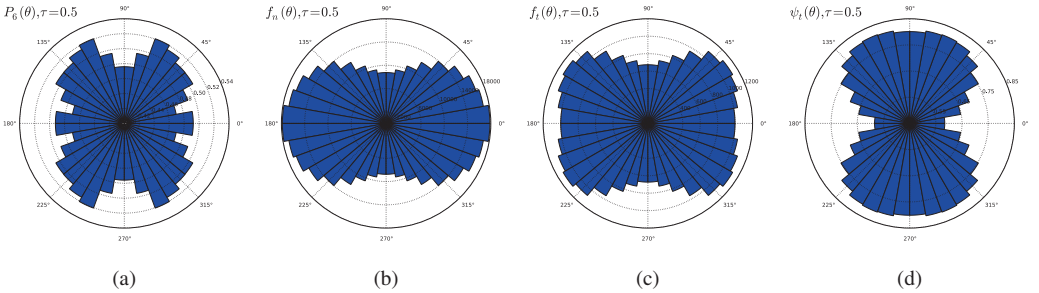


Figure 3.17: Polar distribution of the (a) contacts  $P_6(\theta)$  (b) normal force  $f_n(\theta)$  (c) tangential force  $f_t(\theta)$  (d) mobilized friction  $\psi_f(\theta)$  at dimensionless time ( $\tau = 0.5$ ) for friction  $\mu = 0.1$ .

the normal force distribution, we find that friction is less mobilized along the direction where stronger forces exist (compression) and more mobilized along the direction where weaker forces (tension) are seen. Similar to the directional probability distribution of the normal force presented in Section 3.4.5, the initial state (at  $\tau = 0$ ) which is mostly isotropic is not recovered at the end of unloading ( $\tau = 1$ ). As a complement, in Fig. 3.17, we show the

pictorial representation of the distributions of contacts, normal force, tangential force and mobilized friction at  $\tau = 0.5$  for the same dataset shown in Fig. 3.16, clearly visualizing the 4th and 6th harmonic contributions in 3.17a, 3.17c, and 3.17d.

### 3.6 Summary and Outlook

The discrete element method has been used to investigate the microscopic and macroscopic response of frictional, polydisperse granular assemblies under uniaxial loading and unloading paths. The main goal was to investigate the effects of contact friction on the force and contact network orientation and distribution and to relate this to the evolution of structural anisotropy – which is the key ingredient that quantifies the response of granular materials under non-isotropic loading conditions. Since the uniaxial test is widely realizable in laboratory experiments using various geometries, our findings should be relevant for both experimental and numerical researchers interested in the behavior of packings under different deformation and stress conditions. The present study covers a wide range of friction coefficients for systems that are already “jammed”. Since the boundary walls are periodic, the effects of walls and system geometry should be minimal, which allows to understand the bulk behavior with rather few particles ( $N \approx 10,000$ ).

As preparation procedure, in order to obtain homogeneous initial isotropic states, we attempted several preparation protocols and found that the methods lead to mostly identical initial states even though care has to be taken in the presence of friction which leads to protocol dependence. The evolution of the deviatoric stress ratio and the deviatoric fabric, as functions of the deviatoric strain, in the presence of friction, are different with respect to each other. Even though the contact model is linear, both quantities show a non-linear behavior due to the structural changes during loading and unloading. For the configurations with lower friction, a saturation in the deviatoric stress ratio during loading was observed. However, when friction is increased, a clear saturation of the deviatoric stress ratio is not seen within the same maximum strain. During loading, the deviatoric fabric, which quantifies the structural anisotropy reaches a maximum before maximum  $\varepsilon_{\text{dev}}$  independent of  $\mu$ , and then decreases as the maximum strain is approached. Interestingly for the higher friction coefficients, a second increase was observed. The peak deviatoric stress ratio  $s_{\text{dev}}^{\text{max}}$  reached during uniaxial loading increases up to  $\mu = 0.42$  and subsequently decreases for higher friction to  $\mu \approx 0.33$ . The peak deviatoric fabric reached  $F_{\text{dev}}^{\text{max}}$  largely shows a decreasing trend with increasing friction and eventually saturates at  $F_{\text{dev}}^{\text{max}} \approx 0.025$ .

The orientation of the largest stress eigenvector  $\theta_1^s$ , during loading with non-systematic rates aligns to  $0^\circ$ , i.e. the compression direction. When strain is reversed, we observe that  $\theta_1^s$  remains oriented along the vertical direction before reverting to  $90^\circ$ . The deviatoric strain at which the reversal happens is observed to decrease with increasing friction. On the other

hand, the orientation of the largest fabric eigenvector  $\theta_1^f$  shows a strong dependence on friction. For systems with low friction,  $\theta_1^f$  aligns with the compressive direction during loading while the configurations with high friction begin to align perpendicular to the axial direction as maximum deviatoric strain is approached.

The deviatoric strains at which the stress tensor changes, i.e.  $s_{\text{dev}} = 0$ ,  $\theta_1^s = 45^\circ$  and stress shape factor  $\Lambda^\sigma = 0$  (zero), are identical to each other and show a decreasing dependence on friction, with  $\varepsilon_{\text{dev}} \approx 0.01$  for  $\mu = 1$ . For quantities relating to the microstructure, e.g. the strain at which, e.g.,  $F_{\text{dev}} = 0$ , is different from the stress.

In comparison to other deformation protocols, we find while the coordination number is found to decrease with increasing triaxial loading (or increasing deviatoric strain) [15, 123], we find that the coordination number under increases with strain under uniaxial compression. Under triaxial loading, the number of contacts is found to increase in the the vertical (compression) direction while decreasing/dilating in the horizontal (fixed stress) direction [74]. In the uniaxial mode, the number of contacts is found to increase in both the horizontal and vertical directions. Also, the peak deviatoric fabric is found to increase with increasing friction under triaxial loading [15, 123]. In the uniaxial mode, the peak deviatoric fabric decreases with increasing friction.

As reported in previous studies [125], we also confirm that the orientation of the eigenvector of stress corresponding to the compression direction for strong (forces greater than average) and weak (forces less than average) contacts are orthogonal with respect to each other. As a consequence of the definition of the stress tensor, the effects of strong contacts are more dominant for stress. For fabric however, strong contacts are more dominant when friction is low while the weak contacts are found to play a bigger role for stronger friction, causing the qualitatively different behavior.

In terms of the proportion of contacts, we confirm that a larger proportion of the total contacts are weak while the proportion of sliding contacts out of the total contacts are less than 45%. More importantly, we find less than 50% weak sliding contacts with respect to the total number of weak contacts. On the other hand, the proportion of weak sliding contacts with respect to the total sliding contacts are significantly higher. The latter is in agreement with earlier studies that show that friction is more highly mobilized in weak contacts [147, 148].

As a consequence of the isotropic initial configuration, we find that the directional distribution of normal forces at the initial state are isotropic for all  $\mu$ . At maximum compression, we observe a higher mean, a lower peak and a wider tail of the force distribution in the compressive  $z$ -direction, while the distributions in the two lateral directions remain identical, narrower, with a shorter tail. Due to history, after uniaxial compression and tension, the initial states are not recovered when the original state,  $\varepsilon_{\text{dev}} = 0$  is reached. Forces are weaker and one has less contacts in the tensile  $z$ - direction.

We have also presented two averaging methods for the polar representation of contacts using the constant azimuthal and constant height methods. For our data, a second order tensor is insufficient to describe the structural anisotropy. We find a sixth order distribution with two peaks leading to three anisotropy state descriptors ( $\epsilon_2$ ,  $\epsilon_4$  and  $\epsilon_6$ ).

The second harmonic  $\epsilon_2$  is close to  $F_{dev}^s/\sqrt{3}$ , so that for different friction, the maximum  $\epsilon_2$  values behave in a similar fashion to the maximum deviatoric fabric. A second order tensorial descriptor is sufficient for the normal force but the tangential force and mobilized friction show a similar behavior to the contact distribution – requiring a higher order harmonic approximation due to the two strong peaks at  $\pi/4$  and the dip around  $\pi/2$ .

Future studies should concern exploring higher order tensors and the validity of the findings for other non-isotropic deformation modes (e.g. under simple and pure shear or triaxial tests). Furthermore, recent experiments [29] will allow to validate the present observations from DEM. The final goal is to develop constitutive models of particulate matter based on the microscopic insights gained.

## Appendix I: Averaging Methods

In this appendix, we describe the two averaging methods namely the constant azimuthal angle method (*b*) and the constant height method (*h*).

### 3.1 Constant azimuthal angle (bin width) method

Given the three normal unit vector components  $\hat{n}_x$ ,  $\hat{n}_y$ , and  $\hat{n}_z$  for each contact pair, to calculate the azimuthal angle, one needs the polar orientation  $\arccos(\hat{n}_z)$  of the normal unit vector in the direction relative to the active (axial) direction as schematically described in Fig. 3.18a. We average over the spherical azimuthal (vs. polar) ( $r, \varphi$ ) coordinate and then distribute the vectors, based on their orientation into bins of width  $\Delta\theta$ .

The fraction of contacts in a single bin is defined as  $\phi^\theta = C^\theta/C_{tot}$ , where  $C^\theta = \sum_{C \in b} 1$  and  $b \in [\theta - \Delta\theta/2; \theta + \Delta\theta/2]$ . Furthermore,  $\phi^\theta$  is normalized with the surface of the spherical annulus for each  $b$  by the factor  $\Delta\theta \sin \theta$  to yield the azimuthal contact probability density  $P(\theta) = (\phi^\theta/\Delta\theta \sin \theta)$  such that  $\int_0^\pi P(\theta) \sin \theta \Delta\theta = 1$ .<sup>2</sup> The polar distributions of the normal forces, tangential forces and mobilized friction are given respectively, by  $f_n(\theta) = (\sum_{C \in b} f_n)/(C^\theta)$ ,  $f_t(\theta) = (\sum_{C \in b} f_t)/(C^\theta)$  and  $\psi_f(\theta) = (\sum_{C \in b} (f_t/\mu f_n))/(C^\theta)$ , where the normalization with the number of contacts in each bin has been used.

<sup>2</sup>An alternative to the  $\Delta\theta \sin \theta$  normalization is a discrete formulation  $\cos \theta_f - \cos \theta_i$  where  $\theta_i = \theta - \Delta\theta/2$  and  $\theta_f = \theta + \Delta\theta/2$ .

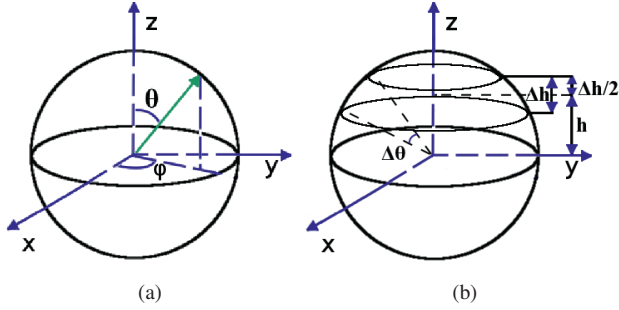


Figure 3.18: Schematic representation of the angles of the contact unit vector (green arrow) for (a) the constant bin width  $\Delta\theta$  method and (b) the constant height method. The angles  $\theta$  and  $\varphi$  are the azimuthal angle and polar angle of the system, respectively.

### 3.2 Constant height method

In the constant height method, we sort the vectors based on their orientations into  $n$  azimuthal spherical segments with equal heights  $\Delta h = \cos \theta_2 - \cos \theta_1$  as shown schematically in Fig 3.18b. Given the polar radius  $r$ , and the height from the center of each segment to the middle of the sphere  $h$ , the polar angle  $\theta$  of each vector is calculated for every  $\hat{n}_z \in h$ . The fraction of contacts within each segment range is then given as  $\phi^h = C^h / C_{tot}$ , where  $C^h = \sum_{C \in h} 1$  and  $h \in [h - \Delta h/2; h + \Delta h/2]$ . With  $-1 \leq h \leq 1$ , specifying the number of bins  $M_h$  (e.g.  $M_h = 20$ ), allows to compute all  $h$ -intervals and boundaries.

Other quantities, including the normal and tangential forces and mobilized friction can be computed similar to the constant bin width method, just by summation and normalization with  $C^h$  instead of  $C^\theta$ .

## Appendix II: Fit Methods

In the following, we describe different methods of obtaining the anisotropy state descriptors using the data obtained using the constant bin width or the constant height methods.

### 3.3 Method 1: Fit azimuthal contact probability density $P(\theta) = (\phi^\theta / \Delta\theta \sin \theta)$

In the first case, we fit the azimuthal contact probability density data  $P(\theta) = (\phi^\theta / \Delta\theta \sin \theta)$  using the harmonic equation (3.25). Note that for the special case of uniaxial compression, Eq. (3.24) does not lead to consistent results across the methods and is thus disregarded.

	Reference	Mode	Contact probability $P(\theta)$	Harmonic function
1.	Azema et al. [19]	triaxial	second order	$\frac{1}{4\pi}[1 + \epsilon(3\cos^2\theta - 1)]$
2.	Deng and Dave [35]	particle Settling in a cylindrical geometry	higher order	–
3.	Ishibashi et al [64]	triaxial	second order	$K(1 - \epsilon + 3\epsilon\cos^2\theta)$
4.	Jenkins [66]	triaxial	second order	$\frac{C}{4\pi}[(1 - \epsilon) + 3\epsilon\cos^2\theta]$
5.	Silbert et al. [146]	3D particle settling on a flat base	higher order	–
6.	Staron and Radjai [147]	2D avalanche	higher order	–

Table 3.4: Selected references on the orientational contact distribution for various modes. For an isotropic sample,  $K = C/4\pi$  and  $C$  is the coordination number.

However, as shown in different literature especially under triaxial compression, the second order approximation  $P_2(\theta)$  is sufficient to fully capture the contact probability density data. Exemplary (not exhaustive) references of works where forms of Eq. (3.24) as applied to various triaxial tests are presented in table 3.4. Other experimental and numerical set-ups are also shown. Note that in these cases, the orientational contact distribution obtained is not of second order and are not fitted.

### 3.4 Method 2: Fit to the constant height data

In the second case, we directly fit the fraction of contacts  $\phi^h$ , generated using the constant height method such that the bad statistics at the poles are not over-exposed as in Method 1. In this case, we set the zero order parameter  $a_0 = 0.5$ .

### 3.5 Method 3: Fit to fraction of contacts $\phi^\theta$ with a $\Delta\theta \sin\theta$ scaling

In the third case, we fit the fraction of contacts  $\phi^\theta$  data directly using harmonic equation (3.24) or (3.25) multiplied by  $\Delta\theta \sin\theta$ . The original signal is a first order sinus, i.e. less weighting is given to the areas close to the poles such that their larger statistical errors are

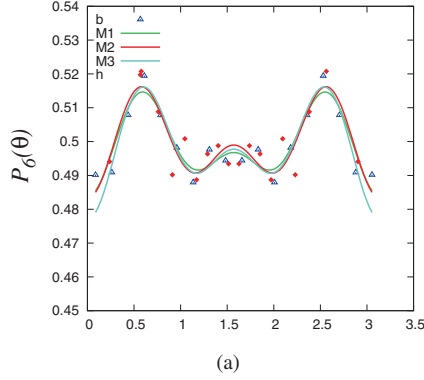


Figure 3.19: 6th Order Fits of methods 1 and 2 and 3 to the  $P(\theta) = (\phi^\theta / \Delta\theta \sin\theta)$  data at dimensionless time  $\tau = 0.076$ . The solid red symbols represent data obtained using the constant height method ( $h$ ), while the triangles are those obtained with the constant bin width method ( $b$ ).

suppressed.

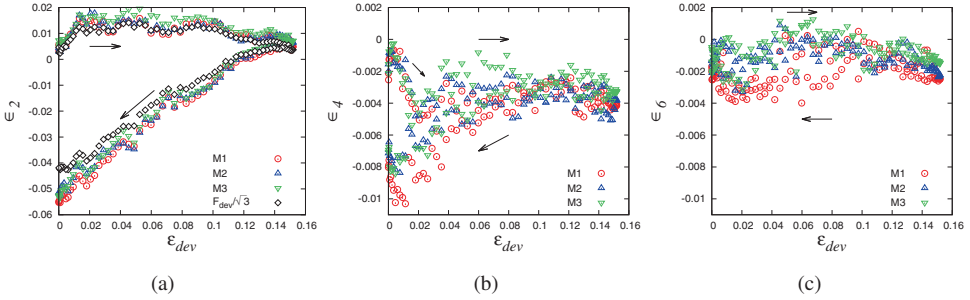


Figure 3.20: Evolution of the anisotropy state descriptors  $\epsilon_2$ ,  $\epsilon_4$  and  $\epsilon_6$  of the 6th order expansion Eq. (3.25) as function of deviatoric strain using the three methods for  $\mu = 0$ .

In Fig. 3.19, we show the sixth order harmonic fits using methods 1 (M1), 2 (M2) and 3 (M3) to the constant bin width ( $b$ ) and constant height ( $h$ ) data for  $\mu = 0$ . For each method, three anisotropy state descriptors, namely  $\epsilon_2$ ,  $\epsilon_4$  and  $\epsilon_6$  are obtained. Here, as an example, we show a single snapshot, namely at  $\tau = 0.076$ . Note that the original data is from 0 to  $\pi/2$  and the extension from  $\pi/2$  to  $\pi$  is only a mirror image. Focusing on the numerical data (symbols), we observe two strong peaks at about  $\pi/2 \pm \pi/4$  and a local maximum at  $\pi/2$ . The twin peaks indicate that a distribution higher than second order is needed. The data are well captured by a sixth order approximation  $P_6(\theta)$  (solid lines). Comparing the  $b$  and  $h$ , we observe stronger scatter at the boundaries for the  $b$  data due to the weak statistics at the extreme  $\theta$  values (0 and  $\pi$ ). For the fits, we observe that M1, M2 and M3 are close and the



major differences between them are most pronounced at both peaks and extrema.

In Fig. 3.20, we plot the evolution of the anisotropy state descriptors  $\epsilon_2$ ,  $\epsilon_4$  and  $\epsilon_6$  as functions of the deviatoric strain and compare the three methods. From Fig. 3.20a, during loading,  $\epsilon_2$  grows and reaches a maximum at  $\epsilon_{\text{dev}} \approx 0.025$  from where it slightly decreases. After maximum loading,  $\epsilon_2$  decreases (taking well into account the sign change) and becomes increasingly negative until it reaches  $\epsilon_2 \approx -0.055$  at complete unloading ( $\tau=1$ ). Comparing the three methods, M3 is slightly off (higher) during loading while M1 is also slightly off at the end of unloading. Interestingly, we find that the evolution of  $\epsilon_2$  is similar to the simple definition of the deviatoric fabric in Eq. (3.19) involving a difference between the fabric component of the axial direction and the average of the components of the two lateral components. Note that the definition of the fabric used here is based on Eq. (3.16) which considers only the contacts and not the dependence on the volume fraction. We note that the magnitude of  $\epsilon_2$  is proportional to  $F_{\text{dev}}/\sqrt{3}$  (black diamonds in Fig. 3.20a) with M3 slightly off during loading and the unloading data also showing slight variations. From Fig. 3.20b and 3.20c, the values of  $\epsilon_4$  and  $\epsilon_6$  appear small compared to  $\epsilon_2$  but must not be neglected. When  $\epsilon_2$  is taken as the structural anisotropy state descriptor, it much resembles  $F_{\text{dev}}$ . However, the higher order anisotropy is quantified by the  $\epsilon_4$  (which is negative) and  $\epsilon_6$  (which is strongly fluctuating and different for different methods).

## Chapter 4

# Slow relaxation behaviour of cohesive powders\*

### Abstract

*We present findings from uniaxial (oedometric) compression tests on cohesive granular materials. Experimental results are presented for the compressibility, tested with two devices, the FT4 Powder Rheometer and the custom made lambdameter. We focus on the stress response and the slow relaxation behavior of the cohesive samples tested. After compression, at constant volume, the decrease in stress is found to follow a power law for cohesive powders, consistently for the different testing equipments. A simple model is proposed for stress relaxation in cohesive powders, which accounts for the change of force and includes a response timescale along with a second, dimensionless stress relaxation parameter. The reported observations will be useful for both the improvement of discrete element simulations and constitutive macroscopic models relating to cohesive granular materials.*

---

\*Based on O. I. Imole, M. Paulick, M. Morgeneuer, V. Magnanimo, E. C. Montes, M. Ramaioli, A. Kwade, and S. Luding. An experimental and theoretical investigation of the time-dependent relaxation behavior of cohesive powders. *In preparation*, 2014

## 4.1 Introduction and Background

Granular materials are omnipresent in nature and widely used in various industries ranging from food, pharmaceutical, agriculture and mining – among others. In many granular systems, interesting phenomena like dilatancy, anisotropy, shear-band localization, history-dependence, jamming and yield have attracted significant scientific interest over the past decade [10, 62, 92]. The bulk behavior of these materials depends on the behavior of their constituents (particles) interacting through contact forces. To understand their deformation behavior, various laboratory element tests can be performed [111, 140]. Element tests are (ideally homogeneous) macroscopic tests in which one can control the stress and/or strain path. Such macroscopic experiments are important ingredients in developing and calibrating constitutive relations and they complement numerical investigations of the behavior of granular materials, e.g. with the discrete element method [92]. Different element test experiments on packings of bulk solids have been realized experimentally in the biaxial box [112, 113, 130] while other deformations modes, namely uniaxial and volume conserving shear have also been reported [122, 131, 177]. Additionally, element tests with more complex, non-commercial testers have been reported in literature [22, 54, 56, 65], even though their applications are restricted for example to the testing of non-industrially relevant materials at very high consolidating stresses.

The testing and characterization of dry, non-sticky powders is well established. For example, rotating drum experiments to determine the dynamic angle of repose have been studied extensively as a means to characterize non-cohesive powders [24, 31, 127]. The main challenge comes when the powders are sticky, cohesive and less flowable like those relevant in the food industry. For these powders, dynamic tests are difficult to perform due to contact adhesion and clump formation. One possibility to overcome this challenge is to perform confined quasi-static tests at higher consolidation stresses.

One element test which can easily be realized (experimentally or numerically) is the uniaxial (or oedometric) compression (in a cylindrical or box geometry) involving deformation of a bulk sample in one direction, while the lateral boundaries of the system are fixed [21, 60, 62, 63]. This test is particularly suited for determining the poroelastic properties of granular materials. While most uniaxial tests on dry bulk solids have been devoted to studying the relationship between pressure and density and the bulk long time consolidation behavior, the dynamics of the time-dependent phenomena has been less studied in experimental and practical applications [179]. For example, in standard shear testers like the Jenike shear tester [70] and the Schulze shear tester [137], during yield stress measurements, the focus is usually not on the relaxation behavior. Considerable stress-relaxation of bulk materials can even disturb yield stress measurements. Additionally, most cohesive contact models [92, 161, 163, 168] used in discrete element simulation of granular materials do not account for the time dependent relaxation behavior, similar to those observed in viscoelastic materials

such as polymers [44, 46, 110], gels [32, 174], in dielectric relaxation [68, 69] and in the attenuation of seismic waves [71]. For the improvement of both discrete element contact models and constitutive macro models relating to cohesive powders, it is necessary to have an experimental and theoretical understanding of the stress response of cohesive materials under different loading conditions. The creep-like response at constant strain is the focus of this study.

For viscoelastic materials, the relaxation has been reported to imply a memory effect and can be described using convolution integrals transformed to their fractional form and containing a relaxation modulus that describes the response of the system to stress [135]. For these materials, phenomenological models involving the combination of springs and dashpots, such as the Maxwell, Zener, anti-Zener, Kelvin-Voigt, and the Poynting-Thomson models have been developed (see Refs. [16, 20, 73, 103] and references therein). Even though stress relaxation has also been observed in granular media [21, 137, 179], not much work has been done in providing a theoretical description of this phenomenon for granular materials.

In the present study, using two simple testers, we perform oedometric compression tests with the main goal of investigating the relaxation behavior of industrial powders at different stress levels under constant strain (volume). Another goal is to provide a quantitative comparison between the relaxation behavior as observed in two testers, namely the lambdameter and the FT4 Rheometer, in order to confirm that this behavior occurs irrespective of the device used. The lambdameter has the peculiar advantage that *both* vertical and horizontal stress can be obtained simultaneously – unlike the FT4 Rheometer and other simpler oedometric test setups. Finally, we will propose a simple model for stress relaxation that captures the relaxation of cohesive powders at different compaction levels.

The work is structured as follows. In section 4.2, we provide a characterization of the material sample, and in section 4.3 the description of the experimental devices and the test protocol. In section 4.4, we present the theoretical model for stress relaxation. Section 4.5 is devoted to the discussion of experimental and theoretical results, while the conclusions and outlook are presented in section 4.6.

## 4.2 Sample Description and Material Characterization

In this section, we provide a brief description of the experimental samples along with their material properties. In order to investigate the relaxation behavior, two cohesive reference samples were chosen, namely cocoa powder and Eskal 500 limestone. The choice can be based on several selection factors, among which are the suitability for different industrial applications, ability to withstand repeated loading without changes in the property of the sample and long term availability/storage of the samples. The Eskal limestone has been used

extensively as reference cohesive powder, and is made available in convenient amounts in a collaborative European project [154] and [www.pardem.eu](http://www.pardem.eu). Scanning Electron Microscope (SEM) images obtained using a Hitachi TM 1000 Instrument (Hitachi Ltd, Japan) for both powders are displayed in Fig. 4.1.

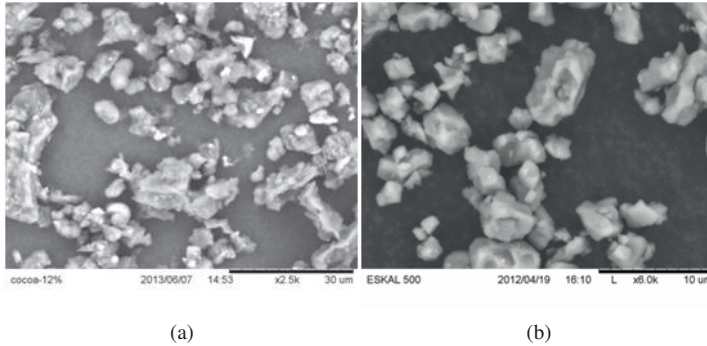


Figure 4.1: Scanning electron microscope images of the cohesive samples (a) Cocoa with 12% fat content (b) Eskal 500 limestone powder. Note the different scales at the bottom right.

The particle size distributions and specific surface area are measured by the dry dispersion module of the Malvern Mastersizer (Malvern Instruments Ltd., UK) while the particle density is measured by helium pycnometry (Accupyc, Micromeritics, USA). The water uptake is given as the ratio of the difference between the original and dried mass (after 24 hours in a oven at 100°C) and the original sample mass. The bulk cohesion is the limiting value of shear stress for which the normal stress is equal to zero and is determined from shear experiments with a ring shear tester (RST-01.pc by Dietmar Schulze Schüttgutmesstechnik, Germany).

A more specific description of the experimental samples are provided in the following section.

### 4.2.1 Cocoa Powder

One cohesive sample used in this work is cocoa powder with 12% fat content - which is a representative sample for the material used as basic ingredient in the production of chocolate and related beverages. The material properties including size distribution, particle density and moisture content are shown in Table 4.1 along with a scanning electron microscope visualization of its morphology in Fig. 4.1a. We note that even though the powder is relatively hygroscopic, its humidity does not change significantly during the experiments. Additionally, the experiments were performed over a relatively short period under ambient conditions

Property	Unit	Cocoa(12%)	Limestone	
Size distribution	$D_{10}$	$\mu\text{m}$	2.14	1.34
	$D_{50}$	$\mu\text{m}$	9.01	4.37
	$D_{90}$	$\mu\text{m}$	37.40	8.24
Particle Density		[ $\text{kg}/\text{m}^3$ ]	1509	2710
Water absorption		%	< 15%	< 0.2%
Cohesion (as function of vertical stress)	$\sigma_c$	kPa	1.8 at 7.4 kPa	1.3 at 4.6 kPa
			9.6 at 41.8 kPa	3.3 at 12.7 kPa

Table 4.1: Material parameters of the experimental samples. Water absorption and cohesion are defined in the main text.

and samples are sealed in air-tight bags when not in use to minimize effects that could arise due to changes in the product humidity.

#### 4.2.2 Eskal 500 Limestone

The other industrial sample powder used in this work is Eskal 500 limestone powder (KSL Staubtechnik, Germany). Eskal 500 limestone is a commercially available powder that has wide applications in architecture, road construction, blast furnaces, medicines and cosmetics. It is also considered a suitable reference material for calibration, measurements and standard testing [42, 179]. One advantage of this material over other grades is its inability to absorb humidity from air. During long term storage under stress, Eskal 500 limestone shows no degradation as confirmed by repeatable results from experiments carried out under different conditions. The material properties and SEM morphology are shown in Table 4.1 and Fig. 4.1b.

Comparing the physical features of the powders, cocoa powder is brownish while Eskal 500 is whitish in color. Secondly, while cocoa powder contains some 12% fat, Eskal 500 limestone does not. As we will see shortly, this distinction is important for a comparison of their relaxation behavior.

### 4.3 Experimental Set-up

In this section, we describe the Lambdameter and FT4 Powder Rheometer along with the protocols used in performing the tests.

### 4.3.1 FT4 Powder Rheometer

The first experimental equipment used in this work is the FT4 powder rheometer (Freeman technology Ltd. UK), illustrated in Fig. 4.2a. Standard accessories for the compressibility test include the 50mm diameter blade for conditioning, the vented piston for compression and the 50mm height by 50mm diameter borosilicate test vessel. One advantage of the commercial FT4 rheometer is the automated nature of the test procedure requiring minimal operator intervention.

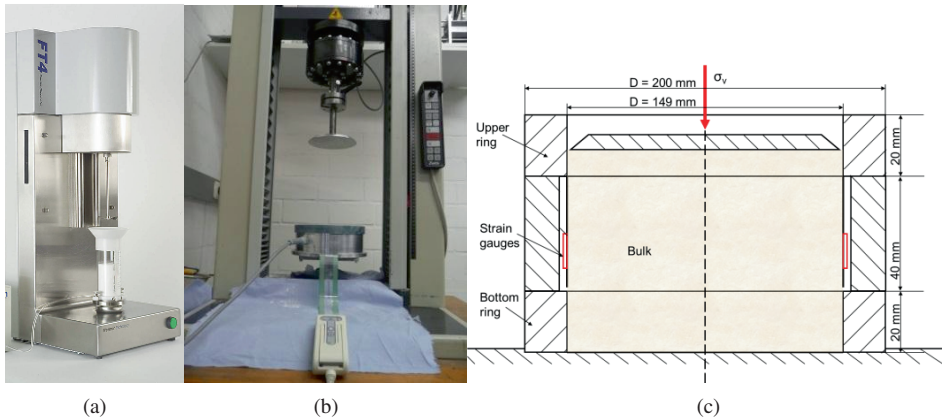


Figure 4.2: (a) The FT4 Powder Rheometer and (b) The Lambdameter apparatus used for the experimental tests. (c) A schematic representation of the Lambdameter test set-up.

The compression test sequence is as follows. The sample is placed in the test vessel (see Fig. 4.3a) after the tare weight of the vessel has been obtained. The weight of the powder is measured and the conditioning cycle is initiated. The conditioning procedure involves the gentle movement of the conditioning blade into the test sample to gently disturb the powder bed for a user pre-defined number of cycles. This action creates a uniform, lightly packed test sample that can be readily reproduced. In this study, we allow three pre-conditioning cycles before the uniaxial compression tests are carried out. Subsequently, the blade is replaced with a vented piston, which incorporates a stainless steel mesh to allow the entrained air in the powder to escape uniformly across the surface of the powder bed. The vessel assembly is split (or leveled) to provide precise volume measurement and the powder mass is recalculated after splitting. The compression test then begins with the distance travelled by the piston measured for each applied normal stress.

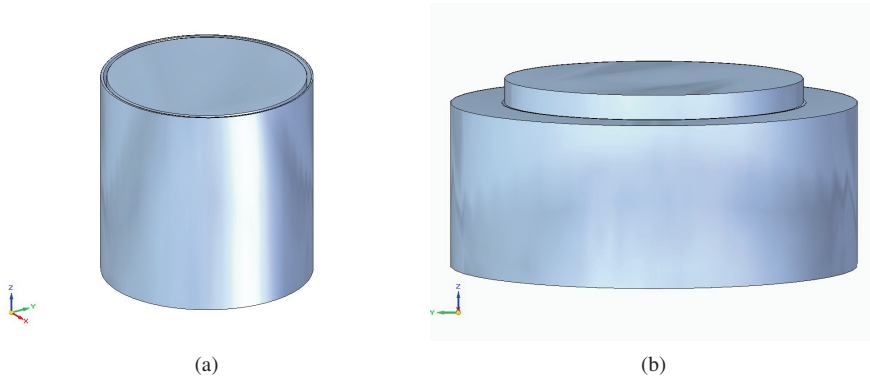


Figure 4.3: Schematic representation showing the difference in the cell design of (a) the FT4 Rheometer with aspect ratio  $\alpha = 1$  and (b) the lambdameter with  $\alpha = 0.4$ .

### 4.3.2 The Lambdameter

The custom made lambdameter represents a horizontal slice of a silo and is primarily used in obtaining the lateral stress ratio [82–84] – one of the most important parameters in the calculation of stress distributions in silos for reliable design [139, 140]. The lambdameter used was designed at the Institute of Particle Technology (iPAT), Technical University of Braunschweig and is shown schematically in Fig. 4.2b and 4.2c. The lambdameter measures the vertical (axial) and horizontal (radial) stress of a powder under compaction. The horizontal stress is measured through the installation of pressure cells along the periphery of the cylindrical mould. The measuring ring of the Lambdameter is made from stainless steel with a very smooth surface and the dimensions are listed in Table 4.2. To allow for the automation of the compression test, similar to that of the FT4, the lambdameter set-up is installed into a Zwick Z010 (Zwick/Roell, Zwick GmbH & Co. KG, Germany) uniaxial testing device as shown in Fig. 4.2b.

The experimental procedure is as follows. The experimental sample is first sieved to prevent formation and a funnel is used to channel the sample into the cylindrical mould (see Fig. 4.3b) until it is completely full. Using a smooth object, excess material is removed without allowing for a compaction of the sample in the mould. Next, the top plate (1.48kg) and the top hanger (2.68kg) are carefully placed on the mould. Subsequently, additional weights are carefully placed on the hanger in successive steps until the target pressure is reached. The horizontal and vertical stresses along with the position of the top punch at a given time are recorded with a data logger on a computer connected to the experimental set-up.

A detailed comparison between the main features of both testers is shown in Table 4.2. We only note that the FT4 is more automated and requires less human intervention compared



Property	FT4 Rheometer	Lambdameter
Cell volume	$8.5 \times 10^{-5} \text{ m}^3$	$1.046 \times 10^{-3} \text{ m}^3$
Cell shape	cylindrical	cylindrical
Area (diameter (D) $\times$ height (H))	$0.05\text{m} \times 0.05 \text{ m}$	$0.149 \text{ m} \times 0.06 \text{ m}$
Aspect ratio $\alpha = H/D$	1	0.40
Driving mode	Motor control	Automated
Test control	Built in test program on PC	Labview
Sample Weighting	on-board	offline
Compression device	vented piston	dead weights
Driving velocity	variable	variable
Maximum stress	22kPa	69.96kPa
Sample pre-conditioning	Automatic	Manual
Test duration	variable	variable
Stress measurement (direction)	vertical stress	horizontal and vertical stress

Table 4.2: Comparison of the FT4 rheometer and the lambdameter specifications.

to the Lambdameter. On the other hand, in contrast to the FT4 Rheometer, higher volumetric strains and axial stresses can be reached with the Lambdameter. Additionally, the lambdameter also provides for the measurement of the horizontal (lateral) stress.

### 4.3.3 Test Protocols

In order to investigate the relaxation behavior of the different experimental samples under uniaxial loading, different staged test protocols are employed, see Table 4.3. The uniaxial loading is done in steps of 5kPa with intermediate relaxation between each step. The maximum stress reached for experiments with the FT4 Rheometer is 22kPa while for the Lambdameter, we reach a higher maximum stress of 25kPa. We performed more extensive experiments with the Lambdameter set-up due to its versatility in terms of the maximum stress reached and the horizontal stress measurement. We compare in some cases the stress-relaxation behavior under uniaxial loading for both equipments.

In general, we study the effects of strain rate, relaxation time duration, and the stress at which the relaxation is initiated along the loading path. We measure the vertical stress as function of the volumetric strain i.e. vertical strain since we are in an oedometric set-up.

protocols	Velocity [mm/s]	No. of steps	Vertical stress [kPa]	Relaxation time [mins]	FT4	Lambda- meter
Protocol 1	0.05	5	5 - 10 - 15 - 20 - 25	5	x	x
Protocol 2	0.05	5	5 - 10 - 15 - 20 - 25	10		x
Protocol 3	0.05	5	5 - 10 - 15 - 20 - 25	20		x
Protocol 4	0.05	5	5 - 10 - 15 - 20 - 25	30		x
Protocol 5	0.01	5	5 - 10 - 15 - 20 - 25	10	x	x
Protocol 6	0.3	5	5 - 10 - 15 - 20 - 25	10		x
Protocol 7	0.7	5	5 - 10 - 15 - 20 - 25	10		x
Protocol 8	1.0	5	5 - 10 - 15 - 20 - 25	10		x
Protocol 9	1.3	5	5 - 10 - 15 - 20 - 25	10		x

Table 4.3: Table of experimental protocols performed. Note that for experiments with the FT4 Rheometer, the maximum stress reached is 22kPa. Protocols 1–4 represent a variation of the relaxation time, while 5–9 are different compression rates. Crosses indicate the device used in performing the experiment.

## 4.4 Stress Relaxation Theory

Assuming a force  $f = \sigma_v A$  that acts on the top plate under uniaxial loading, the change of force  $f$  should be stronger for stronger applied force due to a micro- or nano-scopic or change of the contact structure. The model evolution relation is:

$$\frac{\partial}{\partial t} f = -\frac{C}{t_0 + t} f, \quad (4.1)$$

where  $C$  is a dimensionless proportionality constant and  $t_0$  is a typical response time. The time in the denominator on the r.h.s. accounts for the fact that the change of force decays with time (extremely) slowly. For organic materials like coffee and cocoa, the initial grains contain liquid and solid ingredients. Due to a strong force, the liquid is squeezed out of the solid matrix – locally at the contact during deformation. The terminal state would be a state where all liquid content has been squeezed out, however, since pores exist on many scales, this can take extremely long, i.e. much longer than the experiments presented here.

The change of force is also proportional to the force itself, since at zero force, there is no reason to assume further force changes. The constant  $C$  determines the magnitude of the force change and contains information about the microscopic constitution of the material. Hard materials with low liquid content are described by large  $C$  values, whereas soft materials with high liquid content correspond to small  $C$  values.

Assuming that the force is raised from zero to a value  $f^{\max}$  instantaneously the response of the system is then given by the solution of the above equation with initial force  $f^{\max}$  and starting from time  $t=0$ , so that:

$$\ln\left(\frac{f}{f^{\max}}\right) = \int_{f^{\max}}^f \frac{\partial f'}{f'} = \int_0^t -\frac{C}{t_0+t'} \partial t' = -C \ln(t_0+t) + C \ln t_0 = \ln\left(\frac{t_0+t}{t_0}\right)^{-C} \quad (4.2)$$

which can be further simplified to:

$$1 - \frac{f}{f^{\max}} = 1 - \left(\frac{t_0+t}{t_0}\right)^{-C} = 1 - \left(1 + \frac{t}{t_0}\right)^{-C} \quad (4.3)$$

In the next section, the simple model presented above will be compared to experimental data and the response time  $t_0$  and parameter  $C$  will be analyzed.

## 4.5 Results and Discussion

In this section, as one result of the current study, we will first compare the uniaxial compression and relaxation experiments carried out with the FT4 Rheometer and Lambdameter. To complement these results, we also compare the relaxation behavior of the different cohesive powders using the Lambdameter set-up. Finally, we investigate the effects of strain-rate, loading steps and relaxation time on the decay of the stress at constant strain.

### 4.5.1 Testing Equipments - A Comparison

A comparison of testers is necessary for several reasons. Apart from the fact that several literatures have reported on comparative studies between different testers used in the characterization of cohesive powders [65, 70, 154], most differences observed have been attributable to human errors, differences in the filling procedure and the measurement conditions. For our experiments, it is important to confirm that the relaxation feature can be reproduced in different testers and not due to drift or bias in our testing equipments. The material used here is cocoa powder.

In order to compare the response of the two testing equipments to vertical (axial) stress, we perform uniaxial compression test on cocoa powder with a carriage speed on 0.05mm/s (protocol 1 in Table 4.3). Five intermediate relaxation stages (R1–R5)<sup>1</sup>, in which the top

<sup>1</sup>Due to the difference in the final stress reached at R5 in the FT4 (22kPa) and lambdameter (25kPa), the final relaxation R5 for both equipments should be compared with caution.

piston/punch is held in position for 300 seconds at specific intervals of 5kPa during the compression tests were included. In Fig. 4.4a we plot the vertical stress  $\sigma_v$  as function of time. During loading, the axial stress builds up with time until the first target stress of 5kPa (at R1) is reached. We observe a slower increase of the axial stress in the Lambdameter in comparison to the Rheometer even though the respective pistons were moved with the same carriage speed. This is possibly due to the difference in masses of the powders and volume as well as aspect ratio of the experimental moulds for both equipments, leading to different initial densities of the same sample, and consequently different response to compressive stress.

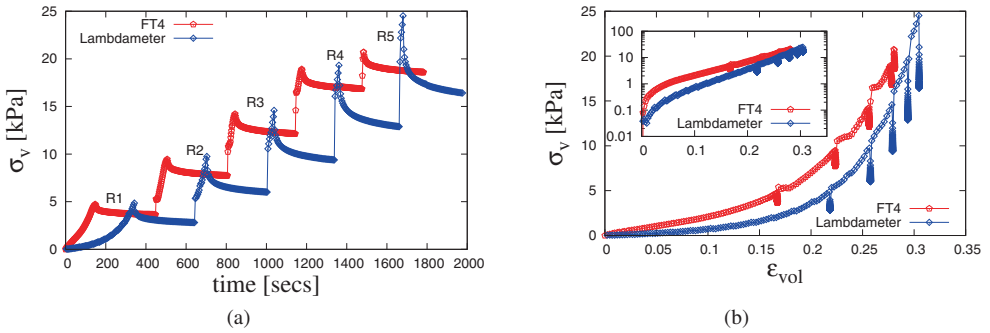


Figure 4.4: Comparison of the vertical (axial) stress plotted against (a) time (b) volumetric strain for experiments with cocoa powder using the FT4 Rheometer and the Lambdameter. The carriage velocity is 0.05mm/s while R1–R5 represent the intermediate relaxations for increasing target stress.

With the initiation of the first relaxation R1 at 5kPa, we observe for both equipments a time-dependent stress decrease for a relaxation time of 300 seconds. This observation, along with other observations reported in literature for other granular materials [137, 179] confirms that the stress decrease is not due to a drift in the measuring equipments but it is a feature. From 5kPa, we observe an approximate 45 percent decrease in stress for the lambdameter compression compared to the 22 percent in the Rheometer. With the activation of axial compression after the relaxation, we observe a sharp increase in the axial stress until the next intermediate stress state is reached. This sudden jump is similar to that observed in stick/slip [137, 143] experiments and friction between solid bodies [36] where a sudden increase in shear velocity results in a sharp increase in shear stress. The same feature is reproduced for the higher stress states.

An objective comparison of the stress-strain evolution in both testing equipments is presented in Fig. 4.4b, where the vertical stress is plotted against volumetric strain. The volumetric strain is defined here as  $(L - L_0)/L_0$  where  $L$  and  $L_0$  are the final and initial piston positions, respectively. We observe that the lambdameter produces a softer response to the applied

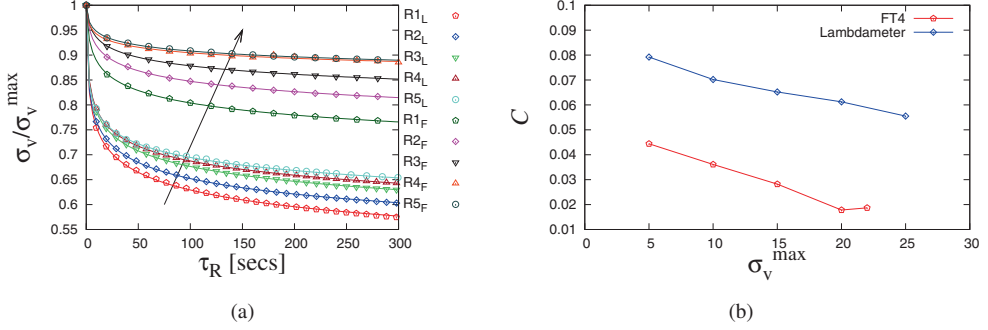


Figure 4.5: Relaxation at different stress levels R1–R5 during the uniaxial compression of cocoa powder in Fig. 4.4. The subscripts F and L represent data from the FT4 and Lambdameter experiments respectively. The symbols represent the experimental data while the solid lines represent the theoretical fit using Eq. (4.3) with parameters listed in Table 5.2.(b) Evolution of the dimensionless  $C$  parameter of Eq. (4.3) with intermediate maximum stresses  $\sigma_v^{\max}$  for the two equipments.

stress, as evidenced by the slower increase in the vertical stress during loading. The same intermediate target stresses are reached at a higher strain in the lambdameter as compared to the FT4 Rheometer. Secondly, the decrease in stress occurs at constant strain as shown by the vertical drops along the deformation path.

Next, we turn our attention to the relaxation stages and extract the data for the steps R1–R5 in Fig. 4.5a. For clarity, R1 is termed the first relaxation occurring at 5kPa while while R5 is the final relaxation at 25kPa (or 22kPa for the FT4). The vertical stresses have been normalized by their initial values before relaxation while  $\tau_R$  is the relaxation time which in this case is 300 secs. Note that even though the data output was at 50Hz, we show only points at intervals of  $\approx 20$ Hz to allow for a clear visualization of the relaxation process. In general, we observe stronger relaxation amplitudes in the lambdameter tests. Most notably, the lambdameter relaxation occurring at the highest stress of 25kPa ( $R5_L$ ) shows even stronger relaxation than the first relaxation ( $R1_F$ ) observed in the rheometer. Interestingly, the stress relaxation law proposed in Eq. (4.3) describes well the relaxation in both equipments at all stress states after the stress in each state has been normalized by its maximum value  $f^{\max}$  such that  $f^* = \sigma_v / \sigma_v^{\max} = f / f^{\max}$  has a maximum value of 1. The maximum intermediate stress reached along with the other parameters are displayed in Table 5.2. Comparing the parameters of the model, we observe that the response time  $t_0$  fluctuates with increasing stress from R1–R5 and is higher for relaxations with the FT4 than with the lambdameter. On the other hand, the parameter  $C$  also plotted in Fig. 4.5b shows a decreasing trend, its magnitude being smaller for the FT4. This is possibly due to both different geometries (see Fig. 4.3) and ongoing, reduced relaxation as the material becomes more and more compressed. The FT4 is much

Step	$\sigma_L^{\max}$	$t_{0L}$	$C_L$	$\sigma_F^{\max}$	$t_{0F}$	$C_F$
R1	4.89649	0.2894	0.0792	4.75	0.7462	0.0444
R2	9.96843	0.2274	0.0702	9.5	1.0308	0.0361
R3	14.913	0.2502	0.06521	14.25	1.0227	0.0282
R4	20.0375	0.2207	0.06124	19.01	0.3614	0.0178
R5	25.0718	0.1422	0.0555	20.9	0.5809	0.0187
error [%]	–	0–3	0–0.4	–	0–5	0–1

Table 4.4: Fit parameters for the analytical predictions of the relaxation model Eq. (4.3). The subscripts  $L$  and  $F$  represent data from the Lambdameter and FT4 Rheometer, respectively while R1–R5 are the relaxation steps.

narrower and thus a strong effect of the side walls is expected. A study of the influence of aspect ratio is ongoing.

#### 4.5.2 Relaxation of Two Powders - A Comparison

As a second step, in order to compare the response of different cohesive powders, we introduce the second powder (Eskal 500) and repeat the same protocol as described in section 4.5.1. For the sake of brevity, the comparison is done using only the lambdameter set-up.

In Fig. 4.6a, we show the time evolution of stress during compression for cocoa powder and Eskal 500 limestone. Both powders show qualitatively identical relaxation behavior under applied stress. Comparing the stress-strain response in both testing equipments as presented in Fig. 4.6b, we observe a similar stress-strain response for both materials within the small strain region ( $\epsilon_{\text{vol}} < 0.15$ ). However at larger strains, the response diverges and limestone responds softer to strain, evidenced by the slower increase in vertical stress. Secondly, we confirm that the decrease in stress at R1–R5 occurs at constant strain as shown by the vertical drops along the deformation path. For the same intermediate stress, the onset of the relaxation occurs at a higher strain in limestone as in cocoa.

In Fig. 4.7a, we extract the relaxation phases of the experiments shown in Fig. 4.6 Eskal (E) and cocoa (C) and plot them against the relaxation time. We observe that at the same stress and using the same driving velocity, cocoa powder relaxes more and much faster than the Eskal limestone. For example, the relaxation under the lowest compressive stress (R1), shows a 33 percent decrease in stress for Eskal compared to a 43 percent decrease for cocoa. This is possibly arising from the fat content present in the cocoa powder and absent in Eskal 500 limestone.

The fit parameters of Eq. (4.3) are shown in Table 5.3 for the five relaxation data shown

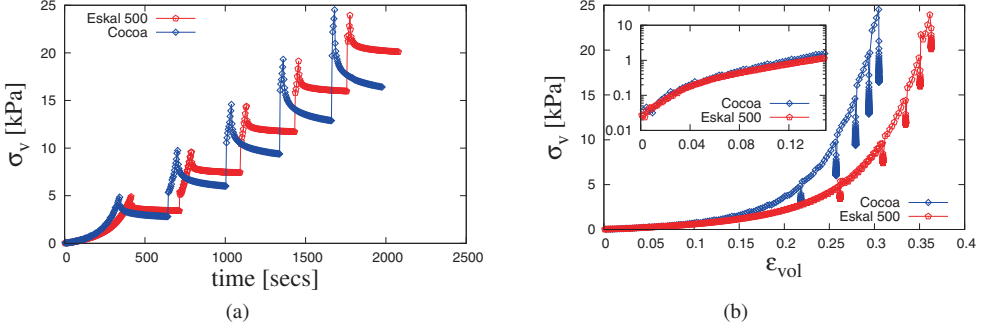


Figure 4.6: Comparison of the vertical (axial) stress plotted against (a) time (b) volumetric strain for experiments with cocoa powder and Eskal 500 limestone. Experiments carried out using the Lambdameter with carriage velocity is 0.05mm/s while R1–R5 represent the intermediate relaxations during loading.

Step	$\sigma_C^{\max}$	$t_{0C}$	$C_C$	$\sigma_E^{\max}$	$t_{0E}$	$C_E$
R1	4.8964	0.28945	0.0792	5.0027	0.00082	0.0300
R2	9.9684	0.2274	0.0702	10.0246	0.00046	0.0227
R3	14.9130	0.2503	0.0652	15.0648	0.00032	0.0184
R4	20.0375	0.2207	0.0612	20.0004	0.00021	0.0160
R5	25.0718	0.1422	0.0556	25.0253	0.00032	0.0159
error[%]	–	0–3	0–0.4	–	3–7	0–1.3

Table 4.5: Fit parameters for the analytical predictions of the relaxation model Eq. (4.3). The subscripts  $C$  and  $E$  represent data for cocoa and Eskal, respectively, while R1–R5 are the relaxation steps.

for each powder in Fig. 4.7a, limestone and cocoa. For each powder, the response time  $t_0$  and dimensionless parameter  $C$  generally shows a decreasing trend with the maximum stress at which the relaxation is initiated. The decreasing trend of both parameters  $t_0$  and  $C$  is confirmed also for Eskal 500, however, the time-scale is orders of magnitude smaller while  $C$  is of the same order only about a factor of two smaller, as summarized in table 5.3 and plotted in Fig. 4.7b.

In summary, for both powders, we conclude that even though both Eskal and Cocoa powder show qualitatively similar relaxation at constant strain, their individual magnitudes and responses are quantitatively dissimilar at different intermediate stress.

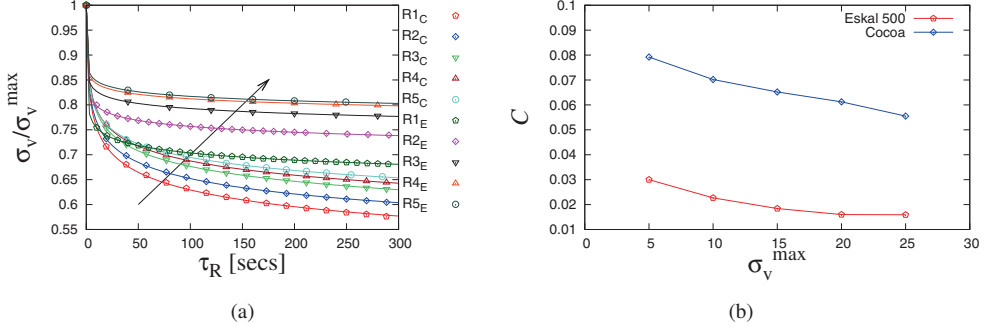


Figure 4.7: (a) Extract of the 5 relaxation steps R1–R5 for both experimental specimens in Fig. 4.6. The subscripts E and C represent data from experiments with Eskal 500 (E) and Cocoa (C), respectively. The symbols represent the experimental data while the solid lines represent the analytical Eq. (4.3) (b) Evolution of the dimensionless  $C$  parameter of Eq. (4.3) with intermediate maximum stresses  $\sigma_v^{\max}$  for the two powders.

### 4.5.3 Effect of Relaxation Duration

In order to compare the changes in the vertical stress drop due to the relaxation duration, using the Lambdameter, we perform several experiments in which the waiting (relaxation) time is varied between 5 minutes and 30 minutes during the different relaxation phases (protocols 1–4 in Table 4.3). Thereafter, we compare the stress states achieved from different levels after the same relaxation for  $\tau = 5$  minutes (300 s), to highlight the effect of (previous) history where the powders with larger  $\tau_R$  relaxed longer.

In Fig. 4.8, we plot the relative stress reduction,  $1 - (\sigma_v(\tau = 5\text{mins})/\sigma_v^{\max})$  as function of the maximum intermediate stresses  $\sigma_v^{\max}$  for different previous relaxation times  $\tau_R$ . We observe that increasing the relaxation time at the lowest stress of 5kPa does not lead to any visible change in the stress reached, as evidenced by the collapse of the data at  $1 - (\sigma_v(\tau)/\sigma_v^{\max}) \approx 0.32$ . It is important to note that this is the first relaxation stage, hence there is no effect yet of the loading history (different  $\tau_R$ ) of the bulk sample at this stage. This also confirms the repeatability of our measurements.

For subsequent relaxations at higher stresses (10, 15, 20 and 25kPa), the difference due to the longer previous waiting times becomes visible. We observe a consistent pattern at all stresses where an increase in relaxation time  $\tau_R$  results in lower relative stress reduction. This is an indication that the effects of previously experienced longer relaxation kicks in at higher stresses, i.e. the loading history becomes important so that longer previous loading reduces the possible relaxation in the present state. Another interesting observation is the similarity in the span of the difference from the 5 mins relaxation to the 30 mins relaxation



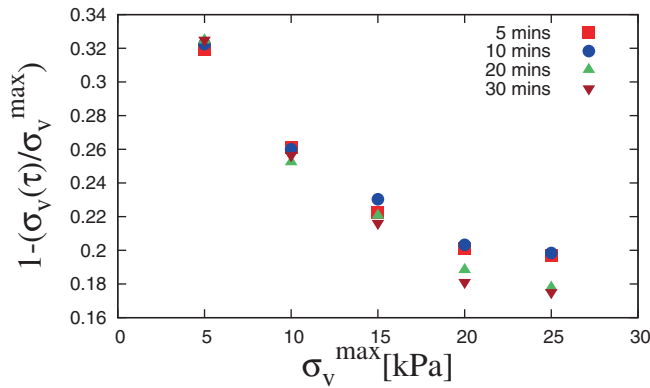


Figure 4.8: Comparison of the relaxed stress states after different relaxation duration  $\tau_R$  protocols, as given in the inset. The comparison is done at the same relaxation of  $\tau = 5$  minutes.

for all stresses.

In summary, the effect of the relaxation duration is found to become visible after the first intermediate stress where history effects from preceding relaxation stages manifest. Also, at  $\sigma_v^{\max} = 20$  and  $25$  kPa, the difference between the  $\tau_R = 20$  and  $30$  mins at the highest stress is small suggesting a saturation effect.

## 4.6 Conclusion and Outlook

We have performed oedometric experiments to study the slow relaxation of two cohesive powders under different consolidation stresses. The main goal was to study the slow relaxation behavior in two experimental devices, namely the custom-built lambdameter and the commercially available FT4 powder rheometer. Additionally, a comparison of the relation behavior of two industrially relevant cohesive powders, namely cocoa powder with 12% fat content and Eskal 500 limestone powder was explored.

A comparison of both testing equipments revealed a qualitative reproduction of the relaxation behavior, i.e. the decrease in stress occurring at constant strain. The lambdameter is found to produce a softer response to applied stress when compared to the FT4. Due to differences in aspect ratio and sample volume used in both devices, larger strain is required in the lambdameter to reach the same intermediate stress in comparison to the FT4. The relaxation model Eq. (4.3) captures well the decrease in stress during relaxation at different stress levels for both testing equipments with the parameter  $t_0$  strongly fluctuating and  $C$  systematically decreasing from low to high stress levels.

For the two cohesive powders studied, it is interesting that both materials show an identical response to axial loading until  $\approx 15$  percent strain where the difference in the response begins to manifest. Eskal 500 limestone is found to produce a softer response to applied vertical stress in comparison to cocoa powder. At the same stress level, cocoa powder is found to relax more slowly and more relative in amplitude than Eskal. In terms of the parameters of the model, the response timescale for Eskal,  $t_{0E}$ , is several orders of magnitude smaller than that of cocoa. On the other hand, the dimensionless parameter  $C$  shows a decreasing trend and is only about a factor two higher for cocoa than for limestone.

In terms of the relaxation duration, we find that the effect of longer relaxation is visible after relaxation at the second intermediate stress level ( $\sigma_v^{\max} = 5\text{kPa}$ ), leading to observable differences in relative stress reduction reached at  $\sigma_v(\tau = 5\text{mins})/\sigma_v^{\max}$ , reached at  $\tau = 5$  mins: Previous longer relaxation reduces the present relaxation.

Further studies will focus on the effect of different compression velocity (or strain rate) and the solution of the model for finite compression rate. The effects of system walls and aspect ratio of the experimental device also needs to be given further attention. The validity of the proposed model for relaxation at constant stress (or strain creep) will be investigated. Finally, the incorporation of the features of the present findings into discrete element contact models for cohesive powders will be explored.

## Acknowledgement

Helpful discussions with N. Kumar and M. Wojtkowski are gratefully acknowledged. This work is financially supported by the European Union funded Marie Curie Initial Training Network, FP7 (ITN-238577), see <http://www.pardem.eu/> for more information.



## Chapter 5

# Dosing of cohesive powders in a simplified canister geometry\*

### Abstract

*We perform experiments and discrete element simulations on the dosing of cohesive granular materials in a simplified canister geometry. The setup is a simplified canister box where the powder is dosed out of the box through the action of a constant-pitch screw feeder connected to a motor. A dose consists of a rotation step followed by a period of rest before the next dosage. From the experiments, we report on the operational performance of the dosing process through a variation of dosage time, coil pitch and initial powder mass. We find that the dosed mass shows an increasing linear dependence on the dosage time and rotation speed. In contrast, the mass output from the canister is not directly proportional to an increase/decrease in the number coils. By calibrating the interparticle friction and cohesion, we show that DEM simulation can quantitatively reproduce the experimental findings for smaller masses but also overestimate arching and blockage. With appropriate homogenization tools, further insights into microstructure and macroscopic fields can be obtained.*

---

\*Based on O. I. Imole, D. Krijgsman, T. Weinhart, V. Magnanimo, E. C. Montes, M. Ramaioli, and S. Luding. Experiments and Discrete Element Simulation of the Dosing of Cohesive Powders in a Canister Geometry. *In preparation*, 2014

## 5.1 Introduction and Background

The dynamic behavior of granular materials is of considerable interest in a wide range of industries (e.g. pharmaceutical, chemical and food processing). In these industries, every step in the product manufacturing process contributes to the final quality of the product. Hence, if uniform product quality is to be achieved, a full understanding and control of the different stages of the production process is essential. In many applications, the transport and conveying of granular materials is a common process that forms a critical part of many production and delivery techniques. For example, transport to silos, process transport, controlled drug delivery and dosing of beverages all rely on an effective and uniform delivery of granular materials. Also, the design of products for these processes is hugely dependent on having a good understanding of the transport behavior and metering process of granular assemblies.

When granular materials are being transported, the behavior of the granular material and the efficiency of the process will depend on several material properties including particle shape, particle size, surface roughness, frictional properties, cohesion and moisture content among others. Discontinuities and inhomogeneities in the micro-mechanical behavior of bulk assemblies of granular materials are ever-present hence, changes in operating condition affect the flow behavior of granular assemblies [115]. Also the geometry of the transport media (boundary conditions) including wall friction and the loading/preparation procedure will play an important role.

Over the past decade, the mechanism during transport of granular materials have attracted significant interests and efforts from researchers. These efforts can be grouped into three classes namely, experimental, numerical modelling and developing constitutive models to predict granular flows in conveying mechanisms [128, 176]. The numerical modelling of granular flows has been based on Discrete Element Method (DEM) as proposed in Ref. [34]. The earlier (more favored) experimental approach mostly involves the design and construction of experimental models of such applications followed by series of studies and benchmark tests to determine quantities of interest and fine-tune the process to desirable levels. Thereafter, a scale-up of the process can be performed. In this case, the challenging task is the selection of relevant parameters and boundary conditions to fully characterize the flow rheology in these systems.

A measure of knowledge in characterizing dry, non-sticky powders exists. For example, rotating drum experiments and simulations to determine the dynamic angle of repose have been studied extensively as a means to characterize non-cohesive powders [28, 153]. What has been less studied is the case where the powders are sticky, cohesive and less flowable like those relevant in the food industry. For these powders, dynamic tests are difficult to perform due to contact adhesion and clump formation. Inhomogeneities are also more rampant and flow prediction becomes even more troublesome.

Screw conveyors are generally used in process industries to transport bulk materials in a precise and steady manner. Materials like cereals, tablets, chemicals, pellets, salt and sand among others can be transported using screw conveyors. As simple as this process may seem, problems of inaccurate metering, unsteady flow rates, bridging, channeling, arching, product inhomogeneity, segregation, high start up torques, equipment wear and variable residence time have been reported [26, 33, 119, 120]. In addition, the design and optimization of screw conveyors performance is not well understood and has been based on semi-empirical approach or experimental techniques using dynamic similarities as pointed out in Ref. [26]. Earlier researchers have investigated the effect of various screw (auger) parameters including choke length (the distance beyond which the screw projects beyond the casing at the lower end of the intake) and pitch–diameter ratio (See Refs [45, 129, 149] and references therein). Robert and Willis [129] reported that since grain motion is largely influenced by its centrifugal inertia, augers with large diameters attain maximum output at lower speeds compared to those with small diameters. They also reported that for maximum throughput during conveying, longer chokes are necessary.

The subject of modelling screw conveying of granular materials with the Discrete Element Method (DEM) [34] is fairly recent. One of the earliest work on this subject was reported in Ref. [142] where the performance of horizontal and vertical screw conveyors are investigated and results are compared with empirical equations. In a related work, Owen et al. [119] studied the performance of a long screw conveyor by introducing the so-called ‘periodic slice’ model. Along this line, Cleary [33] investigated the effects of particle shape on flow out of hoppers and on the transport characteristics of screw conveyors. Experiments on the dosing of glass beads and cohesive powders along with the discrete element simulation of the dosing of glass beads have also been reported [126]. A fundamental question is the extent to which discrete element simulations can predict the dosing of these powders, especially when the powders are cohesive.

In the current study, we use experiments and discrete element simulations to investigate the dosing of cohesive powders in a simplified canister geometry. The characterization of the experimental samples, experimental set-up and procedure are presented in section 5.2. In section 5.3, we present the force model, simulation parameters and homogenization technique followed by a discussion of experimental and numerical results in section 5.4. Finally, the summary, conclusions and outlook are presented in section 5.6.

## 5.2 Dosage Experiments

In this section, we discuss in detail the experimental set-up and measurement procedure along with the material parameters of the experimental sample.

Property		Unit	Value
Size distribution	$d_{10}$	$\mu\text{m}$	31.55
	$d_{50}$	$\mu\text{m}$	184
	$d_{90}$	$\mu\text{m}$	979.19
Span	$(d_{90} - d_{10})/d_{50}$	[-]	5.151
Particle Density		$[\text{kg}/\text{m}^3]$	1427
Specific surface area		$\text{m}^2/\text{g}$	0.088

Table 5.1: Material properties of the experimental cocoa sample.

### 5.2.1 Sample Description and Characterization

The cohesive granular sample used in this work is cocoa powder with material properties shown in Table 5.1. The particle size distribution (PSD) is obtained by the “dry dispersion module” of the Malvern Mastersizer 2000 (Malvern Instruments Ltd., UK), while the particle density is obtained by helium pycnometry (Accupyc, Micromeritics, US). The span is defined as the width of the distribution based on the 10%, 50% and 90% quantile. The experiments were performed over a relatively short period under ambient conditions and samples are sealed in air-tight bags when not in use to minimize effects that could arise due to changes in the product humidity.

### 5.2.2 Experimental Set-up

The setup is a simplified canister box where the powder is dosed out of the box through the action of a constant-pitch screw feeder connected to a motor. A schematic representation of the experimental set-up is shown in Fig. 5.1 along with the dimensions on Table 5.2. A typical experiment begins with the careful filling of the canister with the exit closed until a pre-determined powder mass is reached. Care is taken to ensure that the initial profile of the powder surface is as flat as possible and that any pre-compaction that may arise due to shaking or vibrations are minimized. Subsequently, the dosing experiment begins with the rotation of the screw for a specified time duration followed by an intermediate rest before the next dosage. The dosed mass per screw turn is recorded through a weighing scale connected to a computer. The experiment is complete when the cumulative dosed mass recorded for three consecutive doses is less than 0.15grams indicating either the box is empty or the powder is blocked through arching in the canister. In addition, to obtain and post-process the profiles of the sample surface during the experiments, an external camera (Logitech HD Pro, Logitech Int'l SA) was mounted in front of the canister box and a video recording of each experiment was obtained.

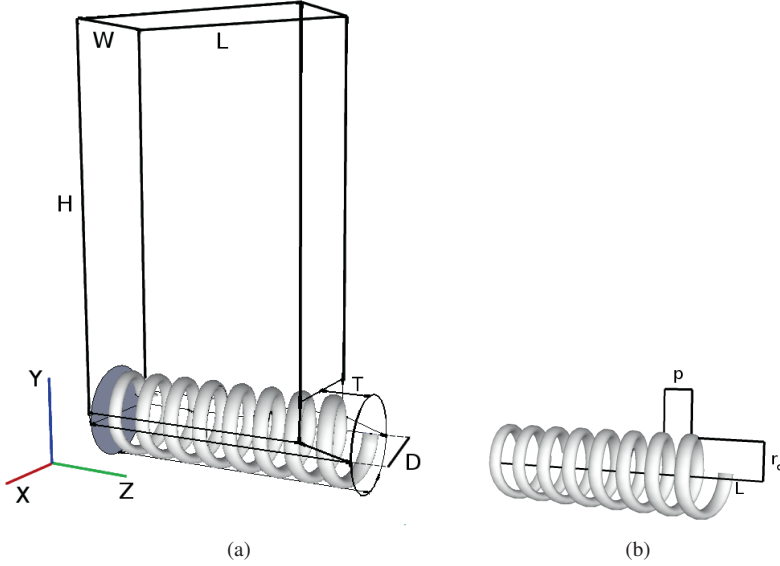


Figure 5.1: Schematic representation of the (a) simplified canister, (b) the coil used for the dosing experiments and simulation, with box length ( $L$ ), width ( $W$ ), height ( $H$ ), throat length  $T$ , outlet diameter ( $D$ ), coil radius  $r_c$  and pitch  $p$ .

### Image Processing

Snapshots of the profile of the powder surface during each experiments were obtained using a camera attached to the experimental set-up. To improve the quality of the snapshots and for comparison, we use the open-source software FIJI [136] to post-process the images following a three step procedure, namely quality adjustment, binarization and extraction of the lateral surface of the powder. In the first stage, we adjust the quality of the images by first selecting the region of interest and enhancing its contrast. In the second stage, the image is binarized into black (0) and white (1) pixels such that the area containing the bulk sample is easily differentiated from other areas in the picture. In the final step, we iteratively move along the length of the image from top to bottom to trace out the profile of the powder surface.

For a given rotation speed, the linear coil (push) velocity is:

$$V_z = \frac{p\omega}{2\pi} \quad (5.1)$$

where  $\omega$  is the angular velocity of the coil and  $p$  is the pitch of the coil. Also, the coil tangential velocity is:

$$V_t = \omega r_c \quad (5.2)$$



where  $r_c$  is the coil radius. Accordingly, the expected dosed mass for a single rotation of the coil is:

$$m_{\text{exp}}^{\text{dose}} = \rho_b \cdot V_c \cdot n_t = \rho_b \cdot p \cdot \pi r_c^2 \cdot n_t \quad (5.3)$$

where  $\rho_b$  is the bulk density,  $V_c$  is the volume within a single pitch and  $n_t = t_d \cdot \omega / 2\pi$  is the number of rotations completed within a given dosing time  $t_d$ . The expected number of doses is then:

$$N_{\text{exp}}^{\text{dose}} = \frac{m_{\text{tot}}}{m_{\text{exp}}^{\text{dose}}} \quad (5.4)$$

where  $m_{\text{tot}}$  is the total initial mass filled into the canister.

### 5.3 Numerical Simulation

The numerical simulation was carried out using the open source discrete element code MercuryDPM [155, 172]. Since DEM is otherwise a standard method, only the contact model and the basic system parameters are briefly discussed.

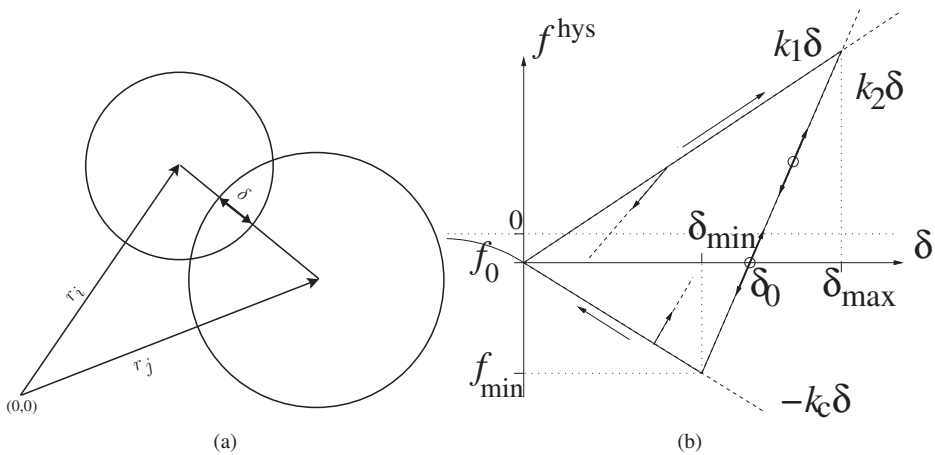


Figure 5.2: (a) Two particle contact with overlap  $\delta$  in normal direction. (b) Schematic graph of the linear, hysteretic, adhesive force-displacement model in normal direction

### 5.3.1 Force Model

Since realistic and detailed modeling of the deformations of particles in contact with each other is much too complicated, we relate the interaction force to the overlap  $\delta$  of two particles as shown in Fig. 5.2a. Thus, the results presented here are of the same quality as the simplifying assumptions about the force-overlap relations made. However, it is the only way to model larger samples of particles with a minimal complexity of the contact properties, taking into account the relevant phenomena: non-linear contact elasticity, plastic deformation, and adhesion.

In this work, we use the Luding's linear hysteretic spring model [92] – which is a simplified version of more complicated non-linear hysteretic force laws [132, 161, 162, 169, 183]. The adhesive, plastic (hysteretic) normal force is given as:

$$f^{\text{hys}} = \begin{cases} k_1 \delta & \text{if } k_2(\delta - \delta_0) \geq k_1 \delta \\ k_2(\delta - \delta_0) & \text{if } k_1 \delta > k_2(\delta - \delta_0) > -k_c \delta \\ -k_c \delta & \text{if } -k_c \delta \geq k_2(\delta - \delta_0) \end{cases} \quad (5.5)$$

with  $k_1 \leq k_2 \leq \hat{k}_2$  as shown in Fig. 5.2b where  $\hat{k}_2$  is the maximum stiffness and  $f_0$  has been set to zero. During initial loading the force increases linearly with the overlap, until the maximum overlap  $\delta_{\text{max}}$  is reached ( $\delta_{\text{max}}$  is kept in memory as a history variable). The line with slope  $k_1$  thus defines the maximum force possible for a given  $\delta$ .

During unloading the force drops on a line with slope  $k_2$ , which depends, in general, on  $\delta_{\text{max}}$ . The force at  $\delta = \delta_{\text{max}}$  decreases to zero, at overlap  $\delta_0 = (1 - k_1/k_2)\delta_{\text{max}}$ , which resembles the plastic contact deformation. Reloading at any instant leads to an increase of the force along the same line with slope  $k_2$ , until the maximum force is reached; for still increasing  $\delta$ , the force follows again the line with slope  $k_1$  and  $\delta_{\text{max}}$  has to be adjusted accordingly [92].

Unloading below  $\delta_0$  leads to attractive adhesion forces until the minimum force  $-k_c \delta_{\text{min}}$  is reached at the overlap  $\delta_{\text{min}} = (k_2 - k_1)\delta_{\text{max}}/(k_2 + k_c)$ , a function of the model parameters  $k_1, k_2, k_c$ , and the history parameter  $\delta_{\text{max}}$ . Further unloading leads to attractive forces  $f^{\text{hys}} = -k_c \delta$  on the adhesive branch. The highest possible attractive force, for given  $k_1$  and  $k_2$ , is reached for  $k_c \rightarrow \infty$ , so that one has  $f_{\text{min}} \geq -(k_2 - k_1)\delta_{\text{max}}$  for arbitrary  $k_c$ .

A more realistic behavior will be a non-linear un-/re-loading behavior. However, due to a lack of detailed experimental information, the piece-wise linear model is used as a compromise. One reasonable refinement, which accounts for an *increasing unloading stiffness with deformation*, is a  $k_2$  value dependent on the maximum overlap. This also implies relatively small and large plastic deformations for weak and strong contact forces, respectively. Unless a constant  $k_2 = \hat{k}_2$  is used, the contact model [90, 91, 97], requires an additional quantity,

Parameter	Value
Canister dimensions ( $L \times W \times H$ )	$60 \times 23 \times 170$ mm
Throat length ( $T$ )	10 mm
Outlet diameter ( $D$ )	23 mm
Coil thickness	2 mm
Coil length	70 mm
Coil radius ( $r_c$ )	10.4 mm
Number of coils	4 (Wide), 8 (Narrow)
Coil pitch	17.5 mm (Wide), 8.75 mm (Narrow)
Coil angular velocity ( $\Omega$ )	90 rpm (9.42 rad/s)

Table 5.2: Summary of system parameters used in the experiments and DEM simulations.

i.e., the plastic flow limit overlap

$$\delta_{\max}^* = \frac{\hat{k}_2}{\hat{k}_2 - k_1} \phi_f \frac{2a_1 a_2}{a_1 + a_2}, \quad (5.6)$$

with the dimensionless plasticity depth  $\phi_f$ , defined relative to the reduced radius. If the overlap is larger than a  $\phi_f$  fraction of the particle radius (for radius  $a_1 = a_2$ ), the (maximal) constant stiffness constant stiffness  $\hat{k}_2$  is used. For different particle radii, the reduced radius increases towards the diameter of the smaller particles in the extreme case of particle-wall contacts (where the wall-radius is assumed infinite).

Note that a limit stiffness  $k_2 \leq \hat{k}_2$  is desirable for practical reasons. If  $k_2$  would not be limited, the contact duration could become very small so that the time step would have to be reduced below reasonable values. For overlaps smaller than  $\delta_{\max}^*$ , the function  $k_2(\delta_{\max})$  interpolates linearly between  $k_1$  and  $k_2$ :

$$k_2(\delta_{\max}) = \begin{cases} \hat{k}_2 & \text{if } \delta_{\max} \geq \delta_{\max}^* \\ k_1 + (\hat{k}_2 - k_1) \frac{\delta_{\max}}{\delta_{\max}^*} & \text{if } \delta_{\max} < \delta_{\max}^*. \end{cases} \quad (5.7)$$

The implementation of the tangential forces and torques have been described extensively in Refs. [90–92, 97].

### 5.3.2 Simulation Procedure and Parameters

The actual number of particles present in the bulk powder used in the dosing experiments are of the order several billions. The realistic simulation of the exact size is exceptionally challenging due to computational cost. Due to this constraint, one choice available is to either scale the system size while keeping particle properties fixed. The other choice is to do the contrary, namely keeping the system size fixed and scaling (or coarse graining) the particle sizes up by essentially making them meso particles. We choose to do the latter, namely using the same system size in simulation as in experiments and increasing the size of our particles so that each meso-particle in our system can be seen as an ensemble of smaller constituent particles. The system parameters used in both simulation and experiment are presented in Table 5.2. Note that the number of coils refer to the number of turns in the coil which, when divided by the length of the coil should give an indication of the pitch of the coil. Typical numerical parameters used in the DEM simulation are listed in Table 5.3.

The numerical implementation of the dosing test is as follows. The particles are generated and positioned on regular grid points within the dimensions of the box. To avoid any initial overlap of particles, either with the coil, surrounding wall or with other particles, we ensure that the initial position of the lowest particle during this generation stage is higher than the diameter of the coil. Subsequently, the particles are allowed to fall under gravity and are left to settle and dissipate their energies for 2 seconds while the coil is not rotating. We find that for strong cohesion, this preparation method leads to initial inhomogeneities and irregular packing within the circumferential area of the coil during the settling phase. This gives rise to irregular dose patterns and increases the possibility of arches (blockage) forming just above the screw. To minimize this, the particles are allowed to settle with a initial cohesive stiffness  $k_c/k = 0.3$  such that the initial packing structure is homogeneous while the actual cohesion is activated after the settling phase.

### 5.3.3 Homogenization Technique

In order to drive macroscopic fields such as density, velocity and stress tensor from averages of the microscopic discrete element variables such as the positions, velocities and forces of the constituent particles, we use the coarse-graining method proposed in Refs. [50, 170–172].

The microscopic mass density of a flow at a point  $\mathbf{r}_\alpha$  at time  $t$  is defined by

$$\rho^{\text{mic}}(\mathbf{r}, t) = \sum_{i=1}^N m_i \delta(\mathbf{r} - \mathbf{r}_i(t)), \quad (5.8)$$

where  $\delta(\mathbf{r})$  is the Dirac delta function and  $m_i$  and  $r_i$  are the mass and center of mass position

Parameter	Experiment	Simulation
Number of Particles	$> 10^{10}$	3360 for $m_{\text{tot}} = 48$ grams
Mean particle diameter ( $\langle d \rangle$ )	0.184mm	2.50 mm
Particle density ( $\rho$ )	$1.427 \times 10^{-6} \text{ kg/mm}^3$	$1.427 \times 10^{-6} \text{ kg/mm}^3$
Polydispersity ( $w$ )	see Table 5.1	$r_{\text{max}}/r_{\text{min}} = 3$
Restitution coefficient ( $e$ )	[-]	0.45
Plasticity depth ( $\phi_f$ )	[-]	0.05
Maximal elastic stiffness ( $k = \hat{k}_2$ )	[-]	24067 kg/s <sup>2</sup>
Plastic stiffness ( $k_1/k$ )	[-]	5
Cohesive stiffness ( $k_c/k$ )	[-]	0.873 (varied 0–1)
Friction stiffness ( $k_t/k$ )	[-]	0.286
Rolling stiffness ( $k_r/k$ )	[-]	0.286
Coulomb friction coefficient ( $\mu$ )	[-]	0.5 (varied 0.5–0.65)
Rolling friction coefficient ( $\mu_r$ )	[-]	0.5
Normal viscosity ( $\gamma_n = \gamma$ )	[-]	0.0827 kg/s
Friction viscosity ( $\gamma_t/\gamma$ )	[-]	0.286
Rolling viscosity ( $\gamma_r/\gamma$ )	[-]	0.286
Wall friction ( $\mu_w$ )	[-]	0.2
Contact duration $t_c$	[-]	$1.1297 \times 10^{-4} \text{ s}$

Table 5.3: Numerical values of parameters used in experiment and DEM simulations.

of particle  $i$ . Accordingly, the macroscopic density can be defined as:

$$\rho(\mathbf{r}, t) = \sum_{i=1}^N m_i \mathcal{W}(\mathbf{r} - \mathbf{r}_i(t)), \quad (5.9)$$

where the Dirac delta function has been replaced with an integrable ‘coarse-graining’ function  $\mathcal{W}$  whose integral over the domain is unity and has a predetermined width, or homogenization scale  $w$ . In this work, we use a Gaussian coarse-graining function.

The homogenized momentum density is also defined as:

$$p_\alpha(\mathbf{r}, t) = \sum_{i=1}^N m_i v_{i\alpha} \mathcal{W}(\mathbf{r} - \mathbf{r}_i). \quad (5.10)$$

with  $v_{i\alpha}$  the velocity of particle  $i$ . The macroscopic velocity field  $V_\alpha(\mathbf{r}, t)$  is defined as the ratio of momentum and density fields,  $V_\alpha(\mathbf{r}, t) = p_\alpha(\mathbf{r}, t)/\rho(\mathbf{r}, t)$ . Comparing other fields, like stress- and structure- tensors as shown in Refs. [50, 170–172], is beyond the scope of this study.

In order to obtain the height variation during the dosing process  $h_z$  as in experiment, we average over the height and the depth of the drum

The height variation of the packing during the dosing is given as:

$$h_z = \frac{m_{\text{bin}}(z, t)}{m_{\text{bin}}(z, 0)} \cdot h_{\text{ini}} = \frac{\rho(z, t)}{\rho(z, 0)} \cdot h_{\text{ini}}, \quad (5.11)$$

assuming an almost constant bulk density.  $m_{\text{bin}}(z, t)$  is the mass change as function of time during the dosing process,  $m_{\text{bin}}(z, 0)$  is the initial mass of the particles at time  $t = 0$  and  $h_{\text{ini}}$  is the initial height of the packing. Furthermore, the mass in a bin as function of time is:

$$m_{\text{bin}}(z, t) = \int_0^{\Delta z} \int_0^H \int_0^D \rho(x, y, z, t) dx dy dz \quad (5.12)$$

where  $D$  is the depth (or width) of the drum,  $H$  the box height, and  $\Delta z$  the bin width.

## 5.4 Experiments

In this section, we present the results from the experiments and simulations and their comparison. For an understanding of the dosing process, in the following, we present experimental

results on the effect of initial mass, number of coils and dosage time.

### 5.4.1 Effect of Initial Mass in the Canister

In Fig. 5.3a, we plot the cumulative dosed mass as function of the number of doses for sample masses  $m_{\text{tot}} = 60\text{g}$ ,  $80\text{g}$  and  $100\text{g}$  in the canister. For these experiments, a dose consists of the rotation of the narrow pitch screw for 2 seconds at a speed of  $90\text{rpm}$ . As expected the number of doses increases with increasing the mass of powder filled in the canister. The number of doses recorded when 99 percent of the total powder mass in the canister is dosed are 16, 23 and 30, for the 60, 80 and 100g fill masses respectively.

The mass per dose obtained for different initial masses is close as shown by the near collapse of the data on each other. We however note that the sensitivity of the mass per dose to the initial mass is tiny as seen in the inset.

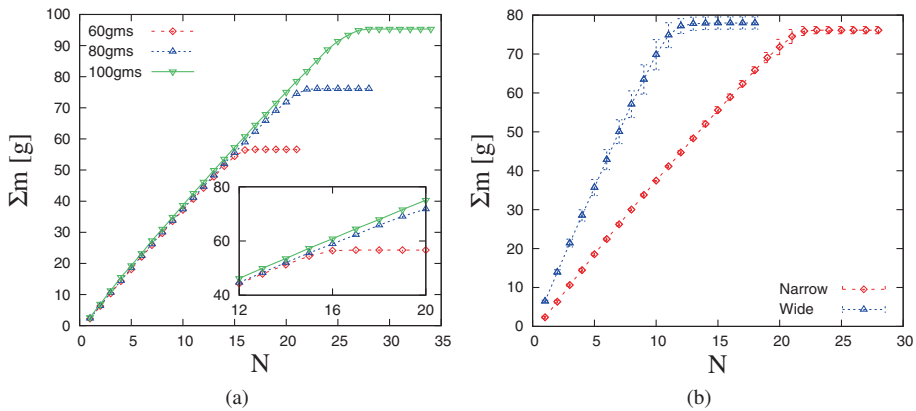


Figure 5.3: (a) Cumulative dosed mass from experiments plotted as function of the number of doses for (a) different initial mass in the box (b) different coils (pitch).

### 5.4.2 Effect of Number of Coils

In Fig. 5.3b, we plot the cumulative dosed mass as function of the number of doses for experiments with two different coils namely a wide coil with 4 coils (or crests) and a narrow coil with 8 crests. The initial powder mass in the canister is  $80\text{g}$  and a dose consists of the rotation of the coil for 2 seconds at a speed of  $90\text{rpm}$ . The error bars represent the standard deviation over three experimental runs for each test. From Fig. 5.3b, it is evident that the dosed mass per coil turn for the coil with the wide pitch is higher compared to the dosed

mass reported for the narrow screw. As a result, the cumulative dosed mass recorded for the coil with the wide pitch increases faster (with slope 7.15 g/dose) in comparison to the narrow one (3.705 g/dose). This indicates that increasing the number of coils from 4 to 8 leads to almost double increase in the mass per dose.

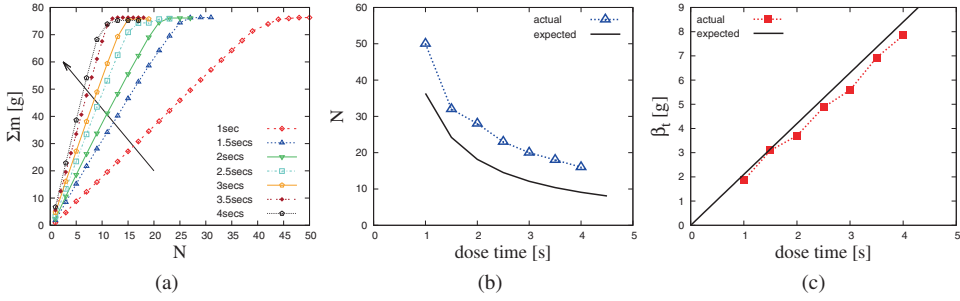


Figure 5.4: (a) Cumulative dosed mass from experiments plotted as function of the number of doses for different dose time, (b) number of doses recorded for the respective dose times, and (c) mass per dose plotted for different dosage times. The solid black lines represent the expected mass  $m_{\text{exp}}^{\text{dose}}$  using Eq. (5.3) and the expected doses  $N_{\text{exp}}^{\text{dose}}$  using Eq. (5.4), as prediction.

### 5.4.3 Effect of Dosage Time

To understand the effect of dosage time, in Fig. 5.4a, we vary the dosage time from 1-4 s while keeping the initial powder mass in the canister and the rotation speed constant at 80g and 90rpm respectively. A first observation is the higher slope for longer dosing time, that leads to a decrease in the number of doses recorded. This is explained by the increased number of complete screw rotations as the dosage time is increased, thus allowing for an increased mass throughput. In Fig. 5.4b, we plot the number of doses for different dose time, and observe inverse proportionality. Also, the expected number of doses predicted using Eq. (5.4) is lower. The decrease in the number of doses is faster between  $t=1-1.5$  s and then slows down as the time increases until  $t=4$  s. In Fig. 5.4c, we plot the actual (red squares) and predicted (solid black line) mass per dose  $\beta_t$  taken from the cumulative dosed mass before saturation, for different dose time. The predicted mass per dose is obtained using Eq. (5.3) for an initial bulk density  $\rho_b \approx 4.71 \times 10^{-4}$  g/mm<sup>3</sup>, coil pitch  $p = 8.75$  mm and coil radius 10.4 mm. We observe a linear increase in the mass per dose with increasing dosage time. The experimental mass per dose for the different dosage times is close to the predicted values with the predicted mass slightly higher. This indicates that less mass is being transported per dose, which could be due to the uneven, inhomogeneous re-filling of the coil during the dosing process and due to the small volume of the coil that is not



considered in Eq. (5.3).

## 5.5 Numerical Results

In this section, we discuss the results from discrete element simulations of the dosing test. First, we compare the snapshots of the particle bed surface with images taken from experiments. Next, we describe the process of calibration of the material parameters used in our simulations. As studied in the experiments, we show results on varying the dosage time, coil rotation speed and number of coils. Finally, we report on the macroscopic velocity and density fields during the dosing process.

### 5.5.1 Surface profile of the dosed material

As a first step to gain insights into the dosing process, we show exemplary snapshots of the time evolution of the surface profile of bulk sample during a typical simulation in Figs. 5.5(a-d). For this study, the initial mass in the box is set at 60grams while the coil with the narrow pitch (8 complete turns) is used. Fig. 5.5(a) shows the state of the bulk sample after the first 2 seconds where the particles have been allowed to settle. At this point, the kinetic energy of the particles are close to zero since they are non-mobile. As the coil begins to turn in Fig. 5.5(b) after the relaxation phase, particles within the area of the coil begin to move leading to an increase in their kinetic energy, as seen from the bright colors in the lower part of the box. In general, particles around the uppermost layer of the box remain largely static while the the region where the kinetic energy is highest can be seen around the rear end of the coil. Moving further in time to Fig. 5.5(c), we find that the emptying of the box occurs faster at the rear (left) end of the box, thereby causing avalanches as the void left due to the emptying of the box is filled. In addition to this, we observe in some cases, arches forming above the coil, where the void created below the screw is visible. We must also point out that particles closest to the right wall of the box remain static and they only collapse into the coil at the base as an increased amount of powder is dispensed from the box as shown in Fig. 5.5(d).

Along with this, in Figs. 5.5(e-h) we show image processed visualizations of the experimental powder profile during the dosing process. From the initial solid, bulk powder in Fig. 5.5(e), we observe a progressive change in the powder surface profile with the canister emptying faster from its left rear end. Arches forming on the lower left side of the box above the coil is also seen leading to avalanches and collapse of the powder around this region.

In summary, comparing the experimental and simulation profiles of the powder surface, we observe that the essential features observed in the experiment, namely the faster emptying

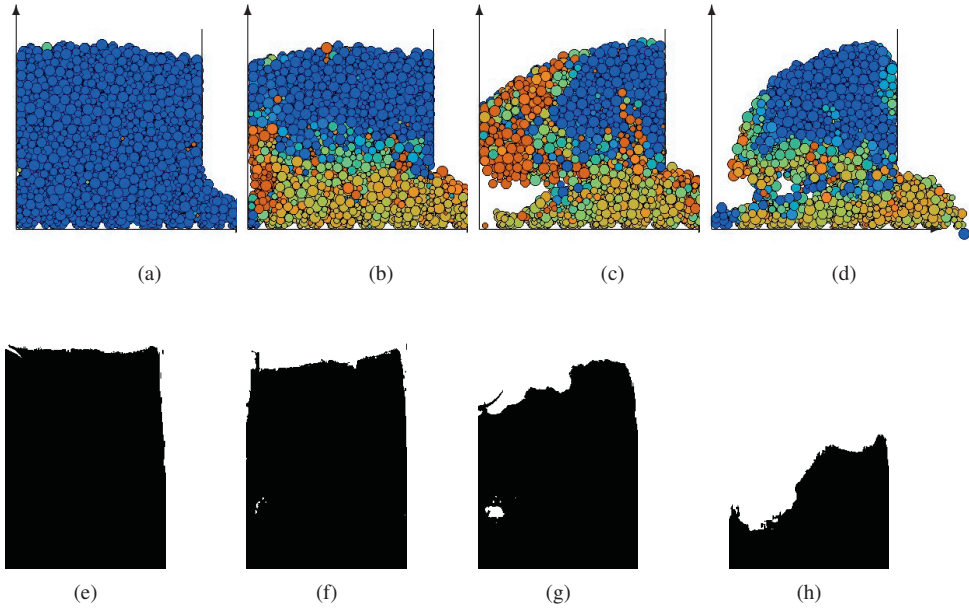


Figure 5.5: Snapshot of the time evolution of the simulation during the dosing test with time increasing from (a–d) and (e–h), respectively. (a–d) are taken from simulation while comparable snapshots (e–h) are image processed experimental visualizations of the powder profile. Colors/shades in (a–d) indicate the kinetic energy of the particles with blue (static) and orange (dynamic) particles. For the simulation, parameters are  $K_c = 0.872$  and  $\mu = 0.5$ . The coil is not shown for clarity.

at the rear end of the coil and arches forming during ongoing dosage are reproduced in the simulation. Also, we must point out that the faster emptying at the rear end of the coil is due to the design of the coil which can be mitigated through the use of conical inserts in the coil [126]. In the next sections, we will focus on a quantitative comparison between experiments and simulation.

### 5.5.2 Calibration and Sensitivity Studies

The particles used in the simulation can be seen as meso-particles consisting of an agglomerate of other smaller particles. Due to this, it is important that their material properties are carefully selected based on sensitivity studies of how each parameter influence the dosing process in comparison to the experiment.

In order to obtain relevant parameters unique for our problem, we perform various studies in order to test the sensitivity of the essential material parameters, namely interparticle friction and cohesion during the dosing process. To achieve this, several simulations were run where

the interparticle friction is fixed in each case and cohesion is varied. Note that for each simulation, we obtain data on the cumulative dosed mass and the number of doses. From each simulation, the respective mass per dose  $\beta$  are obtained within the linear region where initial conditions and other artefacts due to arching are absent. The mass per dose  $\beta$  is then systematically compared for different interparticle friction and cohesion and bench-marked against the obtained experimental  $\beta$  value. We choose  $\beta$  as a calibration parameter since it is largely independent of the initial mass (see Fig. 5.3a). The For the sake of brevity, this calibration procedure is performed on using a total mass of 48grams in the box and the narrow pitch coil with 8 complete turns. We attempted a calibration with higher masses as compared with the experiments but we observe that due to arching occurring when cohesion is high, the plot of the cumulative dosed mass becomes non-linear. This made defining an appropriate  $\beta$  challenging therefore requires further work. In the mean time, we focus the calibration with the lower mass.

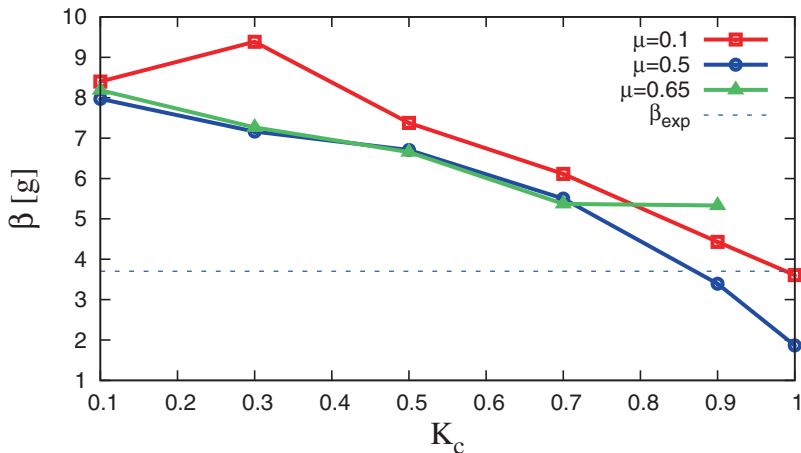


Figure 5.6: Calibration of the cohesive stiffness  $K_c = k_c/k$  and inter particle friction  $\mu$ . Here we plot the mass per dose  $\beta$  for different  $K_c$  and different  $\mu$  as given in the inset. The dotted horizontal line shows the experimental  $\beta$  value.

In Fig. 5.6, we show the mass per dose  $\beta$ , plotted against the interparticle cohesive stiffness  $K_c$  and different interparticle friction coefficient  $\mu$ . The horizontal dotted line shows the mass per dose obtained in the experiment with value 3.702g/dose. A first observation is the consistent decrease of  $\beta$  with increasing  $K_c$  for all friction. This is due to reduced flowability of the bulk sample with increasing cohesion. We note however that for the highest friction, we observe a slight increase in the  $\beta$  values obtained at high cohesion. This is a consequence of arching that sets in due to high cohesion causing a bridge in the flow especially in the region above the coil. This leads to highly unsteady mass throughput from the box.

Comparing the data for different friction, we observe a decrease in  $\beta$  with increasing  $\mu$ .

Increased interparticle friction leads to an an increased resistance to flow which reduces the rate at which the material is being dispensed out of the box and consequently lower  $\beta$ . Similar to what is found in other studies, for interparticle friction within the range  $\mu = 0.5$  and  $0.65$ , the effect becomes less strong as seen in the saturation and collapse of  $\beta$ .

As seen from Fig. 5.6, the experimental measured mass per dose (dotted horizontal line) intersects with the different friction data at different points leading to different possible  $K_c$  values. A choice therefore has to be made of the appropriate  $K_c$  which reproduces the experiments and leads to the least variability between successive doses in the simulations. In this case, we choose the lowest possible  $K_c$  which gives the match with the experimental  $\beta$  value at  $K_c = 0.872$  and  $\mu = 0.50$ .

### 5.5.3 Comparison with Experiments

In order to test the validity of the interparticle friction and cohesion parameters obtained from the calibration test, we perform simulation setting  $K_c = 0.872$  and  $\mu = 0.5$ . We then compare the simulation results with experiments. We note that the total mass  $m_{\text{tot}}$  used in experiment is approximately 60grams while the simulation mass is 48grams. For both experiment and simulation, the narrow coil with 8 turns is used. For each dose, the coil is rotated at a speed of 90rpm for 2 seconds.

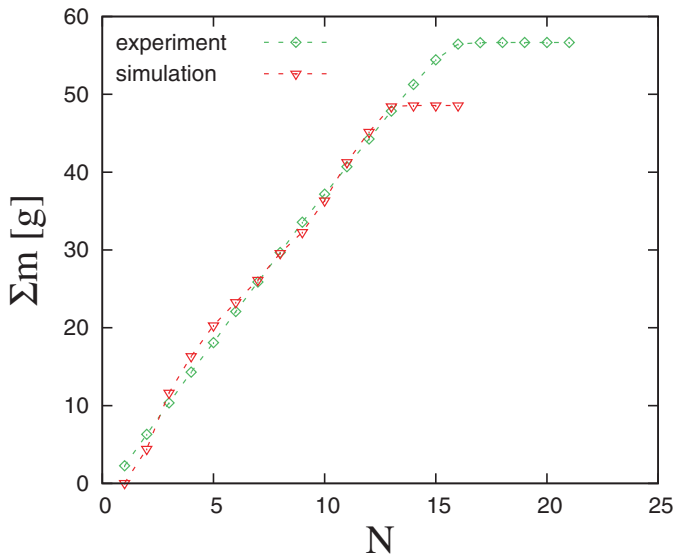


Figure 5.7: Comparison between simulation and experiment. Here we plot the cumulative dosed mass as function of the number of dose obtained from experiment and simulation. For simulations,  $m_{\text{tot}} = 48\text{g}$ , and parameters are  $K_c = 0.872$ , and  $\mu = 0.5$ .

The comparison between simulation and experiments is shown in Fig. 5.7. We observe that for the first few doses, the experimental and numerical dosed masses obtained are slightly different – with the simulation slightly under-predicting the experimental masses. This is possibly arising from the different initial preparation and the randomness of the initial states. After the first few doses, the simulation is observed to compare well with experiments as shown by the collapse of both datasets on each other. By comparing the individual points on the cumulative dosed mass plots between experiment and simulation, we obtain a maximum variation in mass per dose of less than 9 percent. This is comparable to the variation of about 5 percent obtained for experiments with different masses (see section 5.4.1).

### 5.5.4 Parametric Studies

In this subsection, we will discuss the numerical results of parametric studies on the dosing experiments. Similar to the experiments, we investigate the effect of varying the dosage time and the number of coils. Although not studied in the experiment, we also look at the effect of higher rotation speeds during the dosing action.

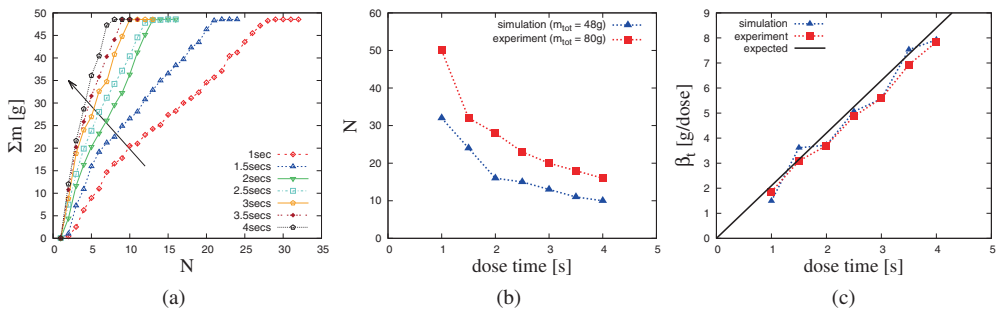


Figure 5.8: (a) Cumulative dosed mass from simulation plotted as function of the number of dose for different dose time; (b) Number of doses obtained from the respective simulations and experiments for different dose times; (c) mass per dose obtained from simulation (from the first few doses) and experiments for different dose times. The solid black line represents the expected mass  $m_{exp}^{dose}$  using Eq. (5.3) as prediction.

In Fig. 5.8, we plot the cumulative dosed mass as function of the number of dose for different dosage times. The initial mass in the canister is 48grams while the interparticle friction and cohesion are kept constant at 0.5 and 0.872, respectively. From Fig. 5.8a, we observe that the cumulative dosed mass increases slightly non-linearly as the number of doses increases. The effect of slight arching and inhomogeneous density is evident by the slight reduction in the mass per dose as the number of dose increases. Due to this, the mass per dose is obtained over the first few doses before arching sets in. The number of dose is obtained when the

cumulative dosed mass does not change for three consecutive doses. As observed in the experiments, we find that the number of doses required to empty the particles in the box shown in Fig. 5.8b also clearly decreases with an increase in the dosage time. The number of doses obtained for experiments is higher than those obtained in experiments since a higher initial mass ( $m_{\text{tot}} = 80\text{grams}$ ) is used in experiment compared to 48grams in simulation. However, a comparable number of doses is obtained if the difference in mass between simulation and experiment is corrected for.

The mass per dose  $\beta_t$  for different dosage time is compared between simulation and experiment in Fig. 5.8c. For all simulations, the mass per dose is obtained from the first few doses as the slope of the cumulative dosed mass in the linear region where the cumulative dosed mass is less than 15 grams. Recall that the calibration was done at a dose time of 2 seconds while parameters obtained are then used for the other dose times. The mass per dose is found to increase linearly with the dose time in simulation and experiments. The mass per dose obtained from experiments and simulation for different dosage times are slightly lower than the prediction from Eq. (5.3).

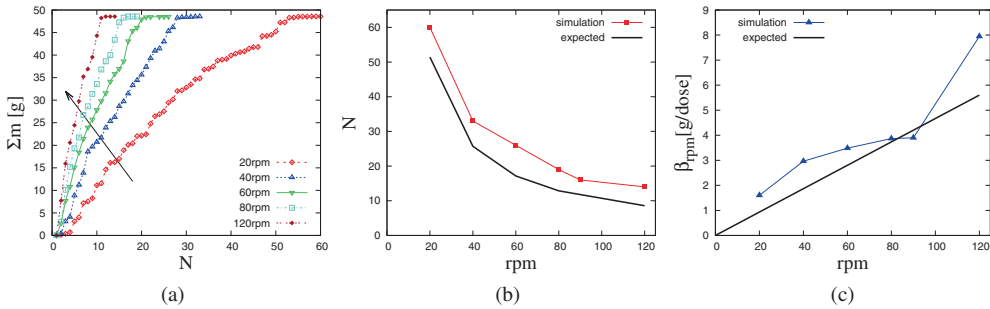


Figure 5.9: (a) Cumulative dosed mass from simulations plotted as function of the number of doses for different rotation speeds (b) Number of dose and (c) mass per dose  $\beta_{rpm}$  obtained from the respective simulations for different rotation speeds. The solid black lines represent the expected mass  $m_{\text{exp}}^{\text{dose}}$  using Eq. (5.3), and the expected doses  $N_{\text{exp}}^{\text{dose}}$  using Eq. (5.4), as prediction.

The effect of varying the rotation speed is presented in Fig. 5.9. For these simulations, the dose time is fixed to 2 seconds while the rotation speed is varied. It is evident that the box empties faster with increasing rotation speed. Also, the number of doses required for the complete emptying of the box, shown in Fig. 5.9b, is found to decrease fast between 20rpm and 40rpm followed by a much slower decrease upon further increase in the coil rotation speed. The slope (mass per dose) of the cumulative dosed mass, obtained from the first few doses for different rotation speeds  $\beta_{rpm}$ , shown in Fig. 5.9c, increases with rotation speed – similar to  $\beta_t$  observed when the dosage time is varied. Here, interestingly the expected mass per dose, Eq. (5.3) mostly under-predicting the simulation, possibly due to on-going refilling

of the coil during rotation and variation in the bulk density from compaction and avalanches occurring during the simulation.

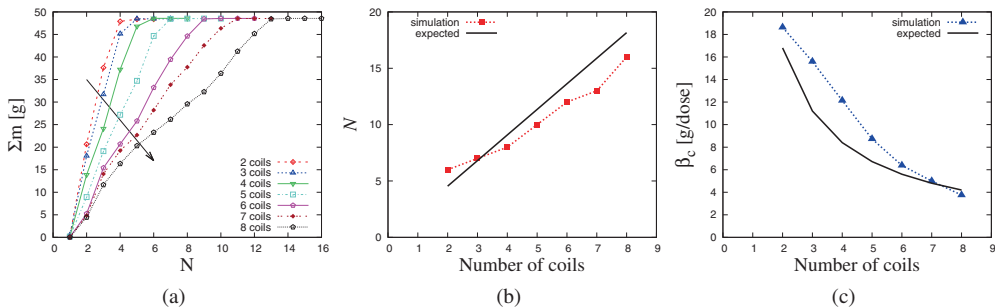


Figure 5.10: (a) Cumulative dosed mass from simulation plotted as function of the number of doses for different number of coils. The arrow indicate the decreasing trend with increasing number of coils. (b) Number of doses and (c) mass per dose  $\beta_c$  obtained from the respective simulations for different number of coils. The solid black lines represent the expected mass  $m_{\text{exp}}^{\text{dose}}$  using Eq. (5.3), and the expected doses  $N_{\text{exp}}^{\text{dose}}$  using Eq. (5.4), as prediction.

Simulation results on the effect of varying the number of coils from 2 to 8 coils are shown in Fig. 5.10. Increasing the number of coils essentially means reducing the pitch of the coil such that the simulation with two coils has the widest pitch. An increase in the number of coils is accompanied by an increase in the number of doses as shown in Fig. 5.10b, due to the decrease in the mass per dose, as can be seen from Fig. 5.10c. The volume of particles transported per dose in the system with 2 coils is more than that transported in the system with 8 coils. An increase in the number of coils is not directly proportional to the output mass, i.e. a two-fold decrease in the number coils does not necessarily lead to a two fold increase in the output dosed mass. For example, at the third dose, the configurations with 2, 4 and 6 coils have cumulative dosed masses of 37grams, 24grams and 15grams, respectively. The under-prediction of the mass per dose is more extreme for less numbers of coils (or wider pitch) but is close to the mass per dose for the simulation with the narrower pitch (7 to 8 coils).

### 5.5.5 Locally averaged macroscopic fields

One advantage of performing simulation is the possibility for data-mining to obtain macroscopic fields from microscopic data. In this section, we show macroscopic fields of velocity and density that can be obtained from simulations.

In Fig. 5.11, we show the velocity of the particles in the outlet of the box along with the staggered motion of the coil (on = 1/off = 0). For this simulation, the motion of the coil is

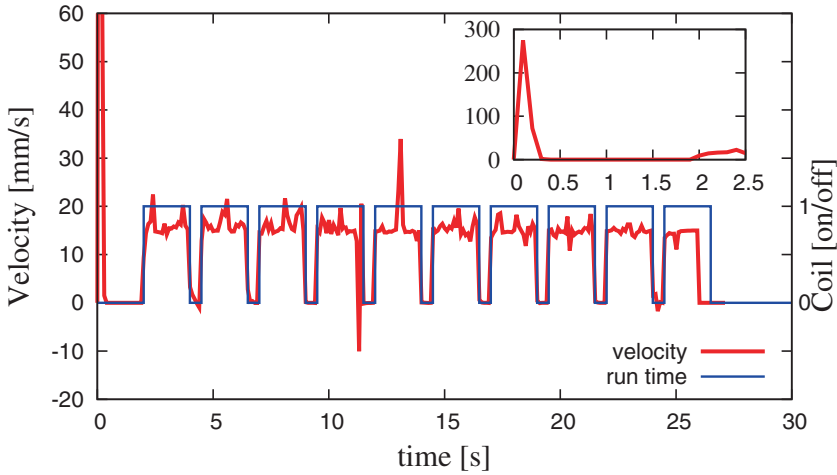


Figure 5.11: Outlet material velocity (along  $z$ ) during multiple dosing. The solid line represent the on-off motion of the coil. The coil angular velocity  $\omega = 9.42$  rad/s,  $V_t = 94.5$  mm/s and  $V_z = 2.09$  mm/s.

such that an initial relaxation of 2 s allows the particles to settle during particle generation, followed by a staggered dosing phase where the coil is rotated for 2 seconds at 90rpm, with waiting time of 0.5 seconds between successive doses until the box becomes empty.

During the initial phase, where the particles are, a momentary increase in the velocity can be seen as the particle fall to the base of the box and some escape through the outlet. The particles quickly settle and the velocity drops to zero. Once the coil begins to move at  $t = 2$  s, the velocity increases again with fluctuations and reaching a peak of  $\approx 18$  mm/s before steadily decreasing to zero as the coil motion goes to zero. The same pattern can be seen from the subsequent doses. It should be noted that even though the velocity profile is mostly positive, we observe in some cases a negative velocity arising from a single particle moving in the opposite direction. This happens mostly during the dosing phase when the coil is moving and is possibly due to collision with other particles or due to violent contact with the boundary (coil).

Along with the velocity profile, in Figs. 5.12 we also show the surface profile evolution from experiments and simulation. At the initial state, for both simulation and experiment, the initial profile is flat with the particles evenly distributed along the length of the box. As the dosing progressed with more and more particles leaving the box, the height reduces unevenly. As observed in the experiments, the height is lower in the region around the rear end of the box since the mass transport is filling the empty coil this region. In general, the evolution of the surface profile as observed in experiment and simulation are qualitatively very similar. For a quantitative comparison, effects of e.g. the wall friction and other parameters must be



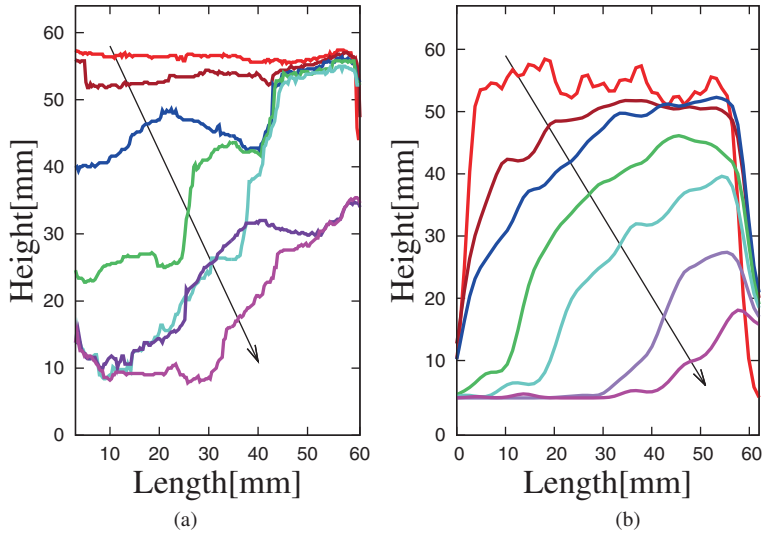


Figure 5.12: The surface profile evolution in time during the dosing process for (a) experiment (b) simulation; the arrow indicates the decreasing trend in time.

studied in more detail to complete the picture.

## 5.6 Conclusion

The dosing of cohesive powders in a simplified canister geometry has been studied using experiments and discrete element simulations. This work has highlighted the prospects of using discrete element simulations to model a complex application test relevant in the food industry. While the modelling of cohesion remains a challenging issue, this work highlights important aspects that can be useful for future research on this subject.

- i. Scaling or coarse-graining of meso-particles by increasing their size relative to the primary (real) particles and setting appropriate parameters, e.g. timescales, to mimic the experimental particles makes it possible to simulate fine powders.
- ii. Calibration of the interparticle friction and cohesive model parameters to match the experimental dosed mass leads to parameter values, different from those expected for the primary particles.
- iii. Homogenization techniques to obtain macroscopic fields provides further insights into the dosing mechanisms beyond experimental methods.

Using the dosed mass as a target variable, we have shown experimentally that the number of doses shows an inverse proportionality to increasing dosage time. Consequently, the dosed mass shows a linear increase with dosage time as expected from the estimated mass per dose. Increasing the number of turns in the coil leads to a non-proportional increase of the dose mass. The mass output from the canister is found to show only a tiny sensitivity to the initial mass in the canister.

All these observations have been confirmed by discrete element simulations for smaller masses while effects of arching and blockage were observed for higher masses are over-estimated. Future work will focus on the quantitative comparison for the masses as used in the experiments. The effects of wall friction and rolling resistance are presently being studied. An extraction of other macroscopic fields like stress or structure using homogenization tools can shed further light on the dosing process.

## Acknowledgement

Helpful discussions with N. Kumar and M. Wojtkowski are gratefully acknowledged. This work is financially supported by the European Union funded Marie Curie Initial Training Network, FP7 (ITN-238577), see <http://www.pardem.eu/> for more information.



## Chapter 6

# Conclusions and Recommendations

### Conclusions

Understanding the mechanical properties of granular materials is important both for practical and fundamental reasons. In the chapters 2 and 3 of this thesis, we have used discrete element simulations to study the microscopic and macroscopic response of assemblies of polydisperse granular packings under quasi-static isotropic and anisotropic loading and unloading. Through a variation of the preparation, the loading paths and quantities such as the volume fraction and contact friction coefficient, this thesis contributes to the understanding of the micromechanical origin of the macroscopic response of granular packings. As a complement, chapter 4 provides new insights on the stress relaxation response of cohesive powders at different stress levels and should be relevant for future research on the development of new contact models for cohesive granular systems. As a step forward towards application, in chapter 5, we have showcased the strength of DEM in modelling an industrially relevant problem like the dosing of cohesive powders. The insights on the macroscopic fields obtained through homogenization techniques are novel for this set-up and should be relevant for various applications in powder transport or processing especially in the food industry.

For validation, a wide class of element tests was defined in the example of a cubical box with periodic boundary conditions that allow to control stress or strain, or both. The beauty of this set-up is its flexibility in providing various element deformation tests within one set-up.

For example, isotropic and deviatoric tests which were used for calibration of a model and the uniaxial compression test used for validation/prediction.

Validation on the level of element tests is a first level consistency-check before the model and insights gained is used for the prediction of larger scale applications, which are typically non-homogeneous, non-continuous, erratic such as the dosing accuracy test. Comparison of DEM simulations with element test experimental data, also opens the door towards insight into the microscopic mechanisms and the wealth of information DEM can provide. By applying data-mining techniques, the microscopic mechanisms at the basis of the behaviour of particle systems is now better understood and used to improve calibration procedures, validation tests and the predictive quality in general.

Several conclusions can be drawn from the analysis:

From the strain-controlled loading and unloading of isotropic, uniaxial and two complementary deviatoric (pure shear) type deformation modes we conclude, for frictionless assemblies (see chapter 2) that:

1. The jamming volume fraction,  $v_c$  is not a single, particular volume fraction, but depends on the deformation modes. Isotropic deformation leads to an increase of the jamming volume fraction whereas deviatoric modes slightly decreases  $v_c$ .
2. The uniaxial, deviatoric and isotropic modes can be described by the same analytical pressure evolution equation. At larger strains, the build up of anisotropy causes the uniaxial and deviatoric modes to deviate from the isotropic deformation mode.
3. The structural anisotropy response (quantified by the deviatoric fabric) to deviatoric strain is qualitatively similar to that of the deviatoric stress ratio while the quantitative response is different. The deviatoric and isotropic stress and strains are cross-coupled by the structural anisotropy such that isotropic strain can cause deviatoric stress response in the presence of structural anisotropy (and vice versa).
4. The calibration of the parameters of a constitutive model with anisotropy, using the deviatoric mode, predicts well an independent test. The uniaxial compression test prediction captures well the basic features of the deviatoric stress and fabric evolution.

In summary, using the simplest contact model and seemingly unrealistic materials, the peculiar interplay of stress, strain, and microstructure was obtained for various deformation modes while the predictive quality of a calibrated anisotropy model was successfully tested.

For the effects of friction on polydisperse assemblies under uniaxial loading and unloading (see chapter 3), we find that:

5. The deviatoric stress and deviatoric fabric evolve strongly differently from each other, in the presence of friction. The peak deviatoric stress ratio reached increases up to  $\mu = 0.3$  before decreasing a little for higher friction. On the other hand, the peak

deviatoric fabric reached shows a decreasing trend with friction.

6. The directional change of the orientation of largest stress eigenvector has a friction-dependent delay with respect to when strain is reversed. On the other hand, high friction causes reversal of fabric to happen much earlier than stress reversal leading to a tilt to the perpendicular direction. The orthogonality of strong and weak forces with respect to each other was also confirmed.
7. The history or “memory” effect leads to the irrecoverability of the initial states after strain reversal. From the directional probability distributions, we find that the forces and contacts in the tensile direction after unloading are generally weaker than those in the neutral (non-mobile) directions.
8. A second order harmonic approximation describes the normal force, whereas contacts, mobilized friction, and tangential force require higher order tensorial descriptors.

Thus, with friction, the microstructure and forces under the simple uniaxial deformation activates microscopic observations that cause interesting macroscopic behavior.

Chapter 4 of this thesis is devoted to understanding the relaxation behavior of cohesive powders under uniaxial compression, experimentally and theoretically

The main conclusions of this study are:

9. Under uniaxial compression of cohesive powder samples for intermediate relaxation at different stress levels, a slow, systematically time-dependent decrease in the axial stress at constant volumetric strain is observed and confirmed in two experimental setups.
10. For longer relaxation time, effects of previously experienced relaxation becomes visible at higher stress level.
11. A simple microscopic model including only two parameters namely the relaxation timescale and a creep material parameter captures the stress relaxation behavior for all stress levels and different materials.
12. Previous long relaxation reduces the possibility for present relaxation.

In general, measurements with simple oedometric testers have revealed the time dependent stress relaxation behavior of cohesive powders which originates from slow dynamics in contacts and thus macroscopic stress relaxation or creep.

On the experimental and numerical study of the dosing of cohesive powders in a simplified canister geometry, the following conclusions are drawn.

13. Scaling or coarse-graining of meso-particles by increasing their size relative to the primary (real) particles and setting appropriate parameters, e.g. timescales, to mimic the experimental particles makes it possible to simulate fine powders. For our system,

a limitation to size scaling is the pitch of the coil which determines the maximum particle size possible, i.e, it should be several times smaller than the pitch or diameter of the coil.

14. Using the mass per dose as a calibration parameter, discrete element simulation results compare quantitatively with results from experiments.
15. Experiments and discrete element simulation of the dosing process confirm that the dosing is most rapid at the back of the screw, where empty space becomes available first, and where avalanches occur.
16. The number of doses is found to be inversely proportional to dosage time and coil rotation speed but increases with increasing number of coils. The mass per dose shows a linear dependence on the dosage time, as expected.
17. Only the dependence on the coil pitch is non-linear.

Scaling or coarse-graining of meso-particles by increasing their size relative to the primary (real) particles and setting appropriate parameters, e.g. timescales, to mimic the experimental particles makes it possible to simulate fine powders.

## Recommendations

The critical evaluation of DEM simulations that predict new, non-calibrated regimes and materials will still remain a challenge in the future, however, a few successful cases could be shown in this thesis. Having a prediction of an experimental lab-scale or real-size industrial application, the comparison between prediction and real-life realization represents a second level validation, but requires more attention. Based on the experience gathered over the course of completing this thesis, the following recommendations could guide future research.

In polydisperse packings, interactions between particles were modeled with using the simplest linear contact force-overlap law. This simple approach is able to capture important features of granular materials. A possible direction for future research will be simulations where more realistic, non-linear contact models such as Hertz-Mindlin are used to generalize the results in this thesis for the case of linearly elastic spheres. Additionally, the validity of the findings for non-spherical particles also needs to be given more attention.

A great deal of care has to be taken when element test simulations are carried out. Most systems are very sensitive to the preparation protocol employed and these effects have to be quantified appropriately for reliable numerical results and models derived from those. A set of best practice guidelines when performing element test simulations are highlighted below:

- When performing wall driven isotropic preparation, one must take into account inhomogeneities that could arise due to the wall motion. This is visible even when periodic boundary

---

conditions are used under (slow) quasi-static conditions. To check for the presence of inhomogeneities, it is best to visualize (on a 3D plot) the locations of particle contacts with high friction mobilization. As consistency check, the particles closest to the wall (where friction is mobilized directly/first) could be excluded and the results compared with the full system analysis for consistency.

- When pressure-driven isotropic preparation is used, the mass of the walls (periodic or real) must be set to be of the order of the total mass of particles used in the simulation. Additionally, too large values of wall mass can lead to large energy fluctuations and too small wall mass values can lead to violent spurious motions; hence both must be avoided.

- Strain-rate control simulations generally lead to more homogeneous states compared to the wall driven mode. However, as best practice, in all cases, the system must be sufficiently relaxed after each preparation state, to approach mechanical equilibrium as close as possible.

- When the swelling method is used and particles are allowed to grow, it must be understood that the particle mass changes as well as the radius. Due to this, one must take care that the values of parameters such as the contact duration and particle stiffness are still reasonable and valid for the particular set-up. Comparison with the previous methods can be done nevertheless, by using dimensionless quantities.

Furthermore, the element test simulation results need to be checked against laboratory experiments and if required new experiments should be carried out. Parameters not easily accessible from experiments, namely, coordination number or fraction of rattlers, will also require advanced experimental and numerical techniques such as X-ray tomography, positron emission particle tracking (PEPT) and others. Additionally, experimental measurements of the parameters of the anisotropy model also needs to be explored.

## Outlook

At the beginning of this research, the plan was to use the uniaxial element experimental data presented in chapter 4 to calibrate DEM simulation parameters from chapter 3, with cohesion included as new ingredient, in addition to friction. This can then be combined with the calibration results from dynamic rotating drum tests (in a related project) to finally predict the dosing application test presented in chapter 5 based on independent calibration experiments. Due to delay in some parts of the project, we directly simulated the dosing test without relying on the independent calibration experiments for the DEM parameters. Instead, we use a simplified calibration procedure based on the mass per dose obtained as the initial slope of the cumulative dosed mass. With the simplified calibration, other dosage time were compared to experiments. The use of independent calibration experiments is certainly a gap that will need to be addressed in future research on this topic.



As shown in this thesis, still a lot of bulk material behaviour need to be understood and only by developing material characterization tests accessing to those mechanisms will this be possible. Modelling of real-life particle shapes, system sizes and contacts remains a daunting challenge. We hope that the results presented in this thesis will be useful in the future for understanding the potential of discrete element simulations in modelling industrial problems and by providing a starting point for future research.

Advances in computational methodologies and parallel programming is expected to aid the deployment of discrete element simulations in modelling industrial applications on a larger scale. The answers provided by this thesis, no doubt elicited new questions which will have to be answered in the future.

# References

- [1] IQ Group: Like Sand through the MySuper Hourglass. <http://www.iqgroup.com.au/intelligence/blog/like-sand-through-the-mysuper-hourglass/>.
- [2] The Environmental Occupational Pathology Division, Dept. of Pathology, SUNY Upstate Medical University. <http://www.upstate.edu/pathenvi/>.
- [3] PARDEM WP1 Report: Characterization for Calibration of DEM datasets. pages 1–53, 2011.
- [4] PARDEM WP2 State of the Art Report: DEM Model Validation Experiments. pages 1–86, 2011.
- [5] PARDEM WP3 State of the art Review Document. pages 1–85, 2011.
- [6] PARDEM WP4 Report: Data mining in DEM Datasets. pages 1–27, 2013.
- [7] PARDEM WP4 Report: Predictive Capabilities of DEM Datasets. pages 1–35, 2013.
- [8] H. Abou-Chakra and U. Tüzün. Coefficient of friction of binary granular mixtures in contact with a smooth wall. Part B. Micro-structural model describing the effects of packing fraction and load distribution on the wall friction of smooth, elastic spheres. *Chemical Engineering Science*, 54(24):5913–5925, Dec. 1999.
- [9] J. Ai, J.-F. Chen, J. M. Rotter, and J. Y. Ooi. Assessment of rolling resistance models in discrete element simulations. *Powder Technology*, 206(3):269–282, 2011.
- [10] F. Alonso-Marroquin and H. J. Herrmann. Ratcheting of Granular Materials. *Physical Review Letters*, 92(5), 2004.
- [11] F. Alonso-Marroquin, S. Luding, H. J. Herrmann, and I. Vardoulakis. Role of anisotropy in the elastoplastic response of a polygonal packing. *Phys. Rev. E*, 71(5), 2005.
- [12] X. Z. An, R. Y. Yang, R. P. Zou, and A. B. Yu. Effect of vibration condition and inter-particle frictions on the packing of uniform spheres. *Powder Technology*, 188(2):102–109, Dec. 2008.
- [13] B. Andreotti, Y. Forterre, and O. Pouliquen. *Granular Media: Between Fluid and Solid*. Cambridge University Press, 2013.
- [14] S. J. Antony and N. P. Krut. Role of interparticle friction and particle-scale elasticity in the shear-strength mechanism of three-dimensional granular media. *Physical Review E (Statistical, Nonlinear, and Soft Matter Physics)*, 79:031308(3), 2009.

- [15] S. J. Antony and M. A. Sultan. Role of interparticle forces and interparticle friction on the bulk friction in charged granular media subjected to shearing. *Physical Review E (Statistical, Nonlinear, and Soft Matter Physics)*, 75:031307(3), 2007.
- [16] T. M. Atanackovic. A modified Zener model of a viscoelastic body. 14(2):137–148, 2002.
- [17] E. Azéma and F. Radjai. Stress-strain behavior and geometrical properties of packings of elongated particles. *Physical Review E*, 81:051304:1–17, 2010.
- [18] E. Azéma, F. Radjai, R. Peyroux, and G. Saussine. Force transmission in a packing of pentagonal particles. *Physical Review E*, 76:011301, 2007.
- [19] E. Azéma, F. Radjai, and G. Saussine. Quasistatic rheology, force transmission and fabric properties of a packing of irregular polyhedral particles. *Mechanics of Materials*, 41(6):729–741, 2009.
- [20] R. L. Bagley and P. J. Torvik. On the fractional calculus model of viscoelastic behavior. *Journal of Rheology*, 30:133, 1986.
- [21] M. M. Bandi, M. K. Rivera, F. Krzakala, and R. E. Ecke. Fragility and hysteretic creep in frictional granular jamming. *Physical Review E*, 87(4), Apr. 2013.
- [22] J. P. Bardet. *Experimental Soil Mechanics*. Prentice-Hall, Upper Saddle River, New Jersey, 1997.
- [23] D. Barreto and C. O’Sullivan. The influence of inter-particle friction and the intermediate stress ratio on soil response under generalised stress conditions. *Granular Matter*, 14(4):505–521, 2012.
- [24] G. Baumann, T. Scheffler, I. M. Jánosi, and D. E. Wolf. Angle of repose in a two-dimensional rotating drum model. In D. E. Wolf, M. Schreckenberg, and A. Bachem, editors, *Traffic and Granular Flow*, page 347, Singapore, 1996. World Scientific.
- [25] D. Bi, J. Zhang, B. Chakraborty, and R. P. Behringer. Jamming by shear. *Nature*, 480(7377):355–358, 2011.
- [26] M. Bortolamasi and J. Fottner. Design and sizing of screw feeders. In *Proc. Partec 2001, Int. Congress for Particle Technology*, pages 27–29, 2001.
- [27] F. P. Bowden and D. Tabor. *The Friction and Lubrication of Solids - Part I*. Clarendon Press, Oxford, 1950.
- [28] R. Brewster, G. S. Grest, and A. J. Levine. Effects of cohesion on the surface angle and velocity profiles of granular material in a rotating drum. *Physical Review E*, 79:011305, 2009.
- [29] N. Brodu, J. D. And, and R. P. Behringer. -. *Private Communication*, 2013.
- [30] H. J. Bunge and P. R. Morris. *Texture analysis in materials science: mathematical methods*. Butterworths London, 1982.
- [31] F. Cantelaube and D. Bideau. Radial Segregation in a 2d Drum: An Experimental Analysis. *EPL (Europhysics Letters)*, 30(3):133+, Apr. 1995.
- [32] F. Chambon, Z. S. Petrovic, W. J. MacKnight, and H. H. Winter. Rheology of model polyurethanes at the gel point. *Macromolecules*, 19(8):2146–2149, 1986.
- [33] P. W. Cleary. DEM modelling of particulate flow in a screw feeder Model description. *Progress in Computational Fluid Dynamics, An International Journal*, 7(2/3/4):128–138, 2007.
- [34] P. A. Cundall and O. D. L. Strack. A discrete numerical model for granular assemblies. *Géotechnique*, 29(1):47–65, 1979.

- [35] X. L. Deng and R. N. Davé. Dynamic simulation of particle packing influenced by size, aspect ratio and surface energy. *Granular Matter*, 15:401–415, 2013.
- [36] J. H. Dieterich and B. D. Kilgore. Direct observation of frictional contacts: New insights for state-dependent properties. *Pure and Applied Geophysics*, 143(1-3):283–302, 1994.
- [37] P. J. Digby. The Effective Elastic Moduli of Porous Granular Rocks. *Journal of Applied Mechanics*, 48(4):803–808, 1981.
- [38] O. Durán, N. P. Kruyt, and S. Luding. Micro-mechanical analysis of deformation characteristics of three-dimensional granular materials. *International Journal of Solids and Structures*, 47(17):2234–2245, 2010.
- [39] B. J. Ennis, J. Green, and R. Davies. The legacy of neglect in the US. *Chemical engineering progress*, 90(4):32–43, 1994.
- [40] A. Ezaoui and H. Di Benedetto. Experimental measurements of the global anisotropic elastic behaviour of dry Hostun sand during triaxial tests, and effect of sample preparation. *Géotechnique*, 59(7):621–635, 2009.
- [41] H. Feise and J. Schwedes. Investigation of the Behaviour of Cohesive Powder in the Biaxial Tester. *KONA*, 13:99–104, 1995.
- [42] H. J. Feise. A review of induced anisotropy and steady-state flow in powders. *Powder Technology*, 98(3):191–200, 1998.
- [43] D. G. Fredlund. Second Canadian Geotechnical Colloquium: Appropriate concepts and technology for unsaturated soils. *Canadian Geotechnical Journal*, 16(1):121–139, 1979.
- [44] C. Friedrich. Relaxation and retardation functions of the Maxwell model with fractional derivatives. *Rheologica Acta*, 30(2):151–158, Mar. 1991.
- [45] B. N. Ghosh. Conveyance of wet parchment coffee beans by an auger. *Journal of Agricultural Engineering Research*, 12(4):274–280, 1967.
- [46] W. G. Gloeckle and T. F. Nonnenmacher. Fractional integral operators and Fox functions in the theory of viscoelasticity. *Macromolecules*, 24(24):6426–6434, Nov. 1991.
- [47] J. D. Goddard. Continuum Modeling of Granular Assemblies. In H. J. Herrmann, J. P. Hovi, and S. Luding, editors, *Physics of dry granular media - NATO ASI Series E 350*, pages 1–24, Dordrecht, 1998. Kluwer Academic Publishers.
- [48] J. D. Goddard. A dissipative anisotropic fluid model for non-colloidal particle dispersions. *Journal of Fluid Mechanics*, 568(1):1–17, 2006.
- [49] J. D. Goddard. Parametric hypoplasticity as continuum model for granular media: from Stokesium to Mohr-Coulombium and beyond. *Granular Matter*, 12(2):145–150, 2010.
- [50] I. Goldhirsch. Stress, stress asymmetry and couple stress: from discrete particles to continuous fields. *Granular Matter*, 12(3):239–252, 2010.
- [51] F. Göncü, O. Durán, and S. Luding. Constitutive relations for the isotropic deformation of frictionless packings of polydisperse spheres. *C. R. Mécanique*, 338(10-11):570–586, 2010.
- [52] F. Göncü and S. Luding. Effect of particle friction and polydispersity on the macroscopic stress-strain relations of granular materials. *Acta Geotechnica*, 2013.
- [53] N. Guo and J. Zhao. The signature of shear-induced anisotropy in granular media. *Computers and Geotechnics*, 47:1–15, 2013.

- [54] J. Harder and J. Schwedes. The Development of a True Biaxial Shear Tester. *Particle and Particle Systems Characterization*, 2(1-4), 1985.
- [55] D. R. Hayhurst. Creep rupture under multi-axial states of stress. *Journal of the Mechanics and Physics of Solids*, 20(6):381–382, 1972.
- [56] K. H. Head. *Manual of soil laboratory testing: Effective stress tests*. Manual of Soil Laboratory Testing. John Wiley & Sons, 1998.
- [57] O. I. Imole, D. Krijgsman, T. Weinhart, V. Magnanimo, E. C. Montes, M. Ramaioli, and S. Luding. Experiments and Discrete Element Simulation of the Dosing of Cohesive Powders in a Canister Geometry. *In preparation*, 2014.
- [58] O. I. Imole, N. Kumar, and S. Luding. Deformation modes of packings of frictionless polydisperse spheres. *Particulate Systems Analysis Conference Proceedings*, pages 1–6, 2011.
- [59] O. I. Imole, N. Kumar, and S. Luding. Element test experiments and simulations: from dry towards cohesive powders. In E. Oñate and D. R. J. Owen, editors, *II International Conference on Particle-based Methods - Fundamentals and Applications*, pages 1–10. ICNME, 2011.
- [60] O. I. Imole, N. Kumar, V. Magnanimo, and S. Luding. Hydrostatic and Shear Behavior of Frictionless Granular Assemblies Under Different Deformation Conditions. *KONA Powder and Particle Journal*, 30:84–108, 2013.
- [61] O. I. Imole, M. Paulick, M. Morgeneyer, V. Magnanimo, E. C. Montes, M. Ramaioli, A. Kwade, and S. Luding. An experimental and theoretical investigation of the time-dependent relaxation behavior of cohesive powders. *In preparation*, 2014.
- [62] O. I. Imole, M. Wojtkowski, V. Magnanimo, and S. Luding. Force correlations, anisotropy, and friction mobilization in granular assemblies under uniaxial deformation. In A. Yu and S. Luding, editors, *Powders and Grains, AIP Conf. Proc.*, volume 1542, pages 601–604, 2013.
- [63] O. I. Imole, M. B. Wojtkowski, V. Magnanimo, and S. Luding. Micro-Macro Correlations and Anisotropy in Granular Assemblies under Uniaxial Loading and Unloading. *Phys. Rev. E (Under Review)*, 2013.
- [64] I. Ishibashi, T. Agarwal, and S. A. Ashraf. Anisotropic behaviors of glass spheres by a discrete element model and laboratory experiment. In *Proceedings of the 1st US Conference on Discrete Element Methods (DEM)*, volume 23, 1989.
- [65] R. J. M. Janssen and H. Zetzener. Measurements on cohesive powder with two biaxial shear testers. *Chem. Engng. & Technol.*, 26(2):147–151, 2003.
- [66] J. T. Jenkins. Volume change in small strain axisymmetric deformations of a granular material, 1987.
- [67] K. L. Johnson. *Contact Mechanics*. Cambridge Univ. Press, Cambridge, 1989.
- [68] A. K. Jonscher. The ‘universal’ dielectric response. *Nature*, 267(5613):673–679, June 1977.
- [69] A. K. Jonscher. Dielectric relaxation in solids. *Journal of Physics D: Applied Physics*, 32(14):R57–R70, July 1999.
- [70] S. Kamath, V. M. Puri, and H. B. Manbeck. Flow property measurement using the Jenike cell for wheat flour at various moisture contents and consolidation times. *Powder Technology*, 81(3):293–297, 1994.
- [71] E. Kjartansson. Constant Q-wave propagation and attenuation. *J. Geophys. Res.*, 84(B9):4737–4748, Aug. 1979.

- [72] D. Kolymbas, I. Herle, and P. A. von Wolffersdorff. Hypoplastic constitutive equation with internal variables. *International Journal for Numerical and Analytical Methods in Geomechanics*, 19(6):415–436, 1995.
- [73] M. P. Kruijjer, L. L. Warnet, and R. Akkerman. Modelling of the viscoelastic behaviour of steel reinforced thermoplastic pipes. *Composites Part A: Applied Science and Manufacturing*, 37(2):356–367, Feb. 2006.
- [74] N. P. Kruyt. Contact forces in anisotropic frictional granular materials. *International Journal of Solids and Structures*, 40(13-14):3537–3556, 2003.
- [75] N. P. Kruyt, I. Agnolin, S. Luding, and L. Rothenburg. Micromechanical study of elastic moduli of loose granular materials. *Journal of the Mechanics and Physics of Solids*, 58(9):1286–1301, 2010.
- [76] N. P. Kruyt and L. Rothenburg. Probability density functions of contact forces for cohesionless frictional granular materials. *International Journal of Solids and Structures*, 39(3):571–583, 2002.
- [77] M. R. Kuhn and K. Bagi. Specimen Size Effect in Discrete Element Simulations of Granular Assemblies. *Journal of Engineering Mechanics*, 135(6):485–492, 2009.
- [78] N. Kumar, O. I. Imole, V. Magnanimo, and S. Luding. Deformation Modes for Assemblies of Frictionless Polydisperse Spheres. *Advanced Materials Research*, 508:160–165, 2012.
- [79] N. Kumar, O. I. Imole, V. Magnanimo, and S. Luding. Effect of polydispersity on the micro-macro behavior of granular assemblies under different deformation paths. *Particuology*, (<http://dx.doi.org/10.1016/j.partic.2013.07.011>), 2013.
- [80] N. Kumar, O. I. Imole, V. Magnanimo, and S. Luding. Evolution of the Effective Moduli for Anisotropic Granular Materials during Shear. In S. Luding and A. Yu, editors, *Powders & Grains 2013*, pages 1238–1241, Sydney, Australia, 2013. Balkema.
- [81] N. Kumar, O. I. Imole, V. Magnanimo, and S. Luding. Predictive methods for deformation modes using constitutive modeling for frictionless spheres: Micro-macro transition to Anisotropy model. *In preparation*, 2013.
- [82] A. Kwade, D. Schulze, and J. Schwedes. Determination of the stress ratio in uniaxial compression tests - Part 1. *Powder handling & Processing*, 6(1):61–65, 1994.
- [83] A. Kwade, D. Schulze, and J. Schwedes. Determination of the stress ratio in uniaxial compression tests - Part 2. *Powder handling & Processing*, 6(2):199–203, 1994.
- [84] A. Kwade, D. Schulze, and J. Schwedes. Design of silos: Direct measurement of stress ratio [Auslegung von Silos. Unmittelbare Messung des Horizontallastverhaeltnisses]. *Beton- und Stahlbetonbau*, 89(3):58+, EMPTY.
- [85] L. La Ragione and V. Magnanimo. Contact anisotropy and coordination number for a granular assembly: A comparison of distinct-element-method simulations and theory. *Physical Review E.*, 85(3), 2012.
- [86] L. La Ragione, V. Magnanimo, J. Jenkins, and H. Makse. Irreversible Incremental Behavior in a Granular Material. In *APS Meeting Abstracts*, 2012.
- [87] S. Luding. Micro-Macro Models for Anisotropic Granular Media. In P. A. Vermeer, W. Ehlers, H. J. Herrmann, and E. Ramm, editors, *Modelling of Cohesive-Frictional Materials*, pages 195–206, Leiden, Netherlands, 2004. Balkema.
- [88] S. Luding. Micro-macro transition for anisotropic, frictional granular packings. *International Journal of Solids and Structures*, 41(21):5821–5836, 2004.

- [89] S. Luding. Anisotropy in cohesive, frictional granular media. *Journal of Physics Condensed Matter*, 17(24):S2623–S2640, 2005.
- [90] S. Luding. About contact force-laws for cohesive frictional materials in 2D and 3D. In P. Walzel, S. Linz, C. Krülle, and R. Grochowski, editors, *Behavior of Granular Media*, pages 137–147. Shaker Verlag, 2006.
- [91] S. Luding. Contact Models for Very Loose Granular Materials. In P. Eberhard, editor, *IUTAM Symposium on Multiscale Problems in Multibody System Contacts*, volume 1 of *IUTAM Bookseries*, pages 135–150. Springer Netherlands, 2007.
- [92] S. Luding. Cohesive, frictional powders: contact models for tension. *Granular Matter*, 10(4):235–246, 2008.
- [93] S. Luding. Constitutive relations for the shear band evolution in granular matter under large strain. *Particulate Science and Technology*, 6(6):501–505, 2008.
- [94] S. Luding. The effect of friction on wide shear bands. *Particulate Science and Technology*, 26(1):33–42, 2008.
- [95] S. Luding. Towards dense, realistic granular media in 2D. *Nonlinearity*, 22(12):R101–R146, 2009.
- [96] S. Luding and E. Bauer. Evolution of swelling pressure of cohesive-frictional, rough and elasto-plastic granulates. In M. J. Jiang, F. Liu, and M. Bolton, editors, *Geomechanics and Geotechnics: From Micro to Macro, (IS-Shanghai Conference Proceedings)*, pages 495–499. CRC Press/Balkema, 2011.
- [97] S. Luding, K. Manetsberger, and J. Mullers. A discrete model for long time sintering. *Journal of the Mechanics and Physics of Solids*, 53(2):455–491, 2005.
- [98] S. Luding and E. S. Perdahcıođlu. A Local Constitutive Model with Anisotropy for Various Homogeneous 2D Biaxial Deformation Modes. *Chemie Ingenieur Technik*, 83(5):672–688, 2011.
- [99] M. Madadi, O. Tsoungui, M. Latzel, and S. Luding. On the fabric tensor of polydisperse granular materials in 2D. *International Journal of Solids and Structures*, 41(9-10):2580, 2004.
- [100] V. Magnanimo, L. La Ragione, J. T. Jenkins, P. Wang, and H. A. Makse. Characterizing the shear and bulk moduli of an idealized granular material. *EPL (Europhysics Letters)*, 81(3):34006, 2008.
- [101] V. Magnanimo and S. Luding. A local constitutive model with anisotropy for ratcheting under 2D axial-symmetric isobaric deformation. *Granular Matter*, 13(3):225–232, 2011.
- [102] V. Magnanimo and S. Luding. A 2D non-linear constitutive model with anisotropy for granular materials. *Philosophical Magazine*, (Under review), 2012.
- [103] F. Mainardi. *Fractional Calculus and Waves in Linear Viscoelasticity*. Imperial College Press-World Scientific, London, 2010.
- [104] T. S. Majmudar and R. P. Behringer. Contact force measurements and stress-induced anisotropy in granular materials. *Nature*, 435(7045):1079–1082, 2005.
- [105] T. S. Majmudar, M. Sperl, S. Luding, and R. P. Behringer. Jamming Transition in Granular Systems. *Phys. Rev. Lett.*, 98(5), 2007.
- [106] H. A. Makse, D. L. Johnson, and L. M. Schwartz. Packing of compressible granular materials. *Phys. Rev. Lett.*, 84(18):4160–4163, 2000.
- [107] D. Mařín. Asymptotic behaviour of granular materials. *Granular Matter*, 14(6):759–774, Sept. 2012.
- [108] J. L. Meriam, L. G. Kraige, and W. J. Palm. *Engineering mechanics Vol. 1: statics*. Wiley, 1987.

- [109] E. Merrow. Estimating startup times for solids-processing plants. *Chemical engineering*, 95:89–92, 1988.
- [110] R. Metzler. Fractional relaxation processes and fractional rheological models for the description of a class of viscoelastic materials. *International Journal of Plasticity*, 19(7):941–959, July 2003.
- [111] G. D. R. MiDi. On dense granular flows. *The European Physical Journal E: Soft Matter and Biological Physics*, 14(4):341–365, 2004.
- [112] M. Morgeneyer, L. Brendel, Z. Farkas, D. Kadau, D. E. Wolf, and J. Schwedes. Can one make a powder forget its history? *Proceedings of the 4th international conference for conveying and handling of particulate solids*, 2003.
- [113] M. Morgeneyer and J. Schwedes. Investigation of powder properties using alternating strain paths. *Task Quarterly*, 7(4):571–578, 2003.
- [114] M. Oda. Initial fabrics and their relations to mechanical properties of granular materials. *Soils and Foundation*, 1(12):17–36, 1972.
- [115] M. Oda and K. Iwashita. Study on couple stress and shear band development in granular media based on numerical simulation analyses. *International Journal of Engineering Science*, 38(15):1713–1740, 2000.
- [116] V. Ogarko and S. Luding. Equation of state and jamming density for equivalent bi- and polydisperse, smooth, hard sphere systems. *Journal of Chemical Physics*, 136(12), 2012.
- [117] C. S. O’Hern, S. A. Langer, A. J. Liu, and S. R. Nagel. Random packings of frictionless particles. *Phys. Rev. Lett.*, 88(7), 2002.
- [118] J. Y. Ooi. Establishing predictive capabilities of DEM - Verification and validation for complex granular processes. *AIP Conf. Proc.*, 1542:20–24, 2013.
- [119] P. J. Owen and P. W. Cleary. Prediction of screw conveyor performance using the Discrete Element Method (DEM). *Powder Technology*, 193(3):274–288, 2009.
- [120] P. J. Owen and P. W. Cleary. Screw conveyor performance: comparison of discrete element modelling with laboratory experiments. *Progress in Computational Fluid Dynamics, An International Journal*, 10(5):327–333, 2010.
- [121] A. A. Peña, R. García-Rojo, and H. J. Herrmann. Influence of particle shape on sheared dense granular media. *Granular Matter*, 9(3-4):279–291, June 2007.
- [122] P. Philippe, F. Bonnet, and F. Nicot. Settlement of a granular material: boundary versus volume loading. *Granular Matter*, 13(5):585–598, 2011.
- [123] F. Radjai, J. Y. Delenne, E. Azéma, and S. Roux. Fabric evolution and accessible geometrical states in granular materials. *Granular Matter*, 14(2):259–264, 2012.
- [124] F. Radjai, S. Roux, and J. J. Moreau. Contact forces in a granular packing. *Chaos*, 9(3):544–550, 1999.
- [125] F. Radjai, D. E. Wolf, M. Jean, and J. Moreau. Bimodal Character of Stress Transmission in Granular Packings. *Physical Review Letters*, 80:61–64, 1998.
- [126] M. Ramaioli. Granular flow simulations and experiments for the food industry. *PhD Thesis, EPFL*, 2007.
- [127] G. H. Ristow. Dynamics of granular material in a rotating drum. *Europhys. Lett.*, 34(4):263–268, 1996.
- [128] A. W. Roberts. The influence of granular vortex motion on the volumetric performance of enclosed screw conveyors. *Powder Technology*, 104(1):56–67, 1999.



- [129] A. W. Roberts and A. H. Willis. Performance of Grain Augers. *Proceedings of the Institution of Mechanical Engineers*, 176(1):165–194, 1962.
- [130] M. Röck, M. Morgeneyer, J. Schwedes, D. Kadau, L. Brendel, and D. E. Wolf. Steady state flow of cohesive and non-cohesive powders. *Granular Matter*, 10(4):285–293, June 2008.
- [131] M. Saadatfar, A. P. Sheppard, T. J. Senden, and A. J. Kabla. Mapping forces in a 3D elastic assembly of grains. *Journal of the Mechanics and Physics of Solids*, 60(1):55–66, 2012.
- [132] M. H. Sadd, Q. M. Tai, and A. Shukla. Contact Law effects on Wave Propagation in Particulate Materials using distinct element modeling. *Int. J. Non-Linear Mechanics*, 28(2):251, 1993.
- [133] A. Samimi, A. Hassanpour, and M. Ghadiri. Single and bulk compressions of soft granules: Experimental study and DEM evaluation. *Chemical Engineering Science*, 60(14):3993–4004, 2005.
- [134] M. Satake. Fabric tensor in granular materials. *Proc., IUTAM Symp. on Deformation and Failure of Granular materials, Delft, The Netherlands*, 1982.
- [135] H. Schiessel, R. Metzler, A. Blumen, and T. F. Nonnenmacher. Generalized viscoelastic models: their fractional equations with solutions. *Journal of Physics A: Mathematical and General*, 28(23):6567+, Dec. 1995.
- [136] J. Schindelin, I. Arganda-Carreras, E. Frise, V. Kaynig, M. Longair, T. Pietzsch, S. Preibisch, C. Rueden, S. Saalfeld, B. Schmid, J. Y. Tinevez, D. J. White, V. Hartenstein, K. Eliceiri, P. Tomancak, and A. Cardona. Fiji: an open-source platform for biological-image analysis. *Nature methods*, 9(7):676–682, 2012.
- [137] D. Schulze. Time- and Velocity-Dependent Properties of Powders Effecting Slip-Stick Oscillations. *Chem. Eng. Technol.*, 26(10):1047–1051, Oct. 2003.
- [138] D. Schulze. *Powders and bulk solids: behavior, characterization, storage and flow*. Springer, 2008.
- [139] J. Schwedes. *Fliessverhalten von Schuettguetern in Bunkern*. Verlag Chemie, Weinheim, 1968.
- [140] J. Schwedes. Review on testers for measuring flow properties of bulk solids. *Granular Matter*, 5(1):1–43, 2003.
- [141] M. R. Shaebani, M. Madadi, S. Luding, and D. E. Wolf. Influence of polydispersity on micromechanics of granular materials. *Phys. Rev. E*, 85(1), 2012.
- [142] Y. Shimizu and P. A. Cundall. Three-dimensional DEM simulations of bulk handling by screw conveyors. *Journal of Engineering Mechanics*, 127(9):864–872, 2001.
- [143] T. Shinbrot, N. H. Kim, and N. N. Thyagu. Electrostatic precursors to granular slip events. *Proceedings of the National Academy of Sciences*, 109(27):10806–10810, July 2012.
- [144] K. Shinohara, M. Oida, and B. Golman. Effect of particle shape on angle of internal friction by triaxial compression test. *Powder Technology*, 107(1-2):131–136, 2000.
- [145] L. E. Silbert, D. Ertas, G. S. Grest, T. C. Halsey, and D. Levine. Geometry of frictionless and frictional sphere packings. *Phys. Rev. E*, 65(3, Part 1):051302, 2002.
- [146] S. E. Silbert, G. S. Grest, and J. W. Landry. Statistics of the Contact Network in Frictional and Frictionless Granular Packings. *Physical Review E.*, 66:061303(6 Part 1), 2002.
- [147] L. Staron and F. Radjai. Friction versus texture at the approach of a granular avalanche. *Physical Review E*, 72:041308:1–5, 2005.

- [148] L. Staron, F. Radjai, and J. Vilotte. Granular micro-structure and avalanche precursors. *Journal of Statistical Mechanics: Theory and Experiment*, 2006(07):P07014:1–15, 2006.
- [149] G. N. Stevens. Performance tests on experimental auger conveyors. *J. Agr. Eng. Res.*, 7(1):47–60, 1962.
- [150] A. S. J. Suiker and N. A. Fleck. Frictional collapse of granular assemblies. *Journal of Applied Mechanics*, 71:350–358, 2004.
- [151] J. Sun and S. Sundaresan. A plasticity model with microstructure evolution for dense granular flows. *AIP Proceeding for the Joint IUTAM-ISIMM Symposium on Mathematical Modeling and Physical Instances of Granular Flows*, 1227:280–289, 2010.
- [152] J. Sun and S. Sundaresan. A constitutive model with microstructure evolution for flow of rate-independent granular materials. *Journal of Fluid Mechanics*, 682:590–616, 2011.
- [153] N. Taberlet, P. Richard, and E. J. Hinch. Shape of a granular pile in a rotating drum. *Phys. Rev. E*, 73:050301, 2006.
- [154] S. C. Thakur, O. I. Imole, M. B. Wojtkowski, V. Magnanimo, E. C. Montes, M. Ramaioli, H. Ahmadian, and J. Y. Ooi. Characterization of cohesive powders for bulk handling and DEM modelling. In M. Bischoff, E. Oñate, D. R. J. Owen, E. Ramm, and P. Wriggers, editors, *III International Conference on Particle-based Methods - Fundamentals and Applications*, pages 1–12. ICNME, 2013.
- [155] A. Thornton, T. Weinhart, S. Luding, and O. Bokhove. Modeling of particle size segregation: Calibration using the discrete particle method. *Int. J. Mod. Phys. C*, 23:1240014(08), 2012.
- [156] A. R. Thornton, D. Krijgsman, A. T. Voortwis, V. Ogarko, R. Fransen, S. Gonzalez, O. Bokhove, O. Imole, T. Weinhart, and S. Luding. A review of recent work on the Discrete Particle Method at the University of Twente: An introduction to the open-source package MercuryDPM. pages 1–6, 2013.
- [157] C. Thornton. Quasi-static simulations of compact polydisperse particle systems. *Particuology*, 8(2):119–126, 2010.
- [158] C. Thornton and S. J. Anthony. Quasi-static deformation of particulate media. *Philosophical Transactions of the Royal Society of London. Series A: Mathematical, Physical and Engineering Sciences*, 356(1747):2763–2782, 1998.
- [159] C. Thornton and L. Zhang. A numerical examination of shear banding and simple shear non-coaxial flow rules. *Philosophical Magazine*, 86(21-22):3425–3452, 2006.
- [160] C. Thornton and L. Zhang. On the evolution of stress and microstructure during general 3D deviatoric straining of granular media. *Géotechnique*, 60(5):333–341, 2010.
- [161] J. Tomas. Particle Adhesion Fundamentals and Bulk Powder Consolidation. *KONA*, 18:157–169, 2000.
- [162] J. Tomas. Fundamentals of cohesive powder consolidation and flow. *Granular Matter*, 6(2-3):75–86, 2004.
- [163] R. Tykhoniuk, J. Tomas, S. Luding, M. Kappl, L. Heim, and H. J. Butt. Ultrafine cohesive powders: From interparticle contacts to continuum behavior. *Chem. Eng. Sci.*, 62(11):2843–2864, 2007.
- [164] M. van Hecke. Jamming of soft particles: geometry, mechanics, scaling and isostaticity. *Journal of Physics: Condensed Matter*, 22:033101(3), 2009.
- [165] M. Wahl, R. Kirsch, U. Bröckel, S. Trapp, and M. Bottlinger. Caking of Urea Prills. *Chem. Eng. Technol.*, 29(6):674–678, June 2006.

- [166] S. D. C. Walsh and A. Tordesillas. A thermomechanical approach to the development of micropolar constitutive models of granular media. *Acta mechanica*, 167(3):145–169, 2004.
- [167] K. Walton. The effective elastic moduli of a random packing of spheres. *Journal of the Mechanics and Physics of Solids*, 35(2):213–226, 1987.
- [168] O. R. Walton. Force models for particle-dynamics simulations of granular materials. In E. Guazzelli and L. Oger, editors, *Mobile Particulate Systems*, page 367, Dordrecht, 1995. Kluwer Academic Publishers.
- [169] O. R. Walton and R. L. Braun. Viscosity, Granular-Temperature, and Stress Calculations for Shearing Assemblies of Inelastic, Frictional Disks. *J. Rheol.*, 30(5):949–980, 1986.
- [170] T. Weinhart, R. Hartkamp, A. R. Thornton, and S. Luding. Coarse-grained local and objective continuum description of three-dimensional granular flows down an inclined surface. *Physics of Fluids*, 25:070605(7), 2013.
- [171] T. Weinhart, A. R. Thornton, S. Luding, and O. Bokhove. Closure relations for shallow granular flows from particle simulations. *Granular Matter*, 14(4):531–552, 2012.
- [172] T. Weinhart, A. R. Thornton, S. Luding, and O. Bokhove. From discrete particles to continuum fields near a boundary. *Granular Matter*, 14(2):289–294, 2012.
- [173] C. M. Wensrich, E. H. Kisi, J. F. Zhang, and O. Kirstein. Measurement and analysis of the stress distribution during die compaction using neutron diffraction. *Granular Matter*, 14(6):671–680, 2012.
- [174] H. H. Winter and F. Chambon. Analysis of linear viscoelasticity of a crosslinking polymer at the gel point. *Journal of rheology*, 30:367, 1986.
- [175] M. Wojtkowski, O. I. Imole, M. Ramaioli, E. Chávez Montes, and S. Luding. Behavior of cohesive powder in rotating drums. In *Powders and Grains, AIP Conf. Proc.*, volume 1542, pages 983–986, 2013.
- [176] Y. Yu and P. C. Arnold. Theoretical modelling of torque requirements for single screw feeders. *Powder Technology*, 93(2):151–162, 1997.
- [177] T. S. Yun and T. M. Evans. Evolution of at-rest lateral stress for cemented sands: experimental and numerical investigation. *Granular Matter*, 13(5):671–683, 2011.
- [178] H. Zetzener and J. Schwedes. Deformation behaviour and relaxation of bulk solids at different deformation rates. *6th Intl. Conf. on Handling and Transportation*, pages 51–55, 1998.
- [179] H. Zetzener and J. Schwedes. Relaxation and Creep of Dry Bulk Solids. *Part. Part. Syst. Charact.*, 19(3):144–148, 2002.
- [180] J. Zhang, T. Majmudar, A. Tordesillas, and R. Behringer. Statistical properties of a 2D granular material subjected to cyclic shear. *Granular Matter*, 12(2):159–172, 2010.
- [181] X. Zhao and T. M. Evans. Numerical analysis of critical state behaviors of granular soils under different loading conditions. *Granular Matter*, 13(6):751–764, Sept. 2011.
- [182] Y. C. Zhou, B. H. Xu, A. B. Yu, and P. Zulli. An experimental and numerical study of the angle of repose of coarse spheres. *Powder Technology*, 125(1):45–54, 2002.
- [183] C. Y. Zhu, A. Shukla, and M. H. Sadd. Prediction of Dynamic Contact Loads in Granular Assemblies. *J. of Applied Mechanics*, 58(2):341–346, 1991.

# Curriculum vitae

## Olukayode I. Imole

Born on November 22, 1982 in Lagos, Nigeria

June 1999	High school diploma, C.M.S. Grammar School, Lagos
December 2005	Bachelor of Engineering in Mechanical Engineering, University of Ado-Ekiti
May 2004 - Nov. 2004	Intern, Seven-Up Bottling Company, Ikeja
Feb. 2006 - Feb. 2007	National Youth Service, Jos
Oct. 2007 - July 2008	Associate, KPMG, Lagos.
Oct. 2008 - March 2010	Master of Science in Quality, Safety and Environment, Otto-von-Guericke University, Magdeburg
Oct. 2010 - April 2014	PhD candidate, University of Twente
March - May 2011	Secondment - Nestle Product Technology Center, Orbe
February 2012	Secondment - Technische Universität, Braunschweig

## Publications

### Journal Papers

1. O. I. Imole, N. Kumar, V. Magnanimo, and S. Luding. Hydrostatic and Shear Behavior of Frictionless Granular Assemblies Under Different Deformation Conditions. *KONA Powder and Particle Journal*, 30:84–108, 2013
2. O. I. Imole, M. B. Wojtkowski, V. Magnanimo, and S. Luding. Micro-Macro Correlations and Anisotropy in Granular Assemblies under Uniaxial Loading and Unloading. *Phys. Rev. E (Under Review)*, 2013
3. N. Kumar, O. I. Imole, V. Magnanimo, and S. Luding. Effect of polydispersity on

the micro-macro behavior of granular assemblies under different deformation paths. *Particuology*, (<http://dx.doi.org/10.1016/j.partic.2013.07.011>), 2013

4. O. I. Imole, M. Paulick, M. Morgeneyer, V. Magnanimo, E. C. Montes, M. Ramaioli, A. Kwade, and S. Luding. An experimental and theoretical investigation of the time-dependent relaxation behavior of cohesive powders. *In preparation*, 2014
5. O. I. Imole, D. Krijgsman, T. Weinhart, V. Magnanimo, E. C. Montes, M. Ramaioli, and S. Luding. Experiments and Discrete Element Simulation of the Dosing of Cohesive Powders in a Canister Geometry. *In preparation*, 2014

#### Refereed Proceedings

6. O. I. Imole, M. Wojtkowski, V. Magnanimo, and S. Luding. Force correlations, anisotropy, and friction mobilization in granular assemblies under uniaxial deformation. In A. Yu and S. Luding, editors, *Powders and Grains, AIP Conf. Proc.*, volume 1542, pages 601–604, 2013
7. N. Kumar, O. I. Imole, V. Magnanimo, and S. Luding. Evolution of the Effective Moduli for Anisotropic Granular Materials during Shear. In S. Luding and A. Yu, editors, *Powders & Grains 2013*, pages 1238–1241, Sydney, Australia, 2013. Balkema
8. M. Wojtkowski, O. I. Imole, M. Ramaioli, E. Chávez Montes, and S. Luding. Behavior of cohesive powder in rotating drums. In *Powders and Grains, AIP Conf. Proc.*, volume 1542, pages 983–986, 2013

#### Non-Refereed Proceedings

9. O. I. Imole, N. Kumar, and S. Luding. Deformation modes of packings of frictionless polydisperse spheres. *Particulate Systems Analysis Conference Proceedings*, pages 1–6, 2011
10. N. Kumar, O. I. Imole, V. Magnanimo, and S. Luding. Deformation Modes for Assemblies of Frictionless Polydisperse Spheres. *Advanced Materials Research*, 508:160–165, 2012
11. A. R. Thornton, D. Krijgsman, A. T. Voortwis, V. Ogarko, R. Fransen, S. Gonzalez, O. Bokhove, O. Imole, T. Weinhart, and S. Luding. A review of recent work on the Discrete Particle Method at the University of Twente: An introduction to the open-source package MercuryDPM. pages 1–6, 2013
12. O. I. Imole, N. Kumar, and S. Luding. Element test experiments and simulations: from dry towards cohesive powders. In E. Oñate and D. R. J. Owen, editors, *II International Conference on Particle-based Methods - Fundamentals and Applications*, pages 1–10. ICNME, 2011
13. S. C. Thakur, O. I. Imole, M. B. Wojtkowski, V. Magnanimo, E. C. Montes, M. Ramaioli, H. Ahmadian, and J. Y. Ooi. Characterization of cohesive powders for bulk handling and DEM modelling. In M. Bischoff, E. Oñate, D. R. J. Owen, E. Ramm,

---

and P. Wriggers, editors, *III International Conference on Particle-based Methods - Fundamentals and Applications*, pages 1–12. ICNME, 2013

Other Scientific contributions

14. PARDEM WP2 State of the Art Report: DEM Model Validation Experiments. pages 1–86, 2011
15. PARDEM WP4 Report: Predictive Capabilities of DEM Datasets. pages 1–35, 2013
16. PARDEM WP4 Report: Data mining in DEM Datasets. pages 1–27, 2013
17. PARDEM WP3 State of the art Review Document. pages 1–85, 2011
18. PARDEM WP1 Report: Characterization for Calibration of DEM datasets. pages 1–53, 2011









# Propositions

1. The confined uniaxial test is inherently different from the triaxial test in terms of the deviatoric fabric and coordination number evolution and has the broadest application of all due to its simplicity.
2. For large strains, isotropic deformation produces more efficient packings while uniaxial and shear deformation lead to less efficient packings.
3. The mass per dose is an appropriate parameter for the calibration of the dosing test.
4. Acceptance of DEM for industrial scale prediction will not happen except appropriate calibration, validation and prediction methodologies are developed.
5. The effects of previously experienced longer stress relaxation in cohesive granular materials only manifest at higher stress levels.
6. Similar to stress relaxation in cohesive powders, human beings endure suffering up to a limit after which, the effects are attenuated.
7. If marriages had expiry dates where the extension of the contract can be renegotiated, couples would probably take their relationship more seriously.
8. Faith must always be placed above religion. Religion can only do as much as reform a man, but faith transforms.
9. The abuse of the privileges of foreign aid by donor and receptor nations is the best argument for its abolition.
10. The idea of absolute trust and cooperation between nations is a farce, but it must be pursued.

These propositions are considered opposable and defensible and as such have been approved by the supervisor Prof.dr. S. Luding.

# Stellingen

1. De besloten uniaxiale test verschilt inherent van de triaxiale test, zowel in termen van de evolutie van de deviatorisch structuur en het coördinatiegetal, en heeft de breedste toepassing van beide testen dankzij zijn eenvoud.
2. Voor grote vervormingen produceren isotrope vervormingen efficiëntere pakkingen, terwijl uniaxiale vervormingen en afschuivingen tot minder efficiënte pakkingen leiden.
3. De massa per dosis is een geschikte parameter voor het kalibreren van de doseringstest.
4. Acceptatie van de Discrete Elementen Methode voor voorspellingen op industriële schaal zal niet gebeuren zolang er geen geschikte kalibratie, validatie en voorspellingsmethodes zijn ontwikkeld.
5. De effecten van eerder ervaren langdurige spanningsrelaxatie in cohesieve granulaire materialen manifesteren zich alleen bij hogere spanningsniveaus.
6. Net als spanningsrelaxatie in cohesieve poeders zullen mensen lijden ondergaan tot een limiet waarboven de effecten verzachten.
7. Als huwelijken vervaldagen hadden waarop verlenging van de echt heronderhandeld kan worden, dan zouden paren hun relatie waarschijnlijk serieuzer nemen.
8. Vertrouwen moet altijd boven religie geplaatst worden. Religie kan een mens hervormen, maar vertrouwen transformeert.
9. Het misbruik van de privileges van ontwikkelingshulp door donerende en ontvangende landen is het beste argument voor haar afschaffing.
10. Het idee van absoluut vertrouwen en samenwerking tussen landen is een farce, maar moet worden nagestreefd.

Deze stellingen worden oponeerbaar en verdedigbaar geacht en zijn als zodanig goedgekeurd door de promotor Prof.dr. S. Luding